DEUTSCHES ELEKTRONEN-SYNCHROTRON

DESY-THESIS-2002-033
September 2002

Helicity Analysis of Vector Mesons Produced in Proton-Dissociative Diffractive Photoproduction at Large Momentum Transfer at HERA

by

A. Kowal

ISSN 1435-8085

NOTKESTRASSE 85 - 22607 HAMBURG

To be sure that your reports and preprints are promptly included in the HEP literature database
send them to (if possible by air mail):

DESY Zentralbibliothek Notkestraße 85 22603 Hamburg Germany	DESY Bibliothek Platanenallee 6 15738 Zeuthen Germany

UNIVERSITY OF MINING
AND METALLURGY in Cracow

Faculty of Physics and Nuclear Techniques

Agnieszka Kowal

Helicity Analysis of Vector Mesons Produced in Proton-dissociative Diffractive Photoproduction at Large Momentum Transfer at HERA

PhD Thesis

Supervisor: Prof. dr hab. Danuta Kisielewska

April 2002

Abstract

The proton-dissociative photoproduction of vector mesons $\gamma p \to VN$ has been measured in e^+p interactions at HERA with the ZEUS detector. The integrated luminosity of the data sample under study was 24 pb^{-1}. The data was collected at the photon-proton center-of-mass energy of $W_{\gamma p} \approx 100$ GeV and with the four-momentum transfer in the proton vertex ranging up to $-t = 12$ GeV^2. As a result of the decay angular analysis the spin density matrix elements for the ρ^0, ϕ and J/ψ mesons were determined in the wide $-t$ range available. The obtained results are compared to the expectations of pQCD calculations.

Contents

List of Abbreviations

BAC	backing calorimeter
BCAL	barrel calorimeter
BMUON	barrel muon chambers
BPC	beam pipe calorimeter
BPT	beam pipe tracker
BW	Breit-Wigner function
CTD	central tracking detector
DESY	Deutsches Elektronen-Synchrotron
EMC	electromagnetic calorimeter
FCAL	forward calorimeter
FLT	first level trigger
FMUON	forward muon chambers
FNC	forward neutron calorimeter
HAC	hadronic calorimeter
HERA	Hadron-Elektron Ring Anlage
IP	interaction point
LPS	leading proton spectrometer
LLA	Leading logarithmic approximation
LUMI	luminosity monitor
MC	Monte Carlo
PDG	Particle Data Group
PMT	photomultiplier tube
pQCD	perturbative QCD
PRT	proton remnant tagger
PT	photoproduction tagger
RCAl	rear calorimeter
REMC	rear electromagnetic calorimeter
RMUON	rear muon chambers
SCHC	s-channel helicity conservation
SLT	second level trigger
TLT	third level trigger
UCAL	uranium calorimeter
VDM	vector meson dominance model
VW	veto wall

List of Symbols

$\alpha_{I\!P}(t)$	Pomeron trajectory
$\alpha_{I\!P}(0)$	intercept of the Pomeron trajectory
$\alpha'_{I\!P}$	slope of the Pomeron trajectory
b^V_{el}	t-slope of the elastic process
b^V_{pd}	t-slope of the proton-dissociative process
e	incoming positron
e'	scattered positron
E_e	energy of the incoming positron
$E_{e'}$	energy of the scattered positron
E_{max}	maximum allowed energy of a calorimeter cell not associated with the tracks

η	pseudorapidity
E_V	energy of the outgoing vector meson
Φ_h	angle between the vector meson production plane and the positron scattering plane
φ_h	azimuthal decay angle in the helicity frame
φ_t	azimuthal decay angle in the transversity frame
γ	photon
γ^*	virtual photon
$\Gamma(y, Q^2)$	photon flux
k	four-momentum of the incoming positron
k'	four-momentum of the scattered positron
M_e	positron mass
M_N	mass of the proton-dissociative hadronic system
M_P	proton mass
M_V	vector meson mass
M_{ee}	invariant mass of the two tracks assuming they are electrons
M_{KK}	invariant mass of the two tracks assuming they are kaons
M_{ll}	invariant mass of the two tracks assuming they are leptons (e or μ)
$M_{\mu\mu}$	invariant mass of the two tracks assuming they are muons
$M_{\pi\pi}$	invariant mass of the two tracks assuming they are pions
N	proton-dissociative hadronic system
ν	photon energy in the proton rest frame
P	four-momentum of the incoming proton
P'	four-momentum of the outgoing proton or proton-dissociative system
p	proton
p_T	track transverse momentum
$p_{V,T}$	vector meson transverse momentum
$p_{V,Z}$	vector meson longitudinal momentum
$I\!P$	Pomeron
Q^2	negative four-momentum square of the virtual photon
q	four-momentum of the virtual photon
$I\!R$	Reggeon
r^α_{ik}	vector meson spin density matrix elements
s	square of the positron-proton center-of-mass energy
t	four-momentum transfer squared at the proton vertex
T_{ik}	helicity amplitudes
T^J_M	statistical tensors in the transversity frame
${}^hT^J_M$	statistical tensors in the helicity frame
θ_h	polar decay angle in the helicity frame
θ_t	polar decay angle in the transversity frame
$W_{\gamma p}$	center-of-mass energy of the photon-proton system
V	vector meson
V_X,V_Y,V_Z	x,y,z coordinates of the vertex position at the IP
v	vector meson four-momentum
X,Y,Z	x,y,z coordinates in the HERA Cartesian system with its origin at the nominal IP
y	fraction of the positron energy transferred to the hadronic final state

List of Figures

List of Tables

Chapter 1

Introduction

Diffractive vector meson production is one of the few processes calculable in perturbative QCD (pQCD). However, in some kinematical regions, in which the strong coupling constant is too large, pQCD is not applicable and Regge based approaches to vector meson production are necessary. The study of the transition between the "soft" nonperturbative and "hard" perturbative regimes of QCD should give important insight into the structure of strong interactions.

The HERA accelerator, located at DESY in Hamburg provides colliding beams of positrons with energy of 27.5 GeV and protons with energy of 820 GeV. For a review of the physics research carried out at the HERA collider see [1]. A large fractions of the ep interaction, in which the four-momentum exchanged between the incoming and outgoing positron is small, are interpreted in terms of photon-proton (γp) interactions. The photoproduction of vector mesons, either elastic ($\gamma p \to Vp$) or proton-dissociative ($\gamma p \to VN$) is a special kind of such processes. Measurements of vector meson production at high energies reveal the general features of a soft diffractive process, namely a weak energy dependence of the cross section, an exponential $d\sigma/dt$ dependence, and s-channel helicity conservation (SCHC) at small $-t$, the four-momentum transferred at the proton vertex. These characteristics are typical for hadron-hadron interactions and consistent with the expectations of Regge theory and the Vector meson Dominance Model (VDM) in which the photon is assumed to fluctuate into a vector meson before it interacts with the proton.

At HERA the center-of-mass energy of the colliding particles is equal to 300 GeV. The positron beam can be considered as a source of interacting virtual photons, allowing to study the photoproduction of vector mesons in a wide kinematical range. Studies of energy behavior of the exclusive diffractive ep scattering reveal that if a hard scale is present the cross section rises faster than expected for soft processes. This suggests the applicability of perturbative QCD (pQCD) calculations. A hard scale can be provided by for example the photon virtuality Q^2 or the large mass of the produced particle. For diffractive vector meson photoproduction it is expected that t, the four-momentum transferred in the proton vertex, may also provide a hard scale, assuming $-t$ is large enough [3, 4].

A recent review of the vector meson production studies conducted at HERA can be found in [2]. Until now vector meson photoproduction was the topic of several analyses in the ZEUS experiment. Elastic and proton-dissociative ρ^0 photoproduction was measured in [5] for $-t < 0.5$ GeV^2. There it was found that in the $-t$ range under study the s-channel helicity was conserved. The validity of pQCD expectations for proton-dissociative vector meson photoproduction at large $-t$ was already tested in [7] for $-t \leq 3.5$ GeV^2. A recent analysis [8] concentrated

on cross section measurements is based on the same data sample as the helicity analysis presented in this thesis. In [8] the $-t$ range is extended significantly compared to [7] and pQCD predictions for VM photoproduction concerning the production cross sections are tested more precisely. A full decay angular analysis for the exclusive electroproduction of the ρ^0 mesons was conducted in [9] for different Q^2 ranges and $-t$ extending up to 0.6 GeV^2. The violation of SCHC was observed in these measurements. Similar observations were reported by the H1 experiment at HERA both for the exclusive electroproduction of the ρ^0 mesons [10, 11] and of the ϕ mesons [12].

The analysis presented in this thesis concentrates on studying the decay angular distributions of the ρ^0, ϕ and J/ψ mesons produced in proton-dissociative diffractive photoproduction for $-t$ up to 12 GeV^2. The main goal of these measurements is to test the validity of SCHC expectations at large values of momentum transfer. The observation of SCHC violation would be one of the indications that t could provide a suitable hard scale for pQCD calculations.

A detector complimentary to the main ZEUS detector, placed in the tunnel at a distance of 44m from the interaction point in the direction of the outgoing positron, is especially dedicated to photoproduction studies at high $-t$ values. The detection of the scattered positron in this device ensures that the photon virtuality $Q^2 \leq 0.01$ GeV^2, and allows for a precise $-t$ measurement.

More than 50 institutes from 12 countries are a part of the ZEUS Collaboration. Altogether about 500 physicists are engaged in this large scale experiment. Throughout my PhD studies I was a member of the ZEUS Luminosity Monitor (LUMI) group. Within this group I contributed to the ZEUS experiment by simulating the setup and response of the luminosity detector with the EGS4 (Electron Gamma Shower) MC generator. I also took part in taking data with the ZEUS detector in the years 1997-2000 and in monitoring of the ZEUS data quality.

The data sample analyzed was collected in 1996 and 1997 with the ZEUS detector at HERA and corresponds to an integrated luminosity of 24 pb^{-1}. The vector mesons ρ^0, ϕ and J/ψ produced in proton-dissociative diffractive photoproduction at $-t < 12$ GeV^2 were selected from this data set. The helicity analysis results presented in this thesis were obtained for each of the three vector mesons with decay angular distributions corrected for non-resonant background.

This thesis is organized as follows. A short introduction to the photon-proton reactions at HERA, especially concentrated the spin state analysis of the produced vector mesons, is given in chapter 2. Chapter 3 contains the description of the HERA accelerator and the main components of the ZEUS detector. The online trigger, the reconstruction of relevant kinematical variables and off-line event selection is presented in chapter 4. Chapter 5 contains a description and applications of the Monte Carlo program used in this analysis. In chapter 6 the method of the decay angular analysis is outlined and the obtained results are presented. These results are then discussed in chapter 7, and finally the conclusions are drawn in chapter 8.

Chapter 2

Diffractive vector meson production in positron-proton collisions

In this chapter the kinematical variables describing *ep* interactions are introduced together with the relation between the *ep* and γp cross sections. Further the Vector meson Dominance Model (VDM) and the Regge phenomenology, are shortly presented. The last sections in this chapter will concentrate on the introduction to the production and decay angular distributions of the meson, analysis of which is the main goal of this thesis.

2.1 Positron-proton scattering

2.1.1 Kinematics of lepton-proton scattering

The positron-proton scattering is mediated by the exchange of a virtual vector boson. The intermediate boson may be a photon γ^* or one of the heavy, weak gauge bosons, either Z^0 or $W^\pm$. However, in the kinematical range of interest in this analysis the contribution from the Z^0 and $W^\pm$ exchange can be safely neglected. A one-photon exchange in the first order is assumed as presented in Figure 2.1. If the four-vectors are denoted by k, k', P and P' for

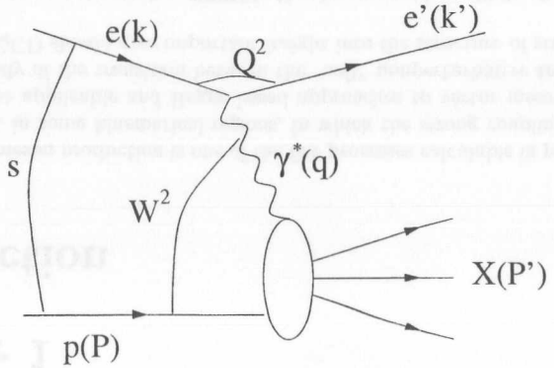

Figure 2.1: A schematic diagram of positron-proton scattering via one-photon exchange. The energy-momentum four-vectors are specified in parentheses.

the initial positron, the final positron, the incoming proton and the outgoing hadronic system respectively, the positron-proton scattering can be described in terms of the following variables:

- the square of the positron-proton center-of-mass energy

$$s = (k + P)^2 \tag{2.1}$$

- the negative square of the four-momentum of the exchanged photon

$$Q^2 = -q^2 = -(k - k')^2, \tag{2.2}$$

- the center-of-mass energy squared of the photon-proton system

$$W^2 = (q + P)^2, \tag{2.3}$$

- the fraction of the positron energy transferred to the hadronic final state in the rest frame of the initial state proton

$$y = \frac{P \cdot q}{P \cdot k}, \tag{2.4}$$

- the energy transfer from the positron to the proton in the proton rest frame

$$\nu = \frac{P \cdot q}{M_p}. \tag{2.5}$$

2.1.2 Relationship between the positron-proton and photon-proton cross sections

The differential cross section for the positron-proton scattering can be directly related to the photon-proton cross section, assuming that Q^2 is small enough ($Q^2 \ll W^2$). It can be written as

$$\frac{d^2\sigma^{ep\to eX}}{dydQ^2} = \Gamma(y, Q^2)\left(\sigma_T^{\gamma^* p\to X} + \epsilon\sigma_L^{\gamma^* p\to X}\right), \tag{2.6}$$

where $\Gamma(y, Q^2)$ denotes the photon flux

$$\Gamma(y, Q^2) = \frac{\alpha}{2\pi Q^2}\left(\frac{1 + (1-y)^2}{y} - \frac{2(1-y)}{y}\frac{Q^2_{min}}{Q^2}\right) \tag{2.7}$$

and

$$\epsilon = \frac{2(1-y)}{1 + (1-y)^2 - 2(1-y)\frac{Q^2_{min}}{Q^2}}. \tag{2.8}$$

The minimum possible value of Q^2 is denoted by $Q^2_{min} = M_e^2\frac{y^2}{1-y}$, α is the fine structure constant and M_e is the positron mass. The two functions $\sigma_T^{\gamma^* p\to X}$ and $\sigma_L^{\gamma^* p\to X}$ are the photon-proton cross sections for transversely and longitudinally polarized photons respectively, which satisfy the following relations

$$\lim_{Q^2\to 0}\sigma_T^{\gamma^* p\to X}(y, Q^2) = \sigma^{\gamma p\to X}(y), \tag{2.9}$$

$$\lim_{Q^2\to 0}\sigma_L^{\gamma^* p\to X}(y, Q^2) = 0\ . \tag{2.10}$$

It was derived in [13] that if the $Q^2 \leq Q^2_{max} \approx 0.01$ GeV^2, $\sigma_T^{\gamma^* p \to X}$ does not depend on Q^2 and the value of $\sigma_L^{\gamma^* p \to X}$ can be neglected. The differential cross section from Equation 2.6 then can be rewritten as

$$\frac{d^2\sigma^{ep\to eX}}{dydQ^2} = \Gamma(y,Q^2)\sigma^{\gamma p\to X}(y) \ . \tag{2.11}$$

Therefore one can obtain the photon-proton cross section $\sigma^{\gamma p\to X}$ from the measured positron-proton cross section $\sigma^{ep\to eX}$ by dividing the positron-proton cross section by the photon flux integrated over y and Q^2 in the range covered in the measurement.

The above conclusion also applies to the vector meson production at HERA, as the interaction process $ep \to eVX$ can be expressed by the reaction $\gamma p \to VX$

$$\frac{d^2\sigma^{ep\to eVX}}{dydQ^2} = \Gamma(y,Q^2)\sigma^{\gamma p\to VX}(y) \ . \tag{2.12}$$

2.2 Diffractive scattering

2.2.1 Vector meson Dominance Model

The Vector meson Dominance Model (VDM) [14, 15] has been quite successful in providing a good description of the photoproduction of vector mesons. The fact that photon-hadron interactions at high energies exhibit properties similar to those of the hadron-hadron interactions is the basis of this model. In this model the vector meson production is viewed as a two step process. First the photon fluctuates during a short time t_f into a virtual vector meson carrying the same quantum numbers as the photon ($J^{PC} = 1^{--}; Q = S = B = 0$). Then the vector meson scatters off the proton target, as shown in Figure 2.2. In the case of photoproduction , where the photon virtuality $Q^2 \simeq 0$, the fluctuation time t_f is given by:

$$t_f \approx \frac{2\nu}{Q^2 + M_V^2} \simeq \frac{2\nu}{M_V^2} \ , \tag{2.13}$$

where ν is the photon energy in rest frame of the proton and M_V is the mass of the vector meson.

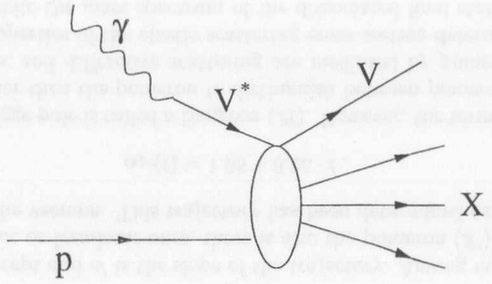

Figure 2.2: Vector meson production in the VDM. The photon fluctuates into a vector meson which then scatters off the proton.

The physical photon $|\gamma\rangle$ can therefore be considered as a superposition of a bare photon $|\gamma_B\rangle$ with a hadronic component $|h\rangle$

$$|\gamma\rangle = \sqrt{Z_3}|\gamma_B\rangle + \sqrt{\alpha}|h\rangle \ , \tag{2.14}$$

where $\sqrt{Z_3}$ is the normalization factor. VDM assumes that the light vector mesons, namely ρ^0, ω and ϕ, are the only contribution to the hadronic component $|h\rangle$ and neglects the bare photon $|\gamma_B\rangle$ contribution. A less restrictive model, the Generalized Vector Dominance model (GVD) [16], includes also other constituents which contribute to the hadronic component $|h\rangle$ of the photon.

2.2.2 Diffraction

One of the possible ways to classify hadron-hadron interactions is into so called diffractive and nondiffractive processes. In diffractive processes, the interacting particles exchange an object called the pomeron ($I\!P$), carrying the vacuum quantum numbers. The experimental signature of pomeron exchange would consist of an elastically (quasi-elastically) scattered proton, well separated in rapidity from the remaining hadronic system. Such events are therefore referred to as events with a *rapidity gap*. The differences in the characteristics of the final state allow to distinguish between three types of diffractive processes, as presented in Figure 2.3. These are :

- *elastic scattering*, in which both incident hadrons stay intact after the collision,
- *single dissociation*, where one of the interacting hadrons dissociates into a multi-particle final state, carrying the same quantum numbers as the initial hadron,
- *double dissociation*, in which both incident hadrons dissociate into multi-particle final states, again preserving the quantum numbers of these hadrons.

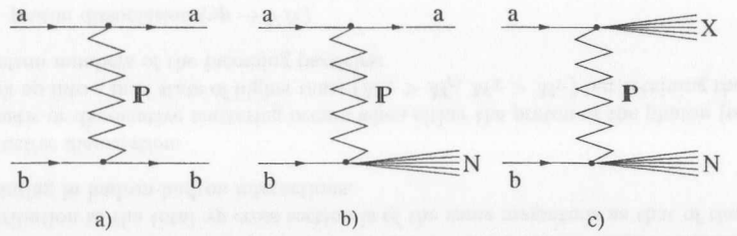

Figure 2.3: The three types of diffractive processes: a) elastic scattering, b) single dissociation, c) double dissociation.

The other class of hadron-hadron interactions includes the so called non-diffractive processes, for which the final state particles are distributed evenly without large rapidity gaps.

2.2.3 Diffraction in Terms of the Regge Formalism

The hadron-hadron interactions are well described by the Regge phenomenology [17]. The interaction is viewed as due to the exchanges of a family of off-shell particles called Regge poles in which the relevant quantum numbers are conserved. The Regge poles can be classified

into different families depending on their quantum numbers, and within one family they form a linear trajectory in the m^2,J plane, where m is the particle mass and J is its spin. The extrapolation of a trajectory to negative m^2 values yields the following parameterization in terms of the four-momentum transfer t :

$$\alpha(t) = \alpha(0) + \alpha' \cdot t \,, \tag{2.15}$$

where $\alpha(0)$ is the intercept and α' is the slope of the trajectory. Among many trajectories, like for example the mesonic or fermionic ones, there is also the pomeron ($I\!P$) trajectory, with the quantum numbers of the vacuum. This trajectory has been determined experimentally [18] as:

$$\alpha_{I\!P}(t) = 1.08 + 0.25 \cdot t \,. \tag{2.16}$$

Generally every Regge pole is called a Reggeon ($I\!R$). However, the term Reggeon is reserved for all Regge poles other then the pomeron to distinguish between pomeron and non-pomeron exchanges. The elastic and diffractive scattering are mediated by pomeron exchange in the Regge theory. The properties of the elastic scattering cross section determine the slope of the pomeron trajectory, while the mass spectrum of the dissociated final state in diffractive scattering is also directly related to its properties.

In the Regge limit, namely $-t \ll M^2 \ll s$, the total, elastic and single dissociation cross section formulae for the interaction of hadrons a and b can be written as follows:

$$\sigma_{tot}^{ab} = \sum_k \beta_{ak}(0)\beta_{bk}(0) s^{\alpha_k(0)-1} \,, \tag{2.17}$$

$$\frac{\sigma_{el}^{ab}}{dt} = \sum_k \frac{\beta_{ak}^2(t)\beta_{bk}^2(t)}{16\pi} s^{2\alpha_k(t)-2} \,, \tag{2.18}$$

$$\frac{\sigma_{sd}^{ab}}{dtdM^2} = \sum_{kl} \frac{\beta_{ak}^2(t)\beta_{bl}^2(0) g_{kkl}(t)}{16\pi} \frac{1}{M^2} \left(\frac{s}{M^2}\right)^{2\alpha_k(t)-2} \left(M^2\right)^{\alpha_l(0)-1} \,, \tag{2.19}$$

where $\beta(t)$ and $g(t)$ are vertex functions and $\alpha(t)$ is the Regge trajectory. The sum runs over all Regge trajectories for which the quantum numbers are preserved. For the elastic and single dissociative processes $k = f, I\!P$ and $l = I\!P, I\!R$. The $I\!P$ trajectory dominates the elastic and diffractive cross section.

Although the Regge phenomenology was developed in the context of hadron-hadron interactions, due the hadronic character of the photon in diffractive processes, it applies equally to the photon-hadron collisions and in particular to vector meson photoproduction.

2.2.4 Diffraction in photoproduction

The photoproduction processes can be classified in the same way as hadron-hadron interactions. Hard photoproduction processes, characterized by a typical jet-like structure of the events, are observed at high energies. However, the cross section for hard photoproduction is very small and therefore the majority of diffractive hadronic interactions occur with a limited momentum transfer $-t \ll s$ and are referred to as soft processes. The Regge theory (Section 2.2.3) describes these interactions successfully.

The soft diffractive photoproduction processes are presented in Figure 2.4 and can be classified as follows:

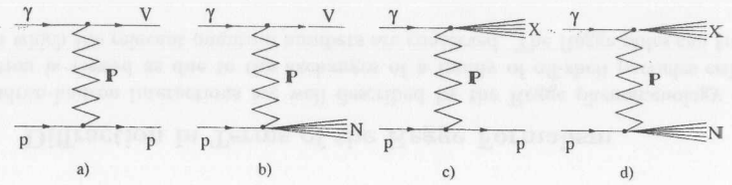

Figure 2.4: The diffractive photoproduction processes: a) elastic, b) proton dissociation, c) photon dissociation, d) double dissociation.

- *elastic diffraction* ($\gamma p \to Vp,\ V = \rho^0, \phi, J/\psi$):
  In the VDM framework this process is considered as an elastic hadron scattering. Its contribution to the total γp cross section is of the same magnitude as that of the elastic scattering in hadron-hadron interactions.

- *diffractive dissociation*:
  Inelastic or dissociative scattering occurs when either the proton or the photon (or both) break up into a final state of higher mass ($M_N > M_p$, $M_X > M_V$) but retaining the initial quantum numbers of the incoming particles:
  - proton dissociation ($\gamma p \to VN$)
  - photon dissociation ($\gamma p \to Xp$)
  - double dissociation ($\gamma p \to XN$)

2.3 Vector Meson photoproduction

The elastic and proton dissociative vector meson photoproduction processes are presented schematically in Figure 2.5. In both cases the produced vector meson decays into two charged particles, namely q^+ and q^-.

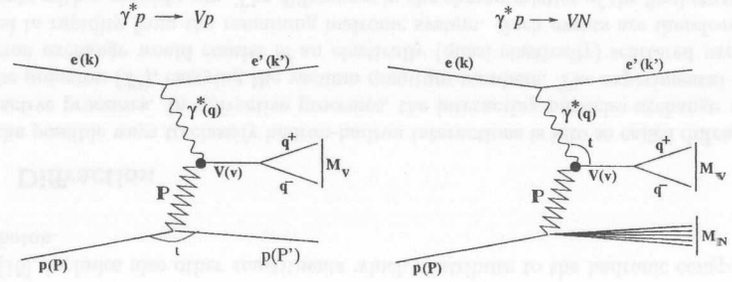

Figure 2.5: Overview of the kinematical variables describing the elastic (left) and proton-dissociative (right) vector meson photoproduction.

In the analysis of these processes additionally to the kinematical variables presented in Section 2.1 also the following ones are used:

- the squared four-momentum transferred at the $\gamma^* V$ vertex

$$t = (q - v)^2 = (P - P')^2 \ , \tag{2.20}$$

where v is the vector meson four-momentum,

- the mass of the vector meson M_V,
- the angles describing the production and decay of the vector meson,
- for the proton-dissociative reaction also the mass M_N of the diffractively produced hadronic state N, where $M_N^2 = (P')^2$.

The decay angular analysis presented in this thesis concentrates on proton-dissociative vector meson photoproduction and elastic events are regarded as background.

2.3.1 Regge theory expectations

For the case of diffractive vector meson photoproduction, assuming only $I\!P$ exchange [53], the formula for the Regge elastic cross section (Eq. (2.18)) can be approximated as follows:

$$\frac{\sigma_{\gamma p \to Vp}}{dt} \sim e^{(b^V_{0,el} + 2\alpha'_{I\!P} ln(W^2))\cdot t} \cdot \left(W^2\right)^{2\alpha_{I\!P}(0)-2} \sim e^{b^V_{el}(W)\cdot t} \cdot (W)^{4\alpha_{I\!P}(0)-4} \ , \tag{2.21}$$

where

$$b^V_{el}(W) = b^V_{0,el} + 2\alpha'_{I\!P} ln(W^2) \ . \tag{2.22}$$

The above equation is an important prediction of the Regge theory. It implies the dependence of the t slope on the energy in case $\alpha'_{I\!P}$ is non-zero. This effect is called shrinkage. The energy dependence of the elastic cross section derived by integrating Eq. (2.21) over t yields

$$\sigma_{\gamma p \to Vp} \sim \frac{(W)^{4\alpha_{I\!P}(0)-4}}{b^V_{el}(W)} \tag{2.23}$$

Assuming only $I\!P$ exchange, also Eq. (2.19) for the case of proton-dissociative, vector meson photoproduction, can be approximated as [53]:

$$\frac{\sigma_{\gamma p \to VN}}{dt dM_N^2} \sim e^{(b^V_{0,pd} + 2\alpha'_{I\!P} ln(\frac{W^2}{M_N^2}))\cdot t} \cdot \frac{1}{M_N^2} \left(\frac{W}{M_N}\right)^{4\alpha_{I\!P}(0)-4} \left[\left(M_N^2\right)^{\alpha_{I\!P}(0)-1} + R \cdot \left(M_N^2\right)^{\alpha_R(0)-1}\right] \ , \tag{2.24}$$

where the slope of the t distribution will be:

$$b^V_{pd}(W, M_N) = b^V_{0,pd} + 2\alpha'_{I\!P} ln\left(\frac{W^2}{M_N^2}\right) \ . \tag{2.25}$$

Here b^V_{pd} depends both on the energy W and the proton-dissociative mass M_N. For the proton-dissociative cross section shrinkage is predicted for non-zero $\alpha'_{I\!P}$, just as for the elastic cross section.

The ratio of the elastic to proton-dissociative differential cross section $d\sigma/dt$ is predicted to be independent of the vector meson involved in both reactions and does not depend on energy W. A comparison of these expectations with the ZEUS vector meson photoproduction data for $-t \leq 3$ GeV^2 can be found in [7].

2.3.2 Expectations from pQCD models

In pQCD models the process of diffractive photoproduction of vector mesons is viewed as a sequence of events well separated in time [19]. The sequence is as follows:

- The photon fluctuates into a $q\bar{q}$ state long before the interaction with the proton.
- the $q\bar{q}$ pair scatters on the proton target,
- the scattered $q\bar{q}$ turns into a vector meson

The fluctuation of the photon into a $q\bar{q}$ state is described by the photon wave-function derived from QCD[19]. The proton target acts as a source of color fields and thus the interaction with the $q\bar{q}$ pair is in the lowest order mediated by the exchange of two gluons in a color singlet state. This interaction can also be described by the exchange of a gluon ladder [20, 21, 23] in the leading logarithmic approximation (LLA). This process is calculable in pQCD only if a hard scale is present. In case Q^2 is approximately equal zero, like in photoproduction, the hard scale for the calculations can be provided by either the meson mass or a large enough four-momentum transfer t in the proton vertex. The transition of the $q\bar{q}$ pair into a vector meson is a non-perturbative phenomenon which can be described by the meson wave-function derived from lattice calculations and sum rules [24].

The main signs of approaching the perturbative regime in diffractive vector meson production are the following:

- The diffractive cross section is expected to rise faster with W, as a result of the increase of the gluon density in the proton [20].
- The t-dependence of the cross section is expected to be independent of the energy W, thus no shrinkage of the diffractive t-slope is predicted [21, 26].
- The differential cross section $d\sigma/dt$ is expected to follow a power-like behavior [3, 4].
- Significant breaking of SCHC is expected for light vector meson production [23, 25, 26].
- Approximate restoration of the flavor-independent production mechanism is predicted [27] (the SU(3) and SU(4) symmetries for light and heavy vector mesons respectively). From these symmetries and the quark charges the ratio of production cross sections is expected to have a relative size of $9 : 1 : 2 : 8$ for $\rho^0{:}\omega{:}\phi{:}J/\psi$.

In this thesis the hypothesis of SCHC violation is tested. In an independent study conducted on the same data sample [8] the other pQCD expectations concerning cross section measurements are tested.

2.3.3 Summary of theoretical predictions for SCHC

The hypothesis of s-channel helicity conservation (SCHC) [22] for vector meson production states that the helicity of the final state meson is equal to that of the initial photon. Studies of the elastic photoproduction of vector mesons at low $-t$ [2] show that this hypothesis is valid for soft diffractive processes.

The production of vector mesons at large $-t$ is calculated in the lowest approximation of pQCD, namely the two gluon exchange, in [25]. It is expected that for meson wave-function

chosen to be the non-relativistic delta function, appropriate for mesons consisting of heavy quarks, like for example J/ψ or Υ, the production of longitudinally polarized mesons by transverse photons vanishes. The scalar photons are expected to produce longitudinal mesons only. Therefore the hypothesis of SCHC should hold in the case of J/ψ photoproduction.

On the contrary to the above predictions for heavy mesons, for the light vector mesons, like ρ^0 or ϕ, a more detailed meson wave function [25] is appropriate. The helicity of the final state meson depends on the modeling of the photon fluctuation into a $q\bar{q}$ pair, where within the standard perturbation theory a photon can only split into a $q\bar{q}$ pair having a chiral-even spin configuration (the spins of the quark and antiquark are antiparallel). It is expected that in the range of pQCD validity, if the quark mass in the γV coupling is interpreted as current quark mass, the transverse photons will produce light vector mesons in the helicity 0 states only. This is due to the chiral nature of perturbative couplings in the massless limit. It is predicted that the production of light mesons in the helicity 0 state grows with $-t$, and also that the pQCD description for the longitudinal meson photoproduction becomes valid earlier for the ϕ meson than for the ρ^0. The bound above which the production of longitudinal vector mesons should exceed the production of mesons in helicity ± 1 state is $-t \approx 1$ GeV^2 for the ϕ and $-t \approx 5$ GeV^2 for the ρ. The previous ZEUS measurements [7] do not support these predictions.

The calculations from [25] were further developed in [26], where a new hard production mechanism for high $-t$ photoproduction was considered. The authors purpose that a large additional contribution would arise from $q\bar{q}$ fluctuations into a chiral-odd spin configuration (the helicities of the quark and antiquark are parallel), what is pictured schematically in Figure 2.6. Within standard perturbative theory a photon can only split into a $q\bar{q}$ pair with a chiral-

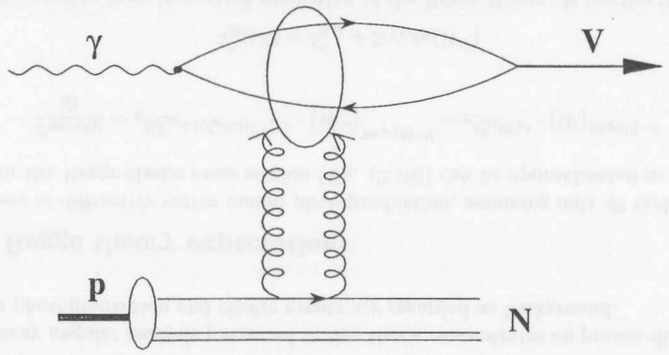

Figure 2.6: The proton dissociative photoproduction of vector mesons

even spin configuration (helicities antiparallel). In [26] all independent helicity amplitudes for the process $\gamma p \to VN$ are expressed in terms of short distance asymptotics of the light-cone wave function of the meson (photon). The contribution from the chiral-odd configuration, expected to be significant for $-t$ not asymptotically large, leads to the dominance of the helicity non-flip amplitude in a very broad region of high $-t$. The production of transversally polarized light mesons is expected to dominate up to $-t \approx 40$ GeV^2. The authors predict that in the

range $3 < -t < 8$ GeV^2, which is covered by the data analyzed in this thesis, the ratios of the helicity amplitudes are the following: $0.25 < T_{01}/T_{11} < 0.35$ and $-0.02 < T_{-11}/T_{11} < 0.04$.

These predictions will be confronted with the results of the decay angle analysis presented in this thesis.

2.4 Vector meson decay angular distributions

The angular distributions of the vector meson decay products allow to determine the spin states of the meson and to study the spin-dependent properties of the photoproduction process.

The definition of the decay angles depends on the the choice of the reference system. This thesis concentrates on the angular analysis in two reference frames, which differ in the choice of the spin-quantization axis (z-axis).

- *the helicity frame*:
  In this frame the z-axis is chosen along the vector meson direction in the γp rest frame, while the y-axis is perpendicular to the production plane (photon and meson momenta lie in this plane).
- *the transversity frame*:
  Here the z-axis is chosen along the normal to the production plane and the y-axis is taken in the direction opposite to that of the vector meson in the γp rest frame. Thus this reference frame is a result of a rotation of the helicity system around the x-axis.

By convention the direction of the positively charged decay particle is used to calculate the decay angles in both reference systems. Once the reference system has been chosen the decay can be characterized by the three planes presented schematically in Figure 2.7. The decay

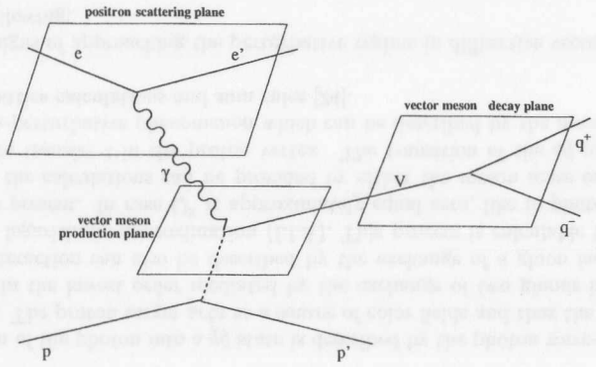

Figure 2.7: A schematical diagram of the scattering, production and decay planes in vector meson production process.

angular distribution in the most general case depends on three angles: the angle Φ_m between the positron scattering plane and the vector meson production plane, the azimuthal angle φ_m between the production plane and the meson decay plane, and the the polar angle θ_m between

the positively charged decay particle and the z-axis in the meson rest frame. The formalism used to study the spin states of the meson has been developed in [28].

The specific choice of the helicity system is motivated by the possibility to study the hypothesis of s-channel helicity conservation (SCHC), which assumes that the vector meson retains the helicity of the photon (i.e. helicity zero mesons are produced only by longitudinally polarized photons and helicity one mesons only by transversely polarized photons). The analysis in the transversity frame not only allows to draw conclusions on SCHC, through the determination of the meson spin state, but also on other properties of the photoproduction process such as for example parity conservation.

2.4.1 Spin density matrix of the photon

The spin density matrix of the photon depends on the polarization of the positron and the angle Φ. It is possible to decompose the photon spin density matrix into an orthogonal set of nine independent hermitian matrices Σ^α:

$$\rho^\gamma = \frac{1}{2}\sum_{\alpha=0}^{8} \Pi_\alpha \Sigma^\alpha \ . \tag{2.26}$$

The Σ^α matrices have the form:

$$\begin{aligned}
\Sigma^0 &= \begin{pmatrix} 1 & 0 & 0 \\ 0 & 0 & 0 \\ 0 & 0 & 1 \end{pmatrix} \quad \Sigma^1 = \begin{pmatrix} 0 & 0 & 1 \\ 0 & 0 & 0 \\ 1 & 0 & 0 \end{pmatrix} \quad \Sigma^2 = \begin{pmatrix} 0 & 0 & -i \\ 0 & 0 & 0 \\ i & 0 & 0 \end{pmatrix} \\
\Sigma^3 &= \begin{pmatrix} 1 & 0 & 0 \\ 0 & 0 & 0 \\ 0 & 0 & -1 \end{pmatrix} \quad \Sigma^4 = 2\begin{pmatrix} 0 & 0 & 0 \\ 0 & 1 & 0 \\ 0 & 0 & 0 \end{pmatrix} \quad \Sigma^5 = \frac{1}{\sqrt{2}}\begin{pmatrix} 0 & 1 & 0 \\ 1 & 0 & -1 \\ 0 & -1 & 0 \end{pmatrix} \\
\Sigma^6 &= \frac{1}{\sqrt{2}}\begin{pmatrix} 0 & -i & 0 \\ i & 0 & i \\ 0 & -i & 0 \end{pmatrix} \quad \Sigma^7 = \frac{1}{\sqrt{2}}\begin{pmatrix} 0 & 1 & 0 \\ 1 & 0 & 1 \\ 0 & 1 & 0 \end{pmatrix} \quad \Sigma^8 = \frac{1}{\sqrt{2}}\begin{pmatrix} 0 & -i & 0 \\ i & 0 & -i \\ 0 & i & 0 \end{pmatrix}
\end{aligned} \tag{2.27}$$

and the vector Π is defined as follows:

$$\begin{aligned}
\Pi \ = \ \Big[& 1, \ -\epsilon\cos 2\Phi, \ -\epsilon\sin 2\Phi, \ \frac{2M_e}{Q}(1-\epsilon)P_0, \ \epsilon+\delta, \\
& \sqrt{2\epsilon(1+\epsilon+2\delta)}\cos\Phi, \ \sqrt{2\epsilon(1+\epsilon+2\delta)}\sin\Phi, \\
& \frac{2M_e}{Q}(1-\epsilon)(P_1\cos\Phi + P_2\sin\Phi), \ \frac{2M_e}{Q}(1-\epsilon)(P_1\sin\Phi - P_2\cos\Phi)\Big] \ .
\end{aligned} \tag{2.28}$$

Here P_0, P_1 and P_2 are the components of the positron polarization vector in the Breit system and ϵ is the polarization parameter defined as the ratio of the longitudinal Γ_L to transverse Γ_T photon flux. In the laboratory frame it is expressed as follows:

$$\epsilon \equiv \frac{\Gamma_L}{\Gamma_T} = \left(1 + 2\frac{Q^2+\nu^2}{Q^2\left(1-\frac{Q^2_{min}}{Q^2}\right)^2}\tan^2\frac{\Theta}{2}\right)^{-1} \ , \tag{2.29}$$

where Θ is the positron scattering angle. For the case of $M_e \neq 0$ a mass correction parameter δ is introduced:

$$\delta = \frac{2M_e^2}{Q^2}(1-\epsilon) \ . \tag{2.30}$$

The matrices Σ^α correspond to different polarization states of the photon. So in order Σ^0 gives the unpolarized part, Σ^1 and Σ^2 represent the transverse polarization, and Σ^3 the circular polarization. The matrix Σ^4 describes longitudinally polarized photons, while matrices Σ^5–Σ^8 the interference terms between transverse and longitudinal photons.

The positron beam at HERA spontaneously polarizes due to the Sokolov-Ternov effect [29]. The positrons being bent into their circular orbit emit synchrotron photons. The spin state of a single positron can be considered with respect to the vertical bending field. Initially there is equal probability to find spins parallel or anti-parallel to the direction of the magnetic field - the beam is unpolarized. As a positron emits a synchrotron photon its spin state can either remain unchanged or can be flipped. It turns out that there is a much greater probability for spin flips from the parallel to the anti-parallel spin state than in the opposite direction. Therefore the positrons slowly build up a polarization vector anti-parallel to the bending field. At HERA the positron beam is transversely polarized up to 70% due to this effect. The interacting photons are as a result transversely polarized as well. Thus all the components of the positron polarization vector in the Breit system $P_\mu = 0$, and therefore Π_3, Π_7 and Π_8 disappear and will be no longer considered.

2.4.2 Spin density matrix of the vector meson

The spin density matrix of the vector meson ρ^V is related to that of the photon by the production amplitudes T

$$\rho^V = \frac{1}{2}T\rho^\gamma T^+ \ . \tag{2.31}$$

The production amplitudes are here introduced in the helicity representation, as in [30]:

$$T \equiv T_{\lambda_V \lambda'_p, \lambda_\gamma \lambda_p} \ , \tag{2.32}$$

where the λ's denote the helicities of the particles. As a consequence of parity conservation the helicity amplitudes obey the following relation:

$$T_{-\lambda_V -\lambda'_p, -\lambda_\gamma -\lambda_p} = (-1)^{(\lambda_V - \lambda'_p)-(\lambda_\gamma - \lambda_p)} T_{\lambda_V \lambda'_p, \lambda_\gamma \lambda_p} \tag{2.33}$$

By including the expression for the photon spin density matrix from equation (2.26) into equation (2.31) it is easy to show that also ρ^V can be decomposed into hermitian matrices:

$$\begin{aligned}
\rho_{\lambda_V \lambda'_V} &= \frac{1}{2}T\rho_{\lambda_\gamma \lambda'_\gamma}T^+ \\
&= \frac{1}{2N_\alpha}\sum_{\lambda_p \lambda'_p \lambda_\gamma \lambda'_\gamma} T_{\lambda_V \lambda'_p, \lambda_\gamma \lambda_p} \sum_{\alpha=0}^{8} \Pi_\alpha \Sigma^\alpha_{\lambda_\gamma \lambda'_\gamma} T^*_{\lambda'_V \lambda'_p, \lambda'_\gamma \lambda_p} \ , \\
&= \sum_{\alpha=0}^{8} \Pi_\alpha \rho^\alpha_{\lambda_V \lambda'_V} \ ,
\end{aligned} \tag{2.34}$$

with

$$\rho^\alpha_{\lambda_V \lambda'_V} = \frac{1}{2N_\alpha}\sum_{\alpha=0}^{8} T_{\lambda_V \lambda'_p, \lambda_\gamma \lambda_p} \Sigma^\alpha_{\lambda_\gamma \lambda'_\gamma} T^*_{\lambda'_V \lambda'_p, \lambda'_\gamma \lambda_p} \ . \tag{2.35}$$

The full spin density matrix of the vector meson expressed in terms of the hermitian matrices reads

$$\rho^V = \sum_{\alpha=0}^{8} \Pi_\alpha \rho^\alpha \ . \tag{2.36}$$

In contrast to the photon spin density matrix the meson ρ^α matrices have individual normalization factors N_α. For the transverse parts, namely $\alpha = 0 - 3$, N_α is the transverse normalization factor N_T, and for the longitudinal part ($\alpha = 4$) the longitudinal normalization factor N_L. The interference terms ($\alpha = 5 - 8$) are normalized by the geometrical mean of the transverse and longitudinal normalization factors $\sqrt{N_T N_L}$. The ratio of the longitudinal and transverse normalization factors is directly related to the ratio of cross sections for vector meson production by longitudinal and transverse photons, and is denoted by

$$R = \frac{N_L}{N_T} = \frac{\sigma_L}{\sigma_T} \ . \tag{2.37}$$

Since the matrices ρ^α are normalized individually, the vector Π_α in equation (2.36) differs from the one which appears in equation (2.26). All components of the photon Π_α vector are scaled by a factor $\frac{1}{1+(\epsilon+\delta)R}$, and additionally for $\alpha = 4$ multiplied by R, while for $\alpha = 5 - 8$ by $\sqrt{R}$.

The separation of σ_T and σ_L, and thus the determination of R, requires measurements at different ϵ, i.e. at different positron scattering angles Θ for fixed Q^2 and W. If no such separation is performed, as is the case in this analysis, the contributions from $\rho^0_{\lambda\lambda'}$ and $\rho^4_{\lambda\lambda'}$ cannot be measured independently. The following matrix elements can be determined, being a linear combination of the vector meson spin density matrix elements:

$$r^{04}_{ik} = \frac{\rho^0_{ik} + (\epsilon+\delta)R\rho^4_{ik}}{1+(\epsilon+\delta)R} \tag{2.38}$$

$$r^{\alpha}_{ik} = \frac{\rho^\alpha_{ik}}{1+(\epsilon+\delta)R} \qquad \alpha = 1,2 \tag{2.39}$$

$$r^{\alpha}_{ik} = \frac{\sqrt{R}\rho^\alpha_{ik}}{1+(\epsilon+\delta)R} \qquad \alpha = 5,6 \tag{2.40}$$

where the subscripts i and k run over the possible helicity states -1, 0 and $+1$. The superscript 0 corresponds to the case of unpolarized transverse photons, while superscript 4 represents the contribution from longitudinally polarized photons. The superscripts 1 and 2 indicate terms arising from in the case of linearly polarized transverse photons and superscripts 5 and 6 indicate the interference between the longitudinal and transverse amplitudes. With these new matrix elements the vector meson spin density matrix can be written in the form:

$$\rho^V_{\lambda_V\lambda'_V} = \sum_\beta \Pi_\beta r^\beta_{\lambda_V\lambda'_V} \ , \qquad \beta = 04,1,2,3,5,\ldots,8. \tag{2.41}$$

2.4.3 Decay angular distribution

The decay angular distribution of the meson decay products in its rest frame reads [31]:

$$W(\cos\theta,\phi) = M\rho^V M^+ = \sum_{\lambda_V\lambda'_V} \langle\theta,\phi|M|\lambda_V\rangle\rho^V_{\lambda_V\lambda'_V}\langle\lambda'_V|M^+|\theta,\phi\rangle \tag{2.42}$$

where M is the decay amplitude and for the meson decay into spinless particles

$$\langle\theta,\phi|M|\lambda_V\rangle = C\sqrt{\frac{3}{4\pi}}D^{1*}_{\lambda_V 0}(\phi,\theta,-\phi) \tag{2.43}$$

The quantity C is set equal to one, as decay angular distributions considered here are normalized. The Wigner rotation functions for $J = 1$ are as follows:

$$D^1_{10}(\phi,\theta,-\phi) = -\frac{1}{\sqrt{2}}\sin\theta e^{-i\phi} \tag{2.44}$$

$$D^1_{00}(\phi,\theta,-\phi) = \cos\theta \tag{2.45}$$

$$D^1_{-10}(\phi,\theta,-\phi) = \frac{1}{\sqrt{2}}\sin\theta e^{i\phi} \tag{2.46}$$

As a consequence of parity conservation and the symmetry properties of the Σ^α matrices, the ρ^α matrices obey the following symmetry relation:

$$\rho^\alpha_{-\lambda_V-\lambda'_V} = C_\alpha(-1)^{\lambda_V-\lambda'_V}\rho^\alpha_{\lambda_V\lambda'_V} \ , \tag{2.47}$$

with the constants:

$$C_\alpha = \begin{cases} 1 & : \ \alpha = 0,1,4,5,8 \\ -1 & : \ \alpha = 2,3,6,7 \end{cases} \tag{2.48}$$

Based on the hermicity of the vector meson spin density matrix

$$\rho^V_{\lambda_V\lambda'_V} = \rho^{V*}_{\lambda_V\lambda'_V} \tag{2.49}$$

its diagonal elements must be real. The symmetry relation in Equation 2.47 reduces the number of independent matrix elements, and furthermore for $C_\alpha = 1$ the matrix elements ρ^α_{1-1} is purely real, while for $C_\alpha = -1$ purely imaginary. The real part of the elements ρ^α_{10} can be extracted for $C_\alpha = 1$, while for $C_\alpha = -1$ the imaginary part.

The full decay angular distribution, in case R is not known, can be obtained by substituting the vector meson spin density matrix in Equation 2.42 with the linear combinations of it's elements from Equations 2.38, 2.39 and 2.40. The resulting normalized three-dimensional angular distribution can be expressed as a function of 15 independent elements.

$$\begin{aligned} W(\cos\theta_m,\varphi_m,\Phi_m) = \frac{3}{4\pi}\Big[&\Big(\frac{1}{2}(1-r^{04}_{00}) + \frac{1}{2}(3r^{04}_{00}-1)\cos^2\theta_m \\ &-\sqrt{2}\mathrm{Re}(r^{04}_{10})\sin 2\theta_m\cos\varphi_m - r^{04}_{1-1}\sin^2\theta_m\cos 2\varphi_m\Big) \\ &-\epsilon\cos 2\Phi_m\left(r^1_{11}\sin^2\theta_m + r^1_{00}\cos^2\theta_m\right. \\ &\left.-\sqrt{2}\mathrm{Re}(r^1_{10})\sin 2\theta_m\cos\varphi_m - r^1_{1-1}\sin^2\theta_m\cos 2\varphi_m\right) \\ &-\epsilon\sin 2\Phi_m\left(\sqrt{2}Im(r^2_{10})\sin 2\theta_m\sin\varphi_m + Im(r^2_{1-1})\sin^2\theta_m\sin 2\varphi_m\right) \\ &+\sqrt{2\epsilon(1+\epsilon+\delta)}\cos\Phi_m\left(r^5_{11}\sin^2\theta_m + r^5_{00}\cos^2\theta_m\right. \\ &\left.-\sqrt{2}\mathrm{Re}(r^5_{10})\sin 2\theta_m\cos\varphi_m - r^5_{1-1}\sin^2\theta_m\cos 2\varphi_m\right) \\ &+\sqrt{2\epsilon(1+\epsilon+\delta)}\sin\Phi_m\left(\sqrt{2}Im(r^6_{10})\sin 2\theta_m\sin\varphi_m\right. \\ &\left.+Im(r^6_{1-1})\sin^2\theta_m\sin 2\varphi_m\right)\Big]. \end{aligned} \tag{2.50}$$

2.4.4 The s-channel helicity frame

The production and decay angles as defined in the s-channel helicity frame are presented in Fig.2.8. This frame is defined as the rest frame of the vector meson in which the meson direction in the $\gamma^* p$ center-of-mass frame is taken as the quantization axis. The polar angle θ_h is

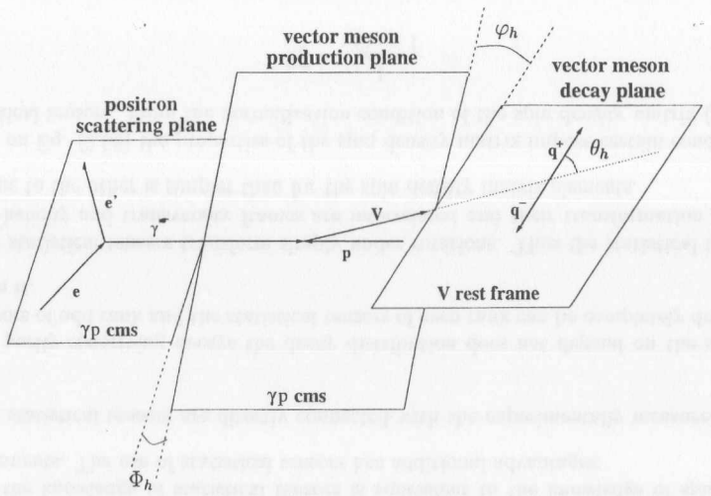

Figure 2.8: The definition of the planes and angles used to describe the production and decay of the vector meson into two charged particles (q^+,q^-)

the angle between the direction of the outgoing meson and the direction of one of the decay particles - by convention the positively charged one. The azimuthal angle φ_h is defined as the angle between the vector meson decay plane and the meson production plane, while Φ_h is the angle between the meson production plane and the positron scattering plane.

The full decay angular distribution can be expressed as a function of all three angles as in Equation (2.50). Since in this analysis the angle Φ_h is not measured, one can integrate the overall decay angular distribution over this angle. Then for an unpolarized positron beam and a decay into two spin-0 particles the angular distribution reduces to

$$\begin{aligned} W(\cos\theta_h, \varphi_h) = \; & \tfrac{3}{4\pi}\left[\tfrac{1}{2}(1 - r^{04}_{00}) + \tfrac{1}{2}(3r^{04}_{00} - 1)\cos^2\theta_h \right. \\ & -\sqrt{2}\mathrm{Re}\,(r^{04}_{10})\sin 2\theta_h \cos\varphi_h \\ & \left. -r^{04}_{1-1}\sin^2\theta_h \cos 2\varphi_h\right]. \end{aligned} \tag{2.51}$$

After further integration over φ_h or $\cos\theta_h$ one obtains the following one-dimensional angular distributions:

$$W(\cos\theta_h) = \frac{3}{4}\left[1 - r^{04}_{00} + \left(3r^{04}_{00} - 1\right)\cos^2\theta_h\right] \tag{2.52}$$

$$W(\varphi_h) = \frac{1}{2\pi}\left(1 - r^{04}_{1-1}\cos 2\varphi_h\right). \tag{2.53}$$

In these equations r^{04}_{00}, r^{04}_{10} and r^{04}_{1-1} are the vector meson spin density matrix elements. The r^{04}_{00} element represents the probability that the vector meson is produced in a helicity zero state. The r^{04}_{10} element is related to the interference between helicity single-flip and helicity non-flip amplitudes, while the element r^{04}_{1-1} is related to the interference between helicity double-flip and helicity non-flip amplitudes.

As the contribution from photons in helicity 0 state is negligible, these matrix elements are related to the helicity amplitudes $T_{\lambda_V \lambda_\gamma}$ as follows [28]:

$$r^{04}_{00} \approx \frac{T^2_{01}}{T^2_{01} + T^2_{11} + T^2_{-11}}, r^{04}_{10} \approx \frac{1}{2}\frac{(T_{11}T^*_{01}) + (T_{-11}T^*_{01})}{T^2_{01} + T^2_{11} + T^2_{-11}}, r^{04}_{1-1} \approx \frac{1}{2}\frac{(T_{11}T^*_{-11}) + (T_{-11}T^*_{11})}{T^2_{01} + T^2_{11} + T^2_{-11}}, \tag{2.54}$$

where T_{11} is the helicity non-flip amplitude, T_{01} is the helicity single-flip amplitude and T_{-11} is the helicity double-flip amplitude. If SCHC holds, only the T_{11} amplitude is non-zero, and therefore r^{04}_{00}, r^{04}_{10} and r^{04}_{1-1} should all be equal zero.

Equation (2.51) is valid for a decay into two spin-0 particles, namely for $\rho^0 \to \pi^+\pi^-$ and $\phi \to K^+K^-$. When however dealing with a decay into two spin-1/2 particles, as for $J/\psi \to e^+e^-$ or $J/\psi \to mu^+\mu^-$, it must be replaced by

$$\begin{aligned} W(\cos\theta_h, \varphi_h) = \; & \tfrac{3}{4\pi}\left[\tfrac{1}{2}(1 + r^{04}_{00}) - \tfrac{1}{2}(3r^{04}_{00} - 1)\cos^2\theta_h \right. \\ & +\sqrt{2}\mathrm{Re}\,(r^{04}_{10})\sin 2\theta_h \cos\varphi_h \\ & \left. +r^{04}_{1-1}\sin^2\theta_h \cos 2\varphi_h\right]. \end{aligned} \tag{2.55}$$

After further integration over φ_h or $\cos\theta_h$ the following one-dimensional angular distributions are obtained:

$$W(\cos\theta_h) = \frac{3}{8}\left[1 + r^{04}_{00} - \left(3r^{04}_{00} - 1\right)\cos^2\theta_h\right] \tag{2.56}$$

$$W(\varphi_h) = \frac{1}{2\pi}\left(1 + r^{04}_{1-1}\cos 2\varphi_h\right). \tag{2.57}$$

Equations (2.52) and (2.53) were fitted to the background subtracted and acceptance corrected, one-dimensional, angular distributions in data in four t bins for ρ^0 and in three t bins for ϕ. In the case of the J/ψ the angular distribution equations (2.56) and (2.57) were fitted to the data in two t bins. The vector meson spin density matrix elements r^{04}_{00} and r^{04}_{1-1} were treated as fit parameters. The whole procedure of the decay angular analysis will be explained in more detail in the next chapters.

2.4.5 The transversity frame

The transversity frame is connected to the helicity frame through a rotation by $-\frac{\pi}{2}$ around the x-axis. The quantization axis z is perpendicular to the reaction plane in the transversity frame, as shown schematically in Fig. 2.9.

The angular distribution of the meson decay products can be expressed in terms of the statistical tensors with the angles θ_t and φ_t measured in the transversity frame. The main features of the statistical tensors and the decay angular distribution in the transversity frame are described in the next section.

2.4.6 The decay angular distribution in terms of statistical tensors

The statistical tensors can be used, instead of spin density matrix elements, to parameterize the decay angular distribution of resonances. They can be easily determined by means of calculating the average value of relevant spherical harmonics over the angular distribution. Especially in the transversity frame the statistical tensors have a particularly straightforward physical interpretation as will be presented below. In this thesis the analysis with the use of statistical

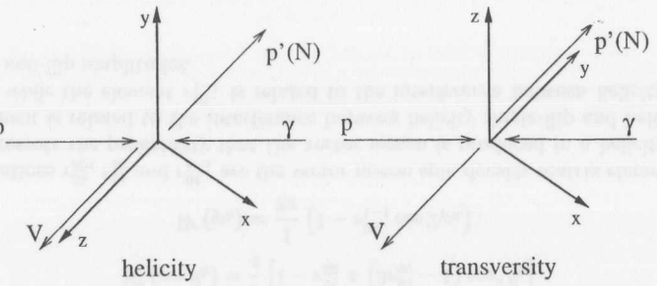

Figure 2.9: The helicity and transversity reference frames for the vector meson V. The arrows denote the momenta of the incoming proton (p), photon (γ), vector meson (V) and the outgoing proton (p') or proton dissociative system (N) respectively.

tensors serves as a cross-check to the results obtained by fitting the spin density matrix elements to the decay angular distribution in the helicity frame.

The decay angular distribution can be expressed in a simple way in terms of the statistical tensors which are defined as follows [32]:

$$T^J_M = \sum_{mm'} (-1)^{s+m-J} C(s, -m; s, m'|J, M) \rho_{mm'} \ , \tag{2.58}$$

where s is the spin of the decaying particle, $C(\ )$ the Clebsh-Gordan coefficients and $\rho_{mm'}$ the spin density matrix. From the orthogonality of the Clebsh-Gordan coefficients an inverse relation is easily obtained:

$$\rho_{mm'} = \sum_{JM} (-1)^{s+m-J} C(s, -m; s, m'|J, M) T^J_M \ , \tag{2.59}$$

therefore the knowledge of statistical tensors is equivalent to the knowledge of spin density matrix elements. The use of statistical tensors has additional advantages:

- The statistical tensors are directly connected with the experimentally measured quantities.
- For parity-conserving decays the decay distribution does not depend on the statistical tensors of odd rank and the statistical tensors of even rank can be completely determined from it.
- The statistical tensors transform simply under rotations. Thus the statistical tensors in the helicity and transversity frames are interrelated and their transformation from one frame to the other is simpler than for the spin density matrix elements.

Based on Eq. (2.58) the properties of the spin density matrix impose certain conditions on the statistical tensors. From the normalization condition of the spin density matrix ($Tr\rho = 1$) follows:

$$T^0_0 = \frac{1}{\sqrt{2s+1}} \tag{2.60}$$

The hermicity of the ρ-matrix ($\rho = \rho^+$) leads to the relation

$$T^{J^*}_M = (-1)^M T^J_{-M} \tag{2.61}$$

which allows to determine only the statistical tensors of rank $M \geq 0$ in the analysis. Parity conservation in the transversity frame, namely:

$$\rho_{mm'} = 0 \qquad \text{for } m - m' \text{ odd} \tag{2.62}$$

leads to the following relation in terms of the statistical tensors:

$$T^J_M = 0 \qquad \text{for } M \text{ odd} \tag{2.63}$$

The decay angular distribution in terms of the statistical tensors can be derived [32, 33] starting from the density of probability for finding the decay products at angles θ_t and φ_t in their center-of-mass system. This probability density is denoted by the formula:

$$W(\theta_t, \varphi_t) = N \sum_{mm'\Lambda} A_{m\Lambda}(\theta_t, \varphi_t)\, \rho_{mm'}\, A^*_{m'\Lambda}(\theta_t, \varphi_t) \ , \tag{2.64}$$

where the angles θ_t and φ_t are decay angles of the meson measured in the transversity frame, and N is the normalization constant. Further $A_{m\Lambda}(\theta_t, \varphi_t)$ is the decay amplitude, m is the projection of the meson spin in the transversity frame and $\Lambda = \lambda_1 - \lambda_2$ is the difference of helicities of the produced decay particles. The decay amplitude can be written as:

$$A_{m\Lambda}(\theta_t, \varphi_t) = M(\lambda_1, \lambda_2) D^{s^*}_{m\Lambda}(\varphi_t, \theta_t, 0) \ , \tag{2.65}$$

where $M(\lambda_1, \lambda_2)$ is a constant depending on the decay dynamics. For parity conserving decay processes it satisfies the relation:

$$M(\lambda_1, \lambda_2) = \eta(-1)^{s-s_1-s_2} M(-\lambda_1, -\lambda_2) \ . \tag{2.66}$$

Here η is the product of the intrinsic parities of the decaying resonance and the decay products, whereas s, s_1 and s_2 are the spins of these particles respectively. From equations (2.64) and (2.65) follows:

$$W(\theta_t, \varphi_t) = N \sum_{mm'\lambda_1\lambda_2} |M(\lambda_1, \lambda_2)|^2\, \rho_{mm'}\, D^{s^*}_{m\Lambda}(\varphi_t, \theta_t, 0)\, D^s_{m'\Lambda}(\varphi_t, \theta_t, 0) \tag{2.67}$$

Taking into account the following property of the rotation matrix:

$$D^{s^*}_{m\Lambda}(\varphi_t, \theta_t, 0) = (-1)^{m-\Lambda} D^s_{-m-\Lambda}(\varphi_t, \theta_t, 0) \tag{2.68}$$

the probability density $W(\theta_t, \varphi_t)$ can be rewritten as:

$$W(\theta_t, \varphi_t) = N \sum_{mm'\lambda_1\lambda_2} |M(\lambda_1, \lambda_2)|^2\, \rho_{mm'}\, (-1)^{m-\Lambda} D^s_{-m-\Lambda}(\varphi_t, \theta_t, 0)\, D^s_{m'\Lambda}(\varphi_t, \theta_t, 0) \tag{2.69}$$

When expressing the spin density matrix elements by the statistical tensor components using Eq.(2.59) we obtain:

$$W(\theta_t, \varphi_t) = \sum_{JM} N \sum_{mm'\lambda_1\lambda_2} |M(\lambda_1, \lambda_2)|^2 (-1)^{m-\Lambda} D^s_{-m-\Lambda}(\varphi_t, \theta_t, 0) D^s_{m'\Lambda}(\varphi_t, \theta_t, 0) \times (-1)^{s+m-J} C(s, -m; s, m'|J, M) T^J_M \tag{2.70}$$

The two rotation matrices D when coupled together eventually give a spherical harmonic:

$$\sum_{mm'} D^{s}_{-m-\Lambda}(\varphi_t,\theta_t,0) D^{s}_{m'\Lambda}(\varphi_t,\theta_t,0)\, C(s,-m;s,m'|J,M) = \\ = D^{J}_{m'-m,0}(\varphi_t,\theta_t,0)\, C(s,-\lambda;s,\Lambda|J,0) = \\ = \sqrt{\frac{4\pi}{2J+1}}\, Y^{J^*}_{M}(\theta_t,\varphi_t)\, C(s,-\Lambda;s,\Lambda|J,0) \tag{2.71}$$

When substituting the result of Eq. (2.71) into Eq. (2.70) we obtain:

$$W(\theta_t,\varphi_t) = \sum_{JM} N \sum_{\lambda_1\lambda_2} \sqrt{\tfrac{4\pi}{2J+1}} |M(\lambda_1,\lambda_2)|^2 (-1)^{J-s-\Lambda}\, T^{J}_{M} \times \\ \times Y^{J^*}_{M}(\theta_t,\varphi_t)\, C(s,-\Lambda;s,\Lambda|J,0) \tag{2.72}$$

The angular decay distribution in the above equation can be rewritten as

$$W(\theta_t,\varphi_t) = \sum_{JM} F(J)\, T^{J}_{M}\, Y^{J^*}_{M}(\theta_t,\varphi_t)\ , \tag{2.73}$$

where $F(J)$ is:

$$F(J) = N\sqrt{\frac{4\pi}{2J+1}} \sum_{\lambda_1,\lambda_2} |M(\lambda_1,\lambda_2)|^2\, (-1)^{J-s-\Lambda}\, C(s,-\Lambda;s,\Lambda|J,0) \tag{2.74}$$

The normalization condition for the spherical harmonics is the following:

$$\int d\cos\theta_t d\varphi_t Y^{J^*}_{M}(\theta_t,\varphi_t) Y^{J'}_{M'}(\theta_t,\varphi_t) = \delta_{JJ'}\delta_{MM'} \tag{2.75}$$

From this normalization condition and Eq. (2.73) the following important relation can be obtained:

$$F(J)T^{J}_{M} = \int d\cos\theta_t d\varphi_t W(\theta_t,\varphi_t) Y^{J}_{M}(\theta_t,\varphi_t) = \langle Y^{J}_{M}(\theta_t,\varphi_t)\rangle \tag{2.76}$$

The statistical tensors can therefore be evaluated experimentally from the decay angular distribution by calculating the average of the corresponding spherical harmonics and dividing this average by $F(J)$. Here $F(J)$ are constant coefficients depending on the rank of the tensor and the decay dynamics. They can be easily evaluated starting from calculating equation (2.76) for $J = 0$ and $M = 0$:

$$F(0)T^{0}_{0} = \frac{1}{\sqrt{4\pi}} \tag{2.77}$$

From equation (2.60) the following result is obtained for $F(0)$:

$$F(0) = \sqrt{\frac{2s+1}{4\pi}} \tag{2.78}$$

With the following property of the Clebsh-Gordan coefficients:

$$C(s,-\Lambda;s,\Lambda|J,0) = (-1)^{s-J-\Lambda}\sqrt{\frac{2J+1}{2s+1}} C(s,\Lambda;J,0|s,\Lambda) \tag{2.79}$$

equation (2.74) can be rewritten in the form:

$$F(J) = N\sqrt{\frac{4\pi}{2s+1}} \sum_{\lambda_1,\lambda_2} |M(\lambda_1,\lambda_2)|^2\, C(s,\Lambda;J,0|s,\Lambda)\ . \tag{2.80}$$

Therefore for $J = 0$

$$F(0) = N\sqrt{\frac{4\pi}{2s+1}} \sum_{\lambda_1,\lambda_2} |M(\lambda_1,\lambda_2)|^2\ . \tag{2.81}$$

By combining Eq. (2.78) and the above relation we get:

$$N \sum_{\lambda_1,\lambda_2} |M(\lambda_1,\lambda_2)|^2 = \frac{2s+1}{4\pi}\ . \tag{2.82}$$

Equation (2.82) together with the following property of the Clebsh-Gordan coefficients:

$$C(s,\Lambda;J,0|s,\Lambda) = (-1)^{J} C(s,-\Lambda;J,0|s,-\Lambda) \tag{2.83}$$

lead to the final result for the coefficients $F(J)$:

$$F(J) = \sqrt{\frac{2s+1}{4\pi}} C(s,\Lambda;J,0|s,\Lambda) \qquad \text{for even } J \tag{2.84}$$

$$F(J) = 0 \qquad \text{for odd } J \tag{2.85}$$

Among parity conserving decays one of the most frequent is $1^- \to 0^- + 0^-$. Good examples of such decays are those studied in this thesis, namely $\rho \to \pi^+\pi^-$ and $\phi \to K^+K^-$. For both these decays only even-J tensors appear in the decay distribution. Since the tensor T^0_0 is trivial (see Eq. (2.60)) the decay angular distribution contains only spherical harmonics Y^2_M and thus depends only on the tensor T^2_M. The only relevant coefficient $F(2)$ from Eq. (2.84) is equal:

$$F(2) = -\sqrt{\frac{3}{10\pi}} \tag{2.86}$$

Therefore the spherical harmonics which will be of use in the analysis are the following:

$$Y^2_0 = \sqrt{\frac{5}{4\pi}}\left(\frac{3}{2}\cos^2\theta_t - \frac{1}{2}\right) \tag{2.87}$$

$$Y^2_1 = -\sqrt{\frac{15}{8\pi}} \sin\theta_t \cos\theta_t e^{i\varphi_t} \tag{2.88}$$

$$Y^2_2 = \frac{1}{4}\sqrt{\frac{15}{4\pi}} \sin^2\theta_t e^{2i\varphi_t}. \tag{2.89}$$

Furthermore the mean values of the spherical harmonics defined as in Eq. (2.76) should be equal zero in case M is odd (see equation (2.63)).

According to the following formulae the statistical tensors of rank 2 in the helicity frame can be expressed by the statistical tensors of the same rank in the transversity frame [33]:

$${}^{h}T^2_2 = \frac{1}{2}\mathrm{Re}T^2_2 - \frac{\sqrt{6}}{4}T^2_0 \tag{2.90}$$

$${}^{h}T^2_1 = -\mathrm{Im}T^2_2 \tag{2.91}$$

$${}^{h}T^2_0 = -\frac{\sqrt{6}}{2}\mathrm{Re}T^2_2 - \frac{1}{2}T^2_0 \tag{2.92}$$

The statistical tensors can be expressed in terms of the transversity density matrix elements as follows:

$$T^2_2 = \rho_{-11} \tag{2.93}$$

$$T^2_0 = \frac{1}{\sqrt{6}}(\rho_{11} - 2\rho_{00} + \rho_{-1-1}) \tag{2.94}$$

The formulae above remain valid in the helicity frame in which in addition:

$$T_1^2 = -\sqrt{2}\mathrm{Re}\rho_{10} \tag{2.95}$$

Taking into account the normalization condition of the spin density matrix ($Tr\rho = 1$) and its symmetry property for parity conserving decays given by equation (2.47) the above equations (2.93) – (2.95) in the helicity frame can be rearranged to give the relevant spin density matrix elements.

$$\rho_{00} = \frac{1}{\sqrt{3}}\,{}^hT_0^0 - \sqrt{\frac{2}{3}}\,{}^hT_0^2 = \frac{1}{3} - \sqrt{\frac{2}{3}}\,{}^hT_0^2 \tag{2.96}$$

$$\mathrm{Re}\rho_{10} = -\frac{1}{\sqrt{2}}\,{}^hT_1^2 \tag{2.97}$$

$$\rho_{-11} = \rho_{1-1} = {}^hT_2^2 \tag{2.98}$$

In the analysis the spin density matrix elements in the helicity frame are obtained indirectly starting from the determination of the statistical tensors in the transversity frame and following the steps described above. This procedure should serve as a good cross-check for spin density matrix elements obtained in the helicity frame by means of fitting the decay angular distribution.

Chapter 3

The ZEUS detector at HERA

In this chapter an overview of the HERA accelerator and the ZEUS experiment is presented. The components of the ZEUS detector particularly important in this analysis are then briefly described.

3.1 The HERA collider

The HERA (Hadron-Elektron Ring Anlage) accelerator [34] is the world's first lepton-hadron collider built at the DESY (Deutsches Elektronen Synchrotron) laboratory in Hamburg, Germany. This collider offers the unique possibility to study the scattering of electrons (or positrons) with energy about 30 GeV on 820 GeV protons. A schematic view of HERA, together with all the preaccelerators, is presented in Figure 3.1.

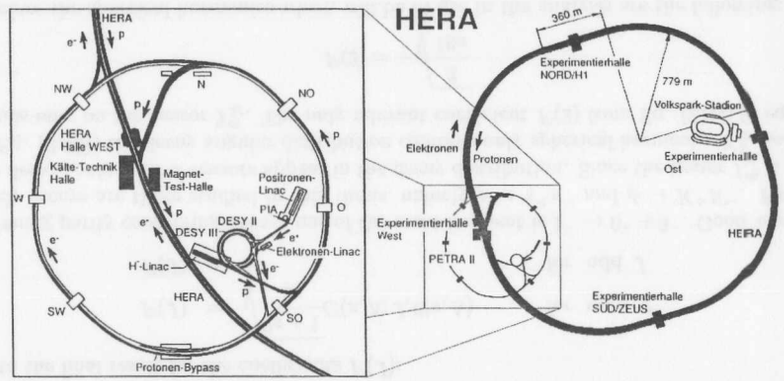

Figure 3.1: The layout of HERA with the location of different experimental halls and a blow-up picture of the preaccelerators.

The particle beams are initially accelerated in a system of linear (LINAC I, LINAC II, H^- LINAC) and circular (DESY II, DESY III, PETRA II) accelerators. From PETRA II, 14 GeV electrons and 40 GeV protons are injected into the main accelerator HERA, where they reach the collision energies of 27.5 GeV and 820 GeV respectively. Along HERA there are four

experimental halls, two of which are occupied by the two main collision experiments – ZEUS (in the south hall) and H1 (in the north hall). The remaining two halls house experiments which use either the electron beam (HERMES) or the proton beam (HERA-B) only. HERMES is designed to study the nucleon spin structure by scattering longitudinally polarized photons off polarized gas targets. HERA-B uses wire targets to produce B-mesons in the proton beam halo, in order to study CP violation in the $B^0\bar{B}^0$ system.

The HERA collider consists of two storage rings, each with a diameter of 6.3 km, placed in a tunnel 10-25 m underground. The use of superconducting dipole magnets, providing a magnetic field of 4.68 T, is necessary to keep the protons with energy of 820 GeV on a circular orbit. Contrary to that, the magnetic field provided by conventional dipole magnets is sufficient to guide the 27.5 GeV electrons along their orbit. The electron and proton beams circulate at HERA in opposite directions and collide at zero crossing angle at two points, around which the ZEUS and H1 detectors are installed. The center of mass energy of the colliding particles, $\sqrt{s} = 300$ GeV, is equivalent to the energy attainable in a collision of a 48 TeV electron beam with a fixed proton target.

HERA parameter	designed value	1996	1997
proton energy (GeV)	820	820	820
positron energy (GeV)	30	27.5	27.5
number of positron bunches	210	177+28	176+20
number of proton bunches	210	177+3	176+5
positron beam current (mA)	58	23	30
proton beam current (mA)	163	60	75
bunch crossing time (ns)	96	96	96
beam σ_x at the IP (mm)	0.30(e^-) 0.27(p)	0.27(e^+) 0.18(p)	0.27(e^+) 0.18(p)
beam σ_y at the IP (mm)	0.06(e^-) 0.09(p)	0.06(e^+) 0.06(p)	0.06(e^+) 0.06(p)
beam σ_z at the IP (mm)	80(e^-) 110(p)	80(e^+) 110(p)	80(e^+) 110(p)
instantaneous luminosity ($cm^{-2}s^{-1}$)	$1.7 \cdot 10^{31}$	$3.8 \cdot 10^{30}$	$5.6 \cdot 10^{30}$
specific luminosity ($cm^{-2}s^{-1}A^{-2}$)	$3.9 \cdot 10^{29}$	$5.3 \cdot 10^{29}$	$5.7 \cdot 10^{29}$
integrated luminosity (pb^{-1}/year)	35	17.6	36.35

Table 3.1: Design and operational values of the main HERA parameters.

The beams at HERA are bunched, with each beam carrying at the most 210 bunches of particles, which cross at the two interaction points (IP) every 96 ns. During standard operation both beams at HERA are not completely filled with bunches. Unpaired bunches, also referred to as pilot bunches, can be used to estimate beam related background rates. Empty bunch buckets, passing through the Interaction Region enable the study and estimation of background rates due to cosmic rays. In 1996 HERA operated with 177 colliding positron and proton bunches, 28 positron and 3 proton pilot bunches. In 1997 there were 176 ep bunches with 20 positron and 5 proton unpaired bunches. Table 3.1 summarizes the design [35] and operational performance of HERA in 1996 and 1997.

3.2 The ZEUS detector

The ZEUS detector is installed in the south experimental hall of the HERA ring. It consists of a number of specialized subdetectors, dedicated to high precision energy measurement and tracking of particles created in ep interactions. The ZEUS detector as a whole, with the different components indicated is presented schematically in Fig. 3.2.

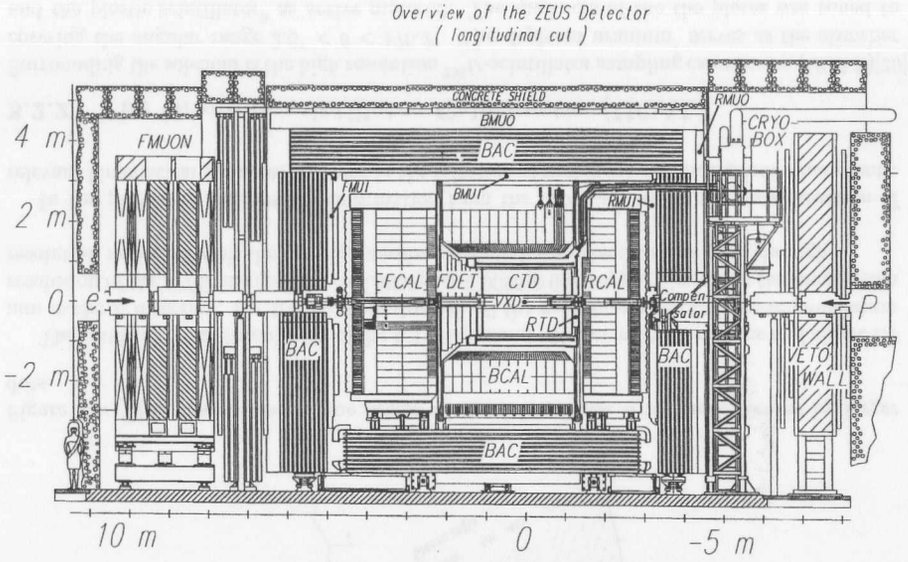

Figure 3.2: The YZ cross-section view of the ZEUS detector.

The coordinate system referred to in this thesis is the so called ZEUS coordinate system. It is defined such that its origin is at the nominal positron-proton interaction point (IP) inside the ZEUS detector. The Z-axis points in the proton beam direction, called also the forward direction. The X-axis points towards the center of the HERA ring and the Y-axis points upwards. The angular coordinates are defined as follows: $\theta \in [0, \pi]$ is the polar angle with respect to the positive Z direction and $\phi \in [0, 2\pi]$ is the azimuthal angle around the Z-axis with respect to the positive X direction. It is sometimes more convenient to use also two other variables, namely the radius $r = \sqrt{X^2 + Y^2}$ and the so called pseudorapidity defined as $\eta = -ln(tg\theta/2)$.

The design and construction of the ZEUS detector account for the large forward-backward asymmetry of the event topology in the final state, resulting from the highly different energies of the incoming protons and positrons.

The innermost components of the ZEUS detector are the drift chambers, which measure the tracks of charged particles emerging from the IP. These are the Central Tracking Detector (CTD), Forward (FDET) and Rear (RTD) Tracking Devices. The Vertex Detector (VXD), still present in Fig. 3.2 was removed before the 1996 data taking period. The tracking detectors are surrounded by a superconducting solenoid providing an axial field of 1.43 T, which enables the determination of the momenta of charged particles from the curvature of their tracks.

A high resolution uranium-scintillator calorimeter (UCAL), devoted to the measurement of the particles' energies, is installed around the tracking devices. It consists of three parts, being the barrel calorimeter (BCAL), the Forward Calorimeter (FCAL) and the Rear Calorimeter (RCAL). The Backing Calorimeter (BAC), constructed of proportional tube chambers surrounding the UCAL, allows for the correction and rejection of showers leaking from the uranium calorimeter. It is also very useful for identifying muons.

Particles which penetrate the material of the UCAL and the BAC are identified as muons and are detected in the barrel (BMUON), forward (FMUON) and rear (RMUON) muon chambers. These detectors are built of drift- and limited streamer tube chambers and each is divided into an inner (BMUI,FMUI,RMUI) and an outer (BMUO,FMUO,RMUO) part. The inner parts of these detectors are mounted before while the outer ones after the magnetized iron yoke.

The ZEUS detector has been operated with additional components mounted at some distance from the main detector along the beam line. Situated at the back of RCAL at $Z = -3$ m and adjacent to the beam pipe is the tungsten-scintillator Beam Pipe Calorimeter (BPC). It consists of two modules on either side of the beam pipe and measures the energy of positrons scattered under very small angles, which miss the RCAL. Inbetween RCAL and BPC is the so called Beam Pipe Tracker (BPT), a silicon micro-strip detector, which measures the scattering angle of the positrons hitting the BPC, with respect to the incoming positron beam. The next detector is the veto wall (VW), an 87 cm thick iron wall equipped with two scintillator layers. It is located at $Z = -7.3$ m to shield the detector against the background particles produced in the interactions of the proton beam with the remnant gas. Further down in the backward direction, in the tunnel is the Luminosity Monitor (LUMI), consisting of two lead-scintillator electromagnetic calorimeters. These detectors allow the determination of HERA luminosity and thus they constitute one of the most important components in the ZEUS experiment. Installed at $Z = -44$ m is another calorimeter of this type, the Photoproduction Tagger (PT), which was especially designed to detect scattered positrons from photoproduction events.

In the forward direction, the Proton Remnant Tagger (PRT), a lead-scintillator counter, is installed around the beam pipe at $Z = 5.1$ m. It gives additional information about the hadronic final state produced in the ep scattering. Protons scattered in the forward direction are registered by 6 silicon micro-strip stations of the Leading Proton Spectrometer (LPS), installed between $Z = 20$ m and $Z = 90$ m. There is also the Forward Neutron Calorimeter (FNC), located at $Z = 105$ m which registers neutrons produced under small angles in the proton beam direction.

These and other ZEUS detector components are described in more detail in [36] while here only the components most relevant to the presented analysis are outlined closer.

3.2.1 The Central Tracking Detector (CTD)

The Central Tracking Detector [37] measures the trajectory and momentum of charged particles emerging from the interaction point (IP). It operates in an axial magnetic field of 1.43 T provided by the superconducting solenoid. The CTD is a cylindrical drift chamber 205 cm long, with an inner radius of 18.2 cm, and an outer radius of 79.4 cm. These dimensions correspond to a wide angular coverage in the polar angle ($15° < \theta < 164°$) and a full azimuthal coverage. The chamber is filled with a mixture of Argon, CO_2, and ethane in the following proportion 0.90:0.08:0.02.

The CTD consists of 72 drift layers arranged into 9 superlayers as presented in Figure 3.3. The wires within a superlayer are azimuthally organized into cells, with each cell containing 8 sense wires. The superlayers alternate between those with wires parallel to the beam axis, the so called axial layers (odd numbered), and those with wires inclined at about $\pm 5°$ with respect to the beam direction, to provide a stereo view. The stereo layers together with the measurement of the time difference in the arrival of the pulse to both ends of the sense wires enable the determination of the track Z coordinate, the so called Z-by-Timing-System [38].

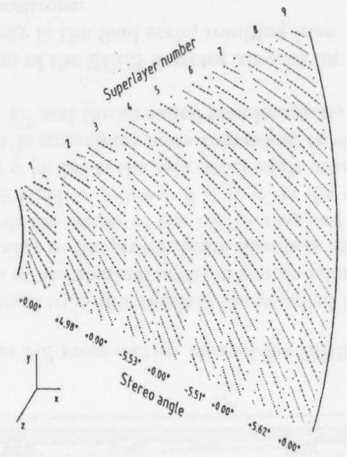

Figure 3.3: The cross section of one octant of the CTD. Sense wires are indicated by larger dots.

The resulting spatial resolution of the CTD is around 180 μm in the XY plane and about 1.0 mm in the Z direction. For tracks going through all the superlayers the transverse-momentum resolution of the CTD is $\sigma(p_T)/p_T = 0.0058p_T \oplus 0.0065 \oplus 0.0014/p_T$. Generally the momentum resolution improves with the growing number of superlayers the particles pass through.

In the presented analysis the information from the CDT is used in the reconstruction of relevant kinematical variables and also in the selection of vector meson photoproduction events.

3.2.2 The Uranium-scintillator Calorimeter (UCAL)

Surrounding the solenoid is the high resolution ^{238}U-scintillator sampling calorimeter (UCAL)[39] covering the angular range $2.6° < \theta < 176.2°$. The depleted uranium[1] serves as the absorber and the plastic scintillator[2] as active material. The thickness of the the plates was tuned to reach equal response from electrons and hadrons (compensation): 3.3 mm thick depleted uranium plates are interleaved with 2.6 mm thick scintillator.

[1] an alloy of 98.4% ^{238}U, 1.4% Nb (which makes the alloy harder) and $\leq$ 0.2% ^{235}U
[2] SCSN-38

The specific choice of the calorimeter construction materials allows to achieve the best possible energy resolution for the registered hadrons. The difficulty in the hadron energy measurement is caused by the fact, that hadrons initiate nuclear reactions often involving neutrons which somehow fail to deposit their whole energy. Therefore a hadron of specific energy produces a shower whose energy is smaller than that of an electromagnetic shower initiated by a positron of the same energy. This energy "lost" in the nuclear reactions has to be compensated for. In the ZEUS calorimeter this compensation is obtained with the use of depleted uranium as the absorbing material, and scintillator layers of precisely matched thickness. In the uranium absorber a fraction of the the hadronic shower energy results in the production of low energy neutrons, which can in turn induce fission in ^{238}U. The fission reaction results in the production of fast neutrons, which can in turn scatter elastically off protons. The energy of the recoil protons is registered and accounts for the energy invisible in the nuclear reactions of the initial hadron. The hadron response is by this effect enhanced considerably, what designates uranium calorimeters as the best choice for hadronic energy measurements. With the ZEUS UCAL it is possible to achieve identical energy responses to positrons and hadrons of the same energy ($e/h = 1$).

The whole UCAL consists of three parts : a forward component (FCAL, $2.6° < \theta < 36.7°$) located in the direction of the outgoing proton at $Z = 2.22$ m, a barrel part (BCAL, $36.7° < \theta < 129.1°$) extending from 120 to 230 cm in radius and a rear section (RCAL, $129.1° < \theta < 176.2°$) opposite to FCAL. Each of these sections is segmented longitudinally in an electromagnetic and one (RCAL) or two (FCAL, BCAL) hadronic sections, called the EMC and HAC respectively, as presented in Figure 3.4. The calorimeter modules are divided into cells, the size of which depends on the type (EMC, HAC) and position of the module, as shown in Table 3.2.

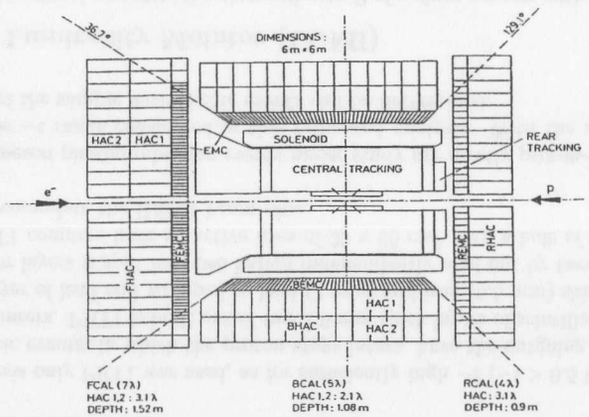

Figure 3.4: Schematic view of the ZEUS uranium calorimeter sections (BCAL, FCAL, RCAL) and their division into EMC and HAC cells.

The BCAL consists of 32 wedge shaped modules, each covering an angle of 11.25° in azimuth and 332 cm long. The inner 21 uranium/scintillator layers form the electromagnetic calorimeter (BEMC) 22 X_0 deep. The outer 98 layers are divided into equally sized sections and make up the hadronic calorimeter – BHAC1 and BHAC2, each with a depth of 2.0 λ.

UCAL Section	Angular Coverage	Cell Size	EMC	HAC
FCAL	$2.6° < \theta < 39.9°$	$x \times y$	20×5 cm^2	20×20 cm^2
RCAL	$128.1° < \theta < 176.2°$	$x \times y$	20×10 cm^2	20×20 cm^2
BCAL	$36.7° < \theta < 129.1°$	$z \times \varphi$	5.06 cm×11.25°	20.3 cm×11.25°

Table 3.2: Angular coverage of UCAL sections and the dimensions of calorimeter cells

The FCAL and RCAl both consist of 23 rectangular modules 20 cm wide, and 220 to 460 cm high (with two half modules above and below the beam pipe, leaving a hole of 20×20 cm^2). The first 25 uranium/scintillator layers (26 X_0) form the electromagnetic section (FEMC and REMC). The rest forms the hadronic calorimeter, of which the FCAL part is segmented into two longitudinal parts. Every HAC section (FHAC1, FHAC2, RHAC) consists of 80 uranium/scintillator layers, thus has the depth of 3.1 λ.

The energy resolution of the calorimeter, as measured under test beam conditions is $\sigma_e/E \approx 18\%/\sqrt{E}$ for electrons and $\sigma_h/E \approx 35\%/\sqrt{E}$ for hadrons, with the energy E in GeV.

The light produced in the stintillator is read out from both sides of the calorimeter modules via 2 mm thick wavelength shifters (WLS) coupled to photomultiplier tubes (PMT). The PMTs convert the light into an electrical signal, which is processed by the readout electronics into energy.

Besides its compensating properties, the uranium serves as a valuable tool for the calibration and monitoring of the UCAL through its natural radioactivity. The precision of the calibration of the calorimeter cells is at the level of 1%. This is achieved by setting the photomultipliers's gains in a way that equalizes the uranium signal from different cells. Therefore, despite the uranium radioactivity, the calorimeter has very low noise, which is typically 10 MeV in the EMC cells and 20 MeV in the HAC cells.

The calorimeter information plays an important role in the selection of events for the presented analysis. Events with energy deposits not associated to the decay tracks of the mesons are discarded from the final sample.

3.2.3 The Photoproduction Tagger (PT)

The photoproduction tagger (PT) is a small electromagnetic sampling calorimeter located at Z=-44 m and sensitive to 21-26 GeV positrons scattered under very small angles (below a few mrad). It is built of twelve tungsten plates ($70 \times 90 \times 7$ mm^3) interleaved with 3 mm thick scintillator layers. After the first three tungsten plates an additional layer of 8 mm wide, vertical scintillator strips is installed. The strips are read out by plastic light guides and PMTs. Fiducial cuts can be applied to signals from this strip layer to select events with electromagnetic showers well contained within the tagger.

The test beam measurements demonstrated that for 1-5 GeV electrons hitting the calorimeter centrally the energy resolution is $\sigma/E \approx 0.25/\sqrt{E(GeV)}$ and the calorimeter linearity is better than 1%.

In this analysis the PT serves as a tagger for photoproduction events. In all the analyzed

events the scattered positron is registered in the PT, which ensures that the photon virtuality Q^2 is small and thus enables a precise t measurement (see Sec. 4.1.2).

3.2.4 The Proton Remnant Tagger (PRT)

The PRT [40] consists of 7 pairs of scintillator counters surrounding the beam pipe, which detect particles associated with the remnant of the dissociated proton. Two pairs of counters (PRT1) are located at $Z = 5$ m and five pairs (PRT2) are installed at $Z = 24$ m in the forward direction in the ZEUS frame, which tag particles in the angular range from 6 to 26 mrad and from 1.5 to 8 mrad, respectively.

In this analysis only PRT1 was used, as for sufficiently high $-t$ ($-t > 0.5$ GeV^2) a fraction of the true elastic events, in which the proton stays intact, have the outgoing proton detected in the PRT2 counters. PRT1 is built out of two 2.6 mm thick layers of scintillator separated by a 1 mm thick layer of lead and wrapped in lead (2 mm) and iron (0.5 mm) shielding foil. Each of the scintillator layers is split into two halves independently read out by two photomultiplier tubes. The PRT1 counters have an active area of 30×26 cm^2 with a hole of 6.0×4.5 cm^2 at the center to accomodate the HERA beam pipe.

The vector meson photoproduction events under study are mostly proton-dissociative, due to the very wide $-t$ range considered in thie presented analysis. With the use of PRT1 the contamination of the sample with elastic events can be determined.

3.2.5 The Luminosity Mointor (LUMI)

The collider luminosity L connects the observed rate R of a given process with the cross section σ of this process and is defined as

$$R = L\sigma \tag{3.1}$$

The value of luminosity depends on the accelerator and beam parameters. It can be either calculated from these parameters or determined from Eq. 3.1 using a well known process.

In the ZEUS experiment the Bethe-Heitler small angle bremsstrahlung process $ep \to ep\gamma$ is used to measure the luminosity, since the cross section for this process is large and is known very precisely from QED calculations [41]. The main advantage of this process is its clean experimental signature, namely the photon and the scattered positron registered in coincidence under small angles with respect to the initial positron beam direction. The recoil proton can be neglected to a very good approximation and therefore the sum of the energies of the photon (E_γ) and the scattered positron ($E_{e'}$) sum up to the energy of the positron beam (E_e) . The photon and the scattered positron emerge from the IP at very small angles θ_γ and $\theta_{e'}$, with respect to the incident positron direction. The values of θ_γ and $\theta_{e'}$ are typically of the order of M_e/E_e and $M_e/E_{e'}$ respectively.

The so called Luminosity Monitor (LUMI) is a detector especially dedicated to measuring luminosity from bremsstrahlung events. Because of small emission angles of the photons and positrons it is possible to register them with seemly small detectors located close to the beam pipe. The LUMI [42] consists of two lead-scintillator sampling calorimeters used to register the scattered positrons (LUMI$_e$) and the bremsstrahlung photons (LUMI$_\gamma$) and located in the HERA tunnel at $Z = -35$ m and $Z = -107$ m respectively. The LUMI$_e$ measures scattered positrons at angles $\theta_{e'} < 6$ mrad with an efficiency greater than 70% for

$0.35E_e < E_{e'} < 0.65E_e$ GeV. The LUMI$_\gamma$ has a geometrical acceptance of 98% independent of the photon energy for bremsstrahlung events. Both these detectors have an energy resolution of $\sigma/E \approx 0.18/\sqrt{E(\text{GeV})}$. Each calorimeter is equipped with a position detector built of two layers of horizontal and vertical scintillator fingers, which is inserted after $3X_0$ in LUMI$_\gamma$ and after $7X_0$ in LUMI$_e$. To shield the photon calorimeter from synchrotron radiation a $3.5X_0$ carbon/lead filter is placed in front of it. The presence of this filter deteriorates the resolution of the calorimeter to $\sigma/E \approx 0.24/\sqrt{E(GeV)}$ and introduces a nonlinearity in the detector response. The layout of the Luminosity Monitor together with the Photoproduction Tagger is presented in Fig. 3.5.

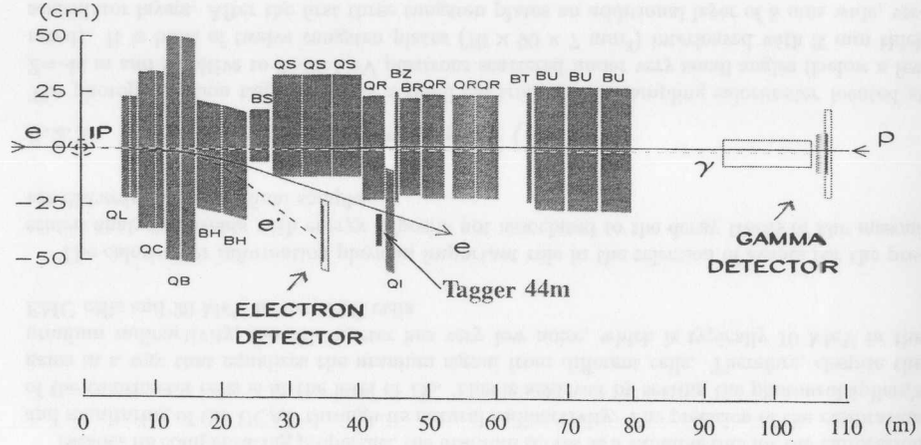

Figure 3.5: The general layout of the ZEUS Luminosity Monitor.

The luminosity is determined from the rate of the high energy bremsstrahlung photons registered in LUMI$_\gamma$ within an energy window. The measurement of the scattered positrons in LUMI$_e$ is used for systematic checks. The total bremsstrahlung rate observed is however contaminated with e-gas bremsstrahlung events , $eZ \to e\gamma Z$, originating from the interactions of the positron beam with residual gas in the beam pipe. These events have practically the same signature as ep bremsstrahlung. The e-gas contribution to the total rate is estimated statistically using the electron pilot bunches (see Sec.3.1). The corrected ep bremsstrahlung rate R_{ep} is evaluated as follows:

$$R_{ep} = R_{tot} - R_{pilot} \cdot \frac{I_e^{tot}}{I_e^{pilot}} \ , \tag{3.2}$$

where R_{tot} is the total rate within an energy window, R_{pilot} is the rate measured for unpaired pilot bunches, I_e^{tot} is the total positron current and I_e^{pilot} is the current of the positron pilot bunches. The e-gas bremsstrahlung is not the only source of background in the luminosity measurement. The observed rate of registered ep-bremsstrahlung photons is further corrected for multiple bremsstrahlung events in the same bunch crossing, the geometrical acceptance of the photon detector, the nonlinearity of the energy scale and the limited energy resolution. The

luminosity is therefore calculated with the corrected rate R_{ep}^{corr} as:

$$L = \frac{R_{ep}^{corr}}{\sigma_{BH}}. \tag{3.3}$$

The Luminosity Monitor is a very important component. The measurement of luminosity with the LUMI detectors allows the determination of cross sections for different processes. In this analysis LUMI was additionally used to calculate the acceptance of the Photoproduction Tagger (see Sec. 5.3.2).

Chapter 4

Reconstruction and event selection

In this analysis only the production of vector mesons, which decay into two charged particles is taken into account. This choice is dictated by the experimental conditions in which the possibility of particle identification is limited, as is the momentum measurement for neutral particles. The number of analyzed vector mesons is thus limited to three: $\rho^0 \to \pi^+\pi^-$ (BR=100%) , $\phi \to K^+K^-$ (BR=50%) and $J/\psi \to e^+e^-/\mu^+\mu^-$ (BR=12%). The other decay channels of these mesons often include neutral pions in the final state, which would be detected only in the UCAL, and not in the CTD. This would significantly complicate the momentum measurement and the reconstruction of the variables relevant in the analysis. For the same reasons the analysis does not include the $\omega \to \pi^+\pi^-\pi^0$ meson.

4.1 Off-line event reconstruction

In Fig.4.1 the diffractive vector meson production signature is shown schematically. The presence of two and only two tracks of opposite charge in the CTD is required. The only energy

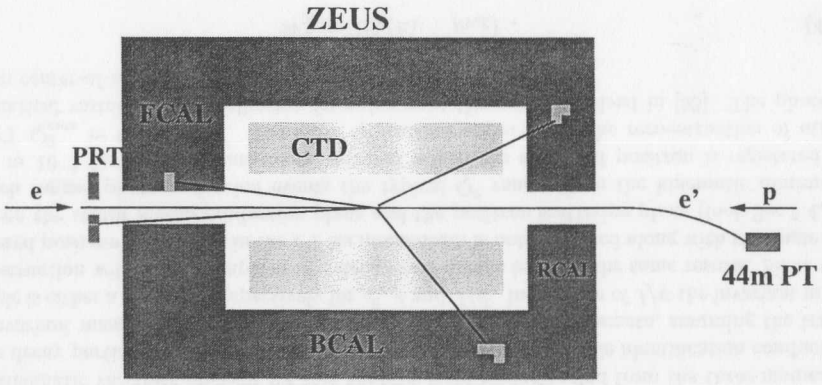

Figure 4.1: A sketch of the diffractive vector meson production signature in the ZEUS detector

deposits in the RCAL and BCAL are to be those coming from the registered tracks. This requirement reduces strongly the photon-dissociative background. Additional energy can be deposited in the FCAL by the constituents of the proton fragmentation system. The scattered

positron is registered in the Photoproduction Tagger, which ensures that the virtuality of the exchanged photon is below 0.02 GeV^2 and thus enables a precise t measurement.

4.1.1 Reconstruction of particles in detectors

Reconstruction of charged particles in the CTD

To reconstruct the particle tracks and the primary vertex in the CTD the VCTRAK [43] package was used. The default version performs track finding twice per event. In the first stage of the reconstruction only the information from the CTD are used, while in the second also additional information from other tracking detectors like SRTD and RTD. In this analysis only the first stage of the reconstruction is used, as this reduces the uncertainties in the corrections for efficiency and acceptance.

Each track candidate begins as a track "seed" in an outer part of the CTD. A track seed is then extrapolated inward, gathering additional hits with increasing precision as the track parameters are updated. When all the tracks are successfully reconstructed the primary interaction vertex is determined. Only tracks which emerge from the beam line are used for vertex reconstruction. To help constrain the vertex position a diffuse pseudo-proton centered at the beam spot in the XY plane (with $\sigma_X = \sigma_Y = 0.7$ cm) is added. The final vertex fit not only determines the final vertex position, but also constrains the remaining tracks (vertexed tracks) to it simultaneously re-fitting the direction and curvature of these tracks.

In this analysis the vertexed tracks, assumed to be the decay tracks of the vector meson, are used to perform the reconstruction of the event's kinematics.

Detection of particles in the UCAL

The reconstruction of the particles' energies deposited in the calorimeter is based on the readout of the two photomultipliers connected to each cell. The positions and energy deposits of the calorimeter cells provide sufficient information to perform the selection and reconstruction of each event. In this analysis the clusters of energy deposits in the calorimeter were matched to the tracks found in the CTD [44]. Any calorimeter cell, which is not associated to the decay tracks observed in the CTD, with energy well above noise is good evidence for additional particles being present in an event.

Detection of the scattered positron in the PT

Positrons of energy between 21 and 26 GeV, scattered under very small angles are detected in the PT. A hit in the PT, required in the trigger, is defined as an energy deposit greater than 1 GeV. The off-line reconstruction of the scattered positron's energy is possible by applying a fiducial cut which selects electromagnetic showers well contained in the detector. This however reduces the number of the observed vector meson candidates by 30-50% and increases the systematic error on the tagging efficiency of the PT. On the other hand the energy of the scattered positrons can be calculated with much higher accuracy from the vector meson momentum measured in the CTD. Therefore in this analysis only the hit information from the PT was useful and no off-line reconstruction of the positron's energy was performed.

Detection of particles in the PRT

A particle is observed in the PRT if it hits one of the PRT counter pairs. The hit in a given pair is defined as the coincidence of signals above noise in both counters. Signals not related to particles coming from the IP were suppressed by a timing cut.

4.1.2 Reconstruction of kinematic variables

The kinematic variables relevant for this analysis were reconstructed from the three-momenta of the decay particles measured in the CTD. Since there is no particle identification conducted the invariant mass of the meson is reconstructed from the track momenta, assuming the track particle is either a π, K or e respectively for ρ^0, ϕ and J/ψ. In the case of J/ψ the invariant mass reconstruction with the assumption of a decay into muons leads to the same results. Since the scattered positron is detected in the PT its momentum is not measured along with the angle Φ_h between the vector meson production plane and the positron scattering plane (look Sec.2.4.4). In such tagged photoproduction events the typical Q^2 ranges from the kinematic minimum $Q^2_{min} \approx 10^{-9}$ GeV^2 to the maximum value at which the scattered positron is registered in the PT $Q^2_{max} \approx 0.015$ GeV^2. Therefore Q^2 can be neglected in the reconstruction of other kinematical variables. The following formulae were thoroughly derived in [53]. The photon-proton center-of-mass energy can be approximated by

$$W^2_{\gamma p} \approx 2E_p(E_V - p_{V,Z}) \ , \tag{4.1}$$

where E_p,E_V and $p_{V,Z}$ denote the energy of the incoming proton, the energy of the produced vector meson and the vector meson longitudinal momentum, respectively, all measured in the laboratory frame. The vector meson transverse momentum reconstructed from the track momenta is given by

$$p^2_{V,T} = (p_{x+} + p_{x-})^2 + (p_{y+} + p_{y-})^2 \tag{4.2}$$

where $p_{x,\pm}$ and $p_{y,\pm}$ are the x and y momentum coordinates of the decay particles. The four momentum transfer in the proton vertex t and its maximum value t_0 are given by

$$t \approx t_0 - p^2_{V,T} \approx -M^2_V(M^2_N - M^2_p)/4W^2 - p^2_{V,T} \tag{4.3}$$

for events which fulfill the condition $Q^2 \ll -t, p^2_{V,T}, M^2_V, M^2_N \ll W^2$. Since $-t_0$ is small compared to the $-t$ value in the whole kinematical range covered in this analysis, it can be neglected and then

$$t \approx -p^2_{V,T}. \tag{4.4}$$

The approximation $Q^2 = 0$ is also used in the reconstruction of the decay angles in the helicity frame.

4.2 Trigger

Most of the signals registered in the ZEUS detector are background events from cosmic rays or beam-gas interactions, which have a much higher rate than the positron-proton collisions. To effectively select interesting physics events a three level trigger system is used. The first level trigger (FLT) is a hardware trigger, which issues a decision based on the global properties of each event. These are determined from the raw signal information read from different detector components. The second level trigger (SLT) and the third level trigger (TLT) are both software based triggers. The SLT serves mainly to identify and eliminate background events

while the TLT enables advanced selection of physics events based on part of the ZEUS off-line reconstruction code. The final output rate of the TLT is the order of a few Hz.

4.2.1 Trigger for vector meson events

For the purpose of this analysis at the first level trigger a coincidence between signals from the PT and a good track candidate in the CTD was required. An upper limit of 1 GeV was imposed on the energy deposits in the LUMI photon and electron calorimeters was imposed to suppress random overlays with bremsstrahlung events. The second level trigger imposed restrictions on the number of tracks and track segments in the CTD and included a requirement on the vertex position if the vertex had been found. Also applied at this stage was a requirement on the transverse momentum of any track p_T to be greater than 0.8 GeV. Events selected by the third trigger level had exactly two tracks pointing to the same vertex, which was located within bounds of the nominal position of the IP, namely $|V_Z| < 60$ cm. Due to these trigger conditions the $-t$ range is in this analysis is restricted to above $-t > 1.1$ GeV^2.

4.3 Selection of vector meson candidates

In order to select the vector meson candidates, events with the following characteristics were accepted to the final sample

- General selection

  1. The PT was modified and placed in a new position in the middle of 1996. Only the data collected with the tagger in its new position are the topic of this analysis. Runs with any problem with the PT or any other important component were excluded from the analysis.

- Tracking requirements

  2. Two tracks of opposite charge emerging from a common vertex were required.
  3. The vertex position was required to be in the range: $\sqrt{V_x^2 + V_y^2} < 0.7cm$ and $|V_z| < 40cm$
  4. The cuts on the pseudorapidity of each track: $|\eta| < 2.1$
  5. The cut on the minimum transverse momentum of each track were the following: $p_T > 150MeV$ (for ρ^0), $p_T > 400MeV$ (for ϕ), $p_T > 500MeV$ (for J/ψ).

- Diffractive event selection

  6. This is a cut on the maximum energy E_{max} of a calorimeter cell not associated with the two tracks. All the cells inside a cone of the opening angle α at the vertex are assigned to the track. It is required that E_{max} is below the energy equivalent to the maximal noise in the calorimeter, thus in the RCAL and BCAL $E_{max} < 250MeV$. The cone opening angle around the track was chosen $\alpha = 0.2rad$.

- The kinematical cuts.

  7. The $W_{\gamma p}$ range chosen for this analysis is restricted to the region where the PT acceptance is well understood, namely $80 < W_{\gamma p} < 120$ GeV

  8. The $-t$ range in the analysis is limited by the trigger conditions to values above 1.1 GeV^2 and extends up to 12 GeV^2 for ρ^0, 7 GeV^2 for ϕ and 6.5 GeV^2 for J/ψ.
  9. Finally the vector meson candidates are identified by applying cuts on the invariant mass of the track pairs. The invariant mass of the vector mesons was reconstructed from the momenta of the two tracks registered in the CTD with the assumption that the decay particles observed are pions ($M_{\pi\pi}$), kaons (M_{KK}) or electrons (M_{ee}). The invariant mass cuts in the resonance region are as follows:

$$\begin{aligned} 0.55 < M_{\pi\pi} < 1.1 \text{ GeV} \quad \text{and} \quad M_{KK} > 1.075 \text{ GeV} \quad & \text{for } \rho^0 \\ 0.99 < M_{KK} < 1.06 \text{ GeV} \quad & \text{for } \phi \\ 2.98 < M_{ll} < 3.13 \text{ GeV} \quad & \text{for } J/\psi. \end{aligned}$$

The cuts on $M_{\pi\pi}$ were tuned to suppress the contamination of the ρ^0 sample with other vector mesons ($\omega \to \pi^+\pi^-\pi^0$ $\rho'(1500) \to \pi^+\pi^-$ and $\phi \to KK$). To reduce the non-resonant background the cuts on M_{KK} and M_{ll} were chosen at the level of ± 3 typical mass resolutions around the reconstructed ϕ and J/ψ masses, respectively. In Fig.4.2 all three invariant mass distributions are presented and in Tables 4.1 a, b and c the number of events after each of the above selection steps is listed for each meson separately.

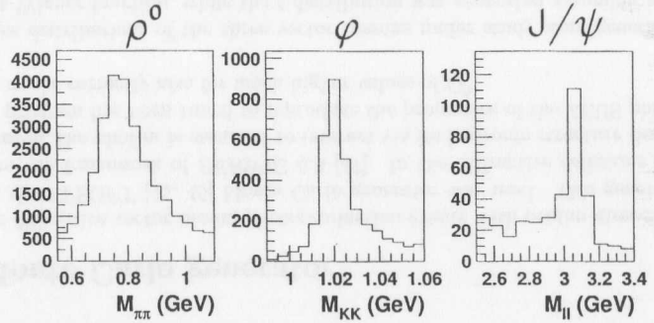

Figure 4.2: The invariant mass distributions for all three vector mesons studied in this analysis

selection cut	number of events (a)
2	176702
3	164768
4	143172
5	137934
6	73320
7	55654
8	37065
9	25447ρ^0

selection cut	number of events (b)
2	176702
3	164768
4	143172
5	86963
6	86963
7	38365
8	28166
9	3095ϕ

selection cut	number of events (c)
2	176702
3	164768
4	143172
5	59740
6	33466
7	25872
8	19513
9	166J/ψ

Table 4.1: The impact of the selection cuts on the number of events in the data for ρ^0 (a), ϕ (b) and J/ψ (c) mesons. The final number of events considered in the analysis is that remaining after cut number 9.

In the final sample after all selection cuts there are 25447 ρ^0 mesons, 3095 ϕ mesons and only 166 J/ψ mesons. For the purpose of the decay angular analyses the ρ^0, ϕ and J/ψ signals were extracted by fitting the invariant mass with a function being a sum of a function for the signal and for the background. In case of ϕ and J/ψ these fits were performed in a wider range of invariant mass. The invariant mass fit regions are the following for ϕ and J/ψ respectively:

$$0.9875 < M_{KK} < 1.15 \text{ GeV} \quad \text{for } \phi$$
$$2.3 < M_{ll} < 3.4 \text{ GeV} \quad \text{for } J/\psi.$$

Extending the fit range in invariant mass enabled a better background parameterization.

Chapter 5

Monte Carlo simulation

This chapter contains the description of the Monte Carlo (MC) programs used to study and account for the event selection efficiency of the vector meson candidates. In the ZEUS experiment the event simulation proceeds in two stages. In the first step the *ep* scattering is simulated with a given MC event generator describing the cross section dependence on the event kinematics and the production of the hadronic final state (Section 5.1). The detector response to these generated final states and the trigger are simulated in the next stage (Section 5.2).

5.1 Monte Carlo generator

To simulate diffractive vector meson photoproduction events with proton-dissociation, namely $\gamma p \to VN$, the EPSOFT [45, 46] Monte Carlo generator was used. This generator has been developed in the framework of HERWIG 5.8 [47]. In the diffractive collisions of the photon with the proton, the photon is assumed to interact via its hadronic structure described by the VDM. The program has been tuned to reproduce the properties of the ZEUS photoproduction events, but works correctly also for much higher values of Q^2.

The mass distributions of the three vector mesons under study were generated according to the Breit-Wigner function, while the t distribution was generated assuming an exponential dependence. The distributions of the vector meson decay angles were generated according to SCHC.

5.1.1 M_N evolution with t

In EPSOFT the mass spectrum of the proton-dissociative nucleonic system, N, was simulated as

$$\frac{d\sigma(\gamma p \to VN)}{dM_N^2} \propto \left(\frac{1}{M_N^2}\right)^{\beta}, \tag{5.1}$$

where $\beta = 1.0$, thus assuming no M_N evolution with t. The results of proton-dissociative experiments [51, 52], as well as the measurements in this analysis show that at large $-t$ this assumption is not sufficient. From the fits of Equation 5.1 to the IRS data [51] at different values of t in the range $0.15 < -t < 2.95$, β was found to depend on t [53].

To test the t-dependence of β in the present analysis the energy deposit E_{FCAL} of the proton fragments in the FCAL was studied in several t ranges. It is correlated with the mass distribution of the proton dissociative system and therefore also with the generated $d\sigma/dM_N^2$.

In Figure 5.1 a comparison between E_{FCAL} distributions in data and the EPSOFT MC (with $\beta = 1.0$) in different t bins are presented for the ρ^0, ϕ and J/psi mesons. The mean values quoted on the plots correspond to the E_{FCAL} distributions in data. The rise of the mean value of the FCAL energy deposits with t manifests a clear evolution with t of the E_{FCAL} distributions, as well as M_N. The MC does not reproduce the data distributions, with growing discrepancies at higher values of t.

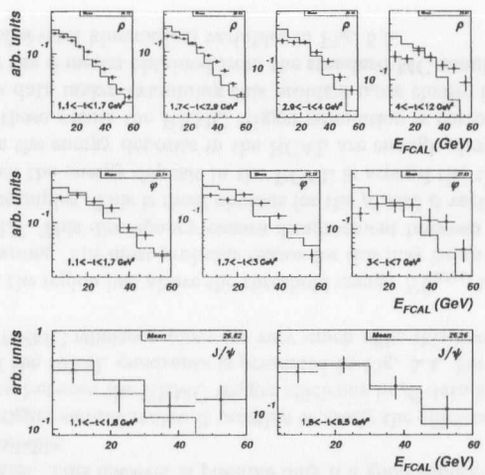

Figure 5.1: Comparison of the normalized E_{FCAL} distributions in data (points) and the EPSOFT MC (histograms) for the ρ^0, ϕ and J/ψ mesons in different $-t$ bins. Quoted mean values correspond to the data.

To achieve agreement between data and MC a parameterization of β as a function of t had to be determined, and applied as a weight to the MC sample. The parameterization $\beta = \beta(t)$ was obtained using the minimal χ^2 method in each t bin to compare the E_{FCAL} distributions in data with the same distributions in the MC reweighted with Equation 5.1. The procedure is described in more detail in [8]. It was found that for ρ^0 and ϕ mesons β decreases exponentially with increasing $-t$, while for J/ψ it is constant in the whole t range under study. The final weights applied to the MC sample were calculated according to equation 5.1 with the use of the following expressions for β:

$$\beta = e^{0.186(\pm 0.040) - 0.297(\pm 0.023)\cdot t} \text{ for } \rho^0, \tag{5.2}$$

$$\beta = e^{0.461(\pm 0.100) - 0.505(\pm 0.057)\cdot t} \text{ for } \phi, \tag{5.3}$$

$$\beta = 0.63(\pm 0.27) \text{ for J}/\psi. \tag{5.4}$$

The reweighted E_{FCAL} MC distributions are in good agreement with the data for all three vector mesons. This is presented in Fig. 5.2 in which the quoted mean values corresponding to the MC agree with those in the data.

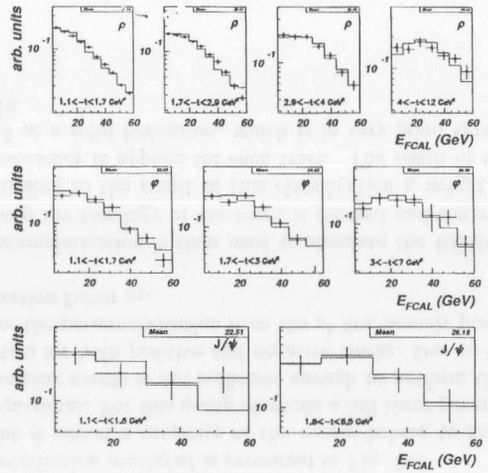

Figure 5.2: Comparison of the normalized E_{FCAL} distributions in data (points) and the reweighted EPSOFT MC (histograms) for the ρ^0, ϕ and J/ψ mesons in different $-t$ bins. Quoted mean values correspond to the MC.

5.2 ZEUS Monte Carlo simulation

The generated events are then passed through the simulation of the ZEUS detector and trigger. The ZEUS detector simulation uses the GEANT [48] package, while the MOZART [49] package was used to lead the particles through the whole detector, taking into account the physics processes they undergo. For the simulation of the ZEUS trigger decision, which is based on the signals from different detector components, the software package ZGANA [50] was used. The reconstructed MC events are then treated with the same analysis tools as the data.

5.3 Trigger efficiency

A good simulation of the trigger in the MC is crucial for obtaining correct physical results. Any improperly simulated trigger efficiency may lead to wrong conclusions from the analysis. It is fairly easy to verify the TLT and SLT efficiencies using for example the so called *control trigger events*, i.e. a fraction of all events, which is taken with looser cuts than the nominal trigger cuts. However this is difficult for the hardware based FLT. In this section the modeling of trigger efficiencies at the FLT, which were incorrectly simulated in the EPSOFT MC is presented.

5.3.1 The REMC trigger efficiency

In ZEUS there are two trigger configurations – the so called High-Lumi and Low-Lumi triggers. At the beginning of each run, when the luminosity is high, and so are the observed event rates the High-Lumi trigger is required in order to suppress background from accidental coincidences. This High-Lumi trigger configuration includes the requirement that the energy deposit in any of the four quadrants (see Fig. 5.3) of the electromagnetic section or the rear calorimeter (RCAL)

is greater than 464 MeV. When during data taking the luminosity goes below a certain level the trigger configuration is switched to Low-Lumi which does not include this condition.

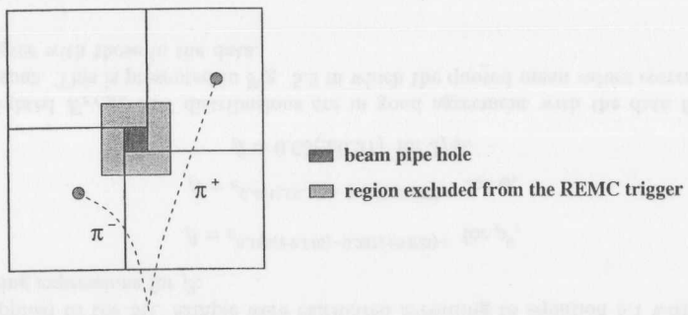

Figure 5.3: A sketch of the four trigger regions in RCAL. On it a schematic drawing of two tracks from the ρ^0 decay hitting these regions.

In 1996 all data collected with the high $-t$ vector meson trigger were taken in the High-Lumi configuration, which accounts for $3.3pb^{-1}$. In 1997 $13.2pb^{-1}$ of data was taken using the High-Lumi configuration and $7.6pb^{-1}$ in the Low-Lumi configuration for the high $-t$ vector meson trigger. Altogether the luminosity acquired for the purpose of this analysis in both these trigger modes is $16.5pb^{-1}$ and $7.6pb^{-1}$ for High-Lumi and Low-lumi respectively. It is essential to combine these two trigger samples to increase the analyzed data set and thus reduce the statistical uncertainties. This however is possible only if a good Monte Carlo simulation of the REMC trigger is available.

The Low-Lumi trigger sample makes it possible to study the efficiency of this trigger condition. The comparison between the REMC trigger efficiency in ρ^0 data and MC as a function of the energy in one of the RCAL quadrants is presented in Fig. 5.4. For the other three RCAL trigger sections the REMC efficiency plots are very much alike this one.

It is clear that in the region just above the threshold energy E^{th}_{REMC} the trigger simulation in the Monte Carlo is wrong. The most probable reason for this may be an incorrect RCAL energy simulation in the FLT. This discrepancy causes disagreement between data and MC for both analyzed trigger subsamples. This is most obvious for the ρ^0 and ϕ vector meson photoproduction events, for which the energy deposit in the RCAL is around the threshold. On the other hand for J/ψ events the energy deposits in the RCAL are enough above the threshold energy to assume that for those events the REMC trigger simulation is correct. Unfortunately poor J/ψ statistics in the data makes examining this problem more closely impossible. The REMC trigger efficiency for the ϕ meson obtained from the standard MC simulation is compared with data as a function of several kinematical variables in Fig. 5.5.

A separate REMC trigger simulation, based on the Low-Lumi data sample was performed by applying a method described in [57]. In this method the trigger efficiency is studied and parametrized as a function of the track momenta. The Low-Lumi data sample was divided into two groups of events depending on the event topology. The first group included events in which both tracks hit the same RCAL quadrant. The second group included these events, in which at least one track hit the RCAL, and if both did they hit two different quadrants. Events in

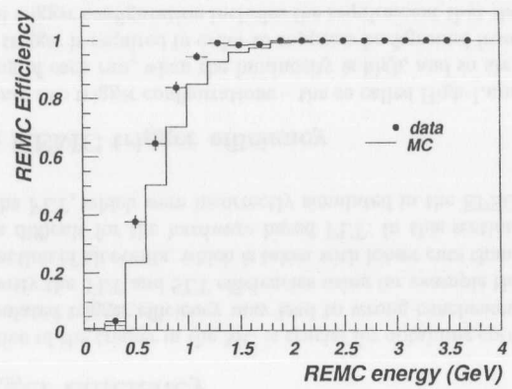

Figure 5.4: The comparison between ρ^0 data and MC of the REMC trigger efficiency as a function of the energy deposit in one of the electromagnetic RCAL trigger sections.

which neither track hit the RCAL were excluded from the analysis, which is less than 1% of the sample. For the first group of events the REMC efficiency was parametrized as a function of the sum of the track momenta. For events in the second group the efficiency parameterization was performed separately for positive and negative tracks as a function of their momentum. A function suggested in [57] :

$$E(P) = a_1 \cdot \left(1 - e^{(P-a_2)\cdot a_3}\right) \tag{5.5}$$

was fitted to the data in both topological groups. The sum of the track momenta or the positive or negative track momentum is denoted by P, while a_1, a_2, and a_3 are fit parameters. The fit was performed for the ρ^0 and ϕ mesons separately, while for J/ψ the standard REMC trigger simulation was found sufficient. The REMC efficiency as a function of the track momenta with the resulting parameterization overlayed is presented in Fig. 5.6.

In the case of the ϕ meson a majority of the events belong to the group in which both tracks hit the same quadrant. For this group of events a full three-parameter fit was done. The statistics of the remaining events is not sufficient enough to perform the two independent fits on all three parameters for both positive and negative tracks. Due to this fact it was decided to retain the shape of the parameterization from the ρ^0 fits, namely parameters a_2 and a_3, and fit only the normalization factor a_1.

The obtained parameterization is then used to simulate the REMC trigger in the Monte Carlo. In the first step the topology of the event is checked and the event is classified to one of the groups. According to the result of this classification a weight, which corresponds to the proper REMC efficiency is applied for each track. The result of this reweighting can be observed in Fig. 5.5 as a solid histogram, which is in very good agreement with the points representing the data.

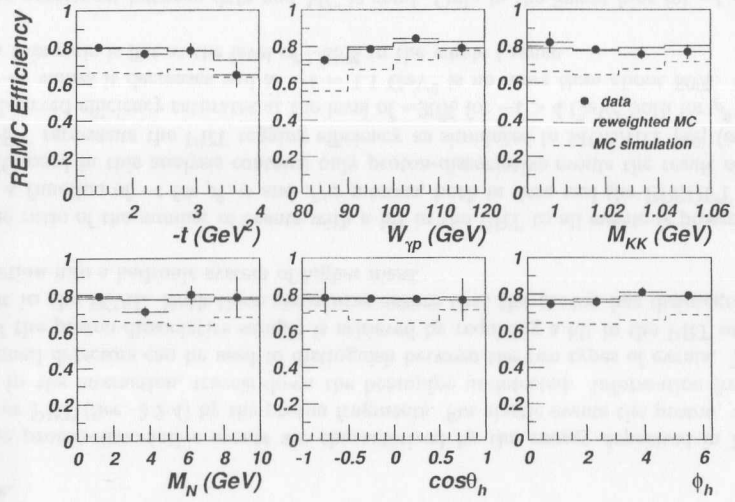

Figure 5.5: The REMC trigger efficiency for ϕ as a function of different kinematical variables. The points are the data, the dashed histogram the standard MC simulation, and the solid histogram represents the MC reweighted with the REMC trigger simulation applied in this analysis.

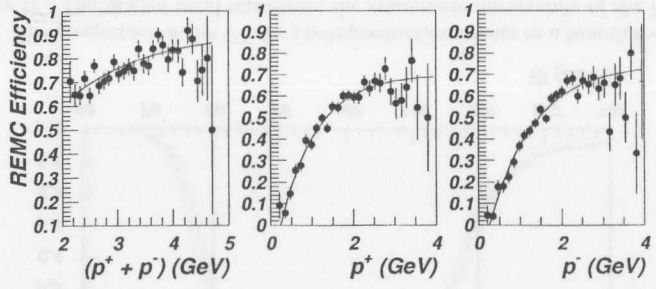

Figure 5.6: REMC efficiency for ρ^0 as a function of the sum of track momenta (left plot), the momentum of the positive track (center plot) and the momentum of the negative track (right plot). The solid lines represent the fit with equation (5.5).

5.3.2 The Photoproduction Tagger Acceptance

The PT triggers events in which the energy deposited by the scattered positron is greater than 1 GeV. Due to such a low threshold energy the tagging efficiency of the PT depends mainly on its geometrical acceptance.

The PT acceptance was determined in [8] by studying the bremsstrahlung events, $ep \to e'\gamma p$ as shown schematically in Figure 5.7. Among events for which the photon was measured in the LUMI photon detector were those which had the scattered positron registered in the PT. The tagger acceptance is defined as the ratio of the number of events with the scattered positron and photon registered in coincidence in the PT and LUMI_γ respectively, to all events with the photon measured in LUMI_γ.

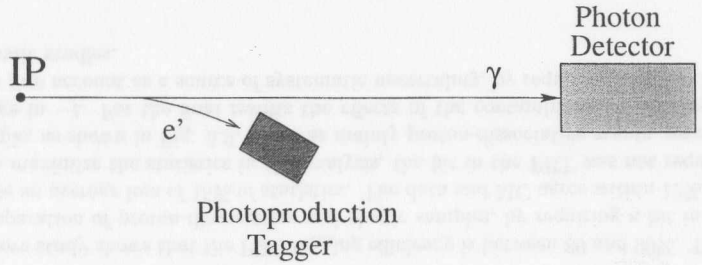

Figure 5.7: A schematic view of the small angle positron and photon tagging system.

The PT itself does not measure the energy of the scattered positron, therefore the acceptance was determined as a function of the photon energy. The energy of the scattered positron which hits the PT can however be calculated as the difference between the nominal positron beam energy and the measured energy of the photon. MC studies in [8] prove that the tagging efficiency is mainly influenced by the tagger position and geometry, the spatial resolution of the positron beam σ_b and the V_x coordinate of the interaction vertex position.

Acceptance of the PT for Photoproduction

The PT acceptance in [8] was determined for photoproduction events with $Q^2 < 0.015$ GeV^2, passed through the simulation of the HERA beam line from the IP to the 44th meter, at which the tagger is located.

Figure 5.8 presents the calculated photoproduction acceptance A of the PT as a function of the γp center-of-mass energy W. The average acceptance in the region $80 < W < 120$ GeV^2 is equal to 80%±4%. The systematic uncertainties in the evaluation of A are mainly due to the LUMI_γ calibration, the position and geometry of the tagger, the eror on the spatial resolution of the beam and the error on the vertex V_x position measurement.

To account for the PT acceptance in the presented analysis, the reconstructed MC events were weighted with the obtained function $A(W)$. The uncertainty in the acceptance calculation was taken into account in the systematic studies of the final results presented in this thesis.

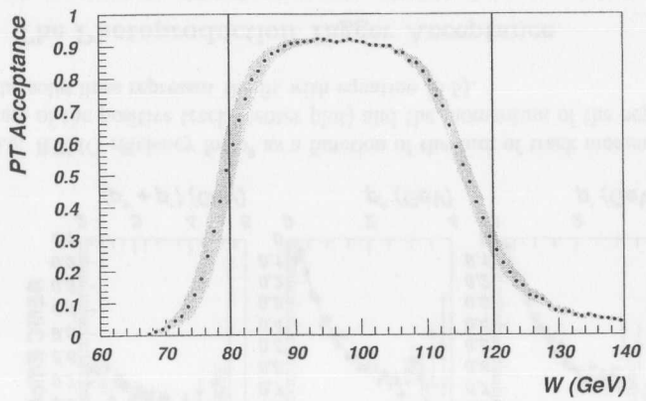

Figure 5.8: The acceptance of the PT for photoproduction events as a function of γp center-of-mass energy W. The shaded band represents the systematic uncertainty of the PT acceptance. Indicated on the plot is the W range used in the analysis

5.4 Separation of elastic and proton-dissociative events

The previous measurements at large $-t$ [7] had shown that the contribution from elastic events falls exponentially with t. For $-t > 1$ GeV^2 the elastic cross section was estimated to be less than 10% of the proton dissociative cross section. Since in this analysis the considered $-t$ range begins at 1.1 GeV^2, mostly proton-dissociative events should be expected in the analyzed data sample.

The proton-dissociative events are characterized by the energy deposited in FCAL (Sec 3.2.2) or PRT (Sec. 3.2.4) by the proton fragments. For elastic events the proton, which stays intact in the interaction, travels down the beampipe undetected. Information from the two mentioned detectors can be used to distinguish between the two types of events. The extraction of the proton-dissociative sample is achieved by requiring a hit in the PRT or an energy deposit in the FCAL. Both these signatures ensure that the proton has disintegrated in the interaction into a hadronic system of higher mass.

The ratio of the number of events with a hit in the PRT to all events is presented in Fig. 5.9 as a function of $-t$ for ρ^0, ϕ and J/ψ mesons, both in data and the EPSOFT MC. Since the MC used in this analysis contains only proton-dissociative events the result obtained for EPSOFT represents the PRT tagging efficiency as simulated in MOZART [49] (see Sec.5.2). The observed efficiency saturates at the level of ~90% for $-t > 4$ GeV^2 both for ρ^0 and ϕ. For lower $-t$ values it decreases and at $-t = 1.1$ GeV^2 is no more than about 80%. For the $J\psi$ meson this ratio is flat at the level of ~85% in the whole t range.

The agreement between data and MC is good. Only in the lowest bins for $-t < 2.5$ GeV^2 the proton-dissociative MC is above the data points. This result shows that the data is con-

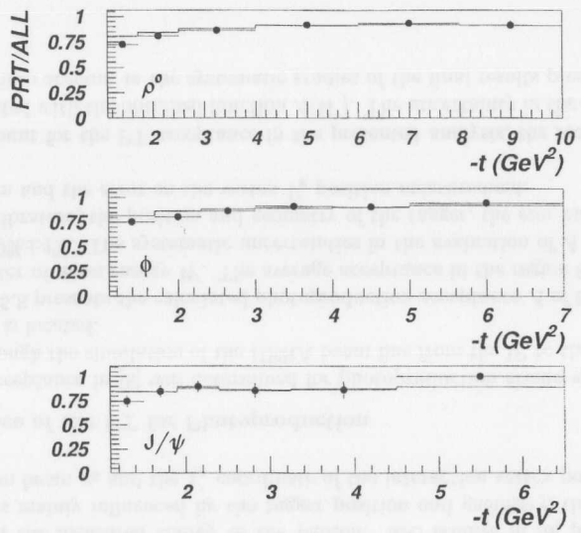

Figure 5.9: The comparison of the ratio of the number of events with a hit in the PRT to all events, between data (points) and EPSOFT MC (histogram).

taminated with elastic events, in which the proton as a whole escaped undetected down the beampipe. The observed contamination does not however exceed 12%.

The above study shows that the PRT tagging efficiency is between 80 and 90%. This means that the separation of proton-dissociative and elastic samples, by requiring a hit in the PRT, would cause an average loss of 15% of statistics. The data and MC agree within 12%, therefore in order to maximize the statistics in the analysis, the hit in the PRT was not required. The whole sample, as shown in Fig. 5.9, contains mainly proton-dissociative events, except for the lowest range in $-t$. For the final results the effects of the contamination with elastic events were taken into account as a source of systematic uncertainty, by requiring a hit in the PRT in the systematic studies.

5.5 Comparison of data and Monte Carlo

Since the acceptance depends on all kinematical variables (W, t, $cos\theta_h$, φ_h), it is important to have a MC simulation, which reproduces the data. To miminize the differences between the measured data distributions and the reconstructed MC distributions, the MC was reweighted. The reweighting in t and the decay angular distributions greatly improved the agreement between data and MC.

The unknown reweighting parameters $\vec{\lambda}$ are determined by finding the minima in the χ^2 function, which is defined as in [54]

$$\chi^2(\vec{\lambda}) = \sum_i \frac{(d_i - m_i(\vec{\lambda}))^2}{\sigma_i^2} \tag{5.6}$$

where d_i is the number of data events in bin i, $m_i(\vec{\lambda})$ is the number of MC events determined by $\vec{\lambda}$ in the corresponding bin and σ_i^2 is the error on the number of events in this bin. The MINUIT [55] package was used to perform the minimalization.

To reach agreement between the MC angular distributions and the data, the MC reweighting procedure was conducted iteratively. In the first step the acceptance corrections were calculated with the use of MC generated according to SCHC. The spin density matrix elements were determined as described in Chapter 6. Then the procedure was repeated using spin density matrix elements obtained in the first step, as weights to the MC. The whole procedure was repeated until the parameters converged.

5.5.1 Reweighting of the ρ^0 Monte Carlo

For the ρ^0 a one-dimensional and two-dimensional decay angular analyses were conducted. The spin density matrix elements – r^{04}_{00}, $\mathrm{Re}(r^{04}_{10})$ and r^{04}_{1-1} – measured in these analyses were parametrized in t and used to reweight the MC, which was generated with the assumption of SCHC, i.e. $r^{04}_{00} = \mathrm{Re}(r^{04}_{10}) = r^{04}_{1-1} = 0$.

The MC is therefore reweighted with the following formula

$$\frac{d\sigma}{dt} \sim \left(\frac{1}{M_N^2}\right)^{\beta(t)} W(\cos\theta_h, \phi_h) \tag{5.7}$$

where $\beta(t)$ is parametrized according to Eq. 5.2.

The matrix elements r^{04}_{00} and $\mathrm{Re}(r^{04}_{10})$ were found t independent, while the r^{04}_{1-1} matrix element was approximated by a linear function in t

$$r^{04}_{1-1} = r_0 + r_1 \cdot t \tag{5.8}$$

The parameters r^{04}_{00}, $\mathrm{Re}(r^{04}_{10})$, r_0 and r_1 were obtained form fits to the results of this analysis.

The final reweighting parameters and the errors corresponding to one standard deviation are summarized in Table 5.1.

parameter	value	error
r^{04}_{00}	0.0348	$\pm$0.010
$\mathrm{Re}(r^{04}_{10})$	0.0494	$\pm$ 0.008
r_0	-0.119	$\pm$ 0.022
r_1	0.016	$\pm$ 0.010

Table 5.1: The final reweighting parameters of the ρ^0 MC.

The t distribution was not properly generated in the MC, so it was reweighted with the use of the minimal χ^2 method, to reproduce the t-slope of the distribution in data. The agreement between data and MC reached after reweighting of the ρ^0 MC is depicted in Fig. 5.10, showing the comparison of the ρ^0 distributions in relevant kinematical variables The agreement between data and reconstructed MC is satisfactory.

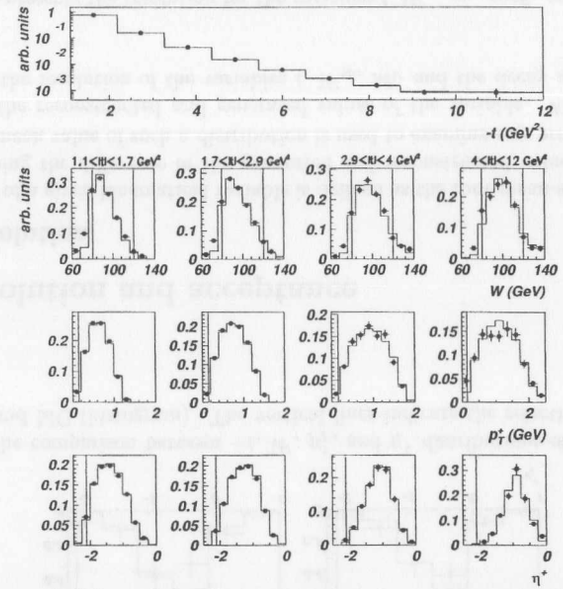

Figure 5.10: The comparison between $-t$, W, p_T^+, and η^+ distributions of ρ^0 candidates in data (points) and MC (histogram). The vertical lines indicate the selection cuts used in the analysis.

5.5.2 Reweighting of the ϕ Monte Carlo

For the ϕ also the one-dimensional and two-dimensional decay angular analyses were conducted. The spin density matrix elements – r^{04}_{00}, $\mathrm{Re}(r^{04}_{10})$ and r^{04}_{1-1} – measured in these analyses were parametrized in t and used to reweight the MC, which was generated with the assumption of SCHC.

$$\frac{d\sigma}{dt} \sim \left(\frac{1}{M_N^2}\right)^{\beta(t)} W(\cos\theta_h, \phi_h) \tag{5.9}$$

where $\beta(t)$ is parametrized according to Eq. 5.3.

The matrix elements r^{04}_{00} and $\mathrm{Re}(r^{04}_{10})$ were found t independent, and r^{04}_{1-1} matrix element was parametrized with a linear function as follows:

$$r^{04}_{1-1} = r_1 \cdot t \tag{5.10}$$

The parameters r^{04}_{00}, $\mathrm{Re}(r^{04}_{10})$ and r^{04}_{1-1} were obtained form fits to the results of this analysis.

The final reweighting parameters and the errors corresponding to one standard deviation are summarized in Table 5.2.

parameter	value	error
r_{00}^{04}	0.054	$\pm$ 0.016
$\mathrm{Re}(r_{10}^{04})$	0.055	$\pm$ 0.013
r_1	0.026	$\pm$ 0.009

Table 5.2: The final reweighting parameters of the ϕ MC.

The t distribution was also improperly generated in the MC, so it was reweighted with the use of the minimal χ^2 method, to describe the data. The agreement between data and MC reached after reweighting of the ϕ MC is depicted in Fig. 5.11, showing the comparison of the ϕ distributions in relevant kinematical variables. The agreement between data and reconstructed MC is satisfactory.

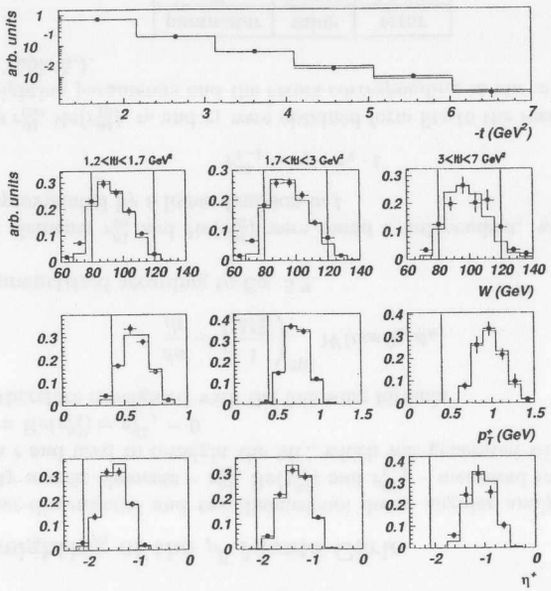

Figure 5.11: The comparison between $-t$, W, p_T^+, and η^+ distributions of ϕ candidates in data (points) and MC (histogram). The vertical lines indicate the selection cuts used in the analysis.

5.5.3 Reweighting of the J/ψ Monte Carlo

For the J/ψ it was possible to conduct only a one-dimensional decay angular analysis due to the low statistics of the sample. Both spin density matrix elements, r_{00}^{04} and r_{1-1}^{04}, were found t independent and the obtained parameterization was consistent with the SCHC expectations. The results obtained with the assumption of SCHC were therefore regarded as nominal, and the J/ψ MC was not reweighted with the decay angular distribution, but only with:

$$\frac{d\sigma}{dt} \sim \left(\frac{1}{M_N^2}\right)^{\beta(t)} , \qquad (5.11)$$

where $\beta(t)$ is parametrized according to Eq. 5.4.

Since also in the J/ψ case the t distribution was improperly generated, it was reweighted to describe the data, using the minimal χ^2 method. The agreement between data and MC reached after reweighting of the J/ψ MC is depicted in Fig. 5.12, showing the comparison of the J/ψ distributions in t, W, p_T^+, and η^+. The agreement between the data and the reconstructed MC is satisfactory.

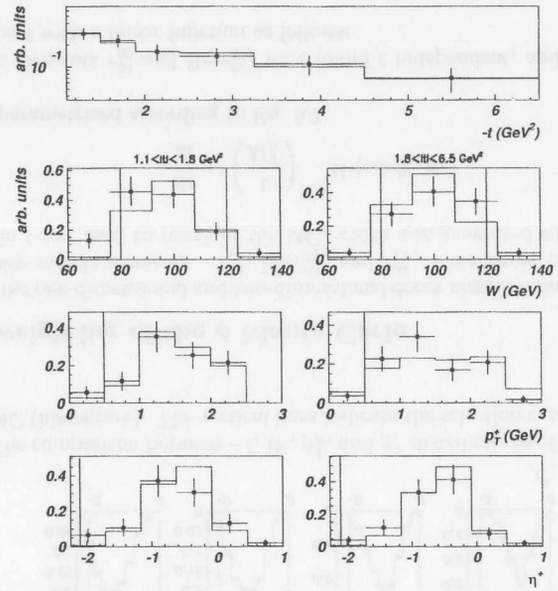

Figure 5.12: The comparison between $-t$, W, p_T^+, and η^+ distributions of J/ψ candidates in data (points) and MC (histogram). The vertical lines indicate the selection cuts used in the analysis.

5.6 Resolution and acceptance

5.6.1 Resolution

The resolution of a given kinematical variable is defined as the root-mean-square (RMS) of the distribution being the difference of the generated and reconstructed values of this particular variable. The mean value of such a distribution is used to examine any presumable systematic shift between the reconstructed and generated values of the variable. With the help of the EPSOFT MC the resolution of the variables t, $W_{\gamma p}$, M_V and the decay angles φ_h and $cos\theta_h$ was studied.

Figure 5.13 presents the resolution for the variables t, $W_{\gamma p}$, φ_h, $cos\theta_h$ and M_V as a function of the reconstructed $-t$ for ρ^0, ϕ and J/ψ mesons. Generally the resolution improves with

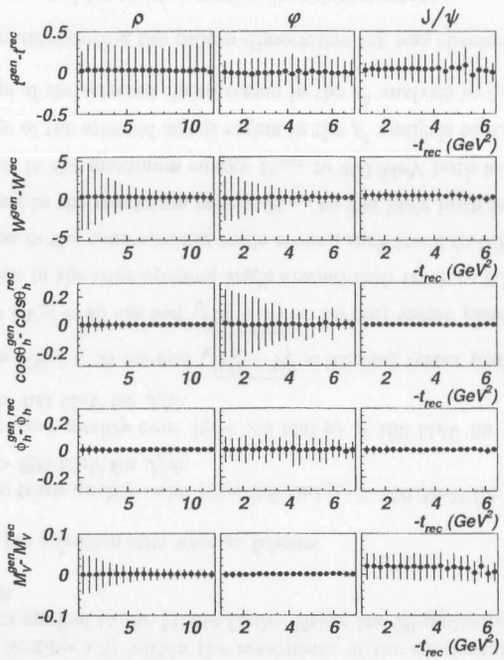

Figure 5.13: The resolution for t, $W_{\gamma p}$, φ_h, $cos\theta_h$ and M_V as a function of the reconstructed $-t$ for ρ^0, ϕ and J/ψ mesons.

increasing $-t$, since as $-t$ increases also the angle between the decay tracks and the Z-axis increases and therefore the tracks penetrate more CTD superlayers. This in turn improves the reconstruction of the track momenta (see Section 3.2.1) which influences strongly the resolution in all variables. In Table 5.3 the typical values of the resolution for different variables are summarized. The angular resolution depends on the opening angles between the meson decay

variable	ρ^0	ϕ	J/ψ
t (GeV^2)	0.30	0.15	0.10-0.20
W (GeV)	4.0-1.0	2.5-1.0	1.0
$\cos\theta_h$	0.06-0.01	0.20-0.05	0.01
φ_h (rad)	0.05-0.01	0.10	0.05
M_V (MeV)	50-10	5	25

Table 5.3: The typical resolutions for the variables t, $W_{\gamma p}$, φ_h, $cos\theta_h$ and M_V for ρ^0, ϕ and J/ψ mesons.

products. If the tracks are not well spatially separated the angular resolution deteriorates significantly, which is the case for the ϕ meson. The opening angle between the two kaons from

the ϕ decay are relatively small compared to the angles between the decay products of the ρ^0 and J/ψ mesons.

No systematical differences are observed between the reconstructed and generated variables, except for the reconstruction of the invariant mass of the J/ψ meson. The electrons radiate photons in the magnetic field, what causes a 20 MeV systematic shift of the reconstructed J/ψ mass for the electron decay channel.

5.6.2 Acceptance

The acceptance in a given bin was determined from the MC as the ratio of the number of reconstructed MC events accepted by the selection cuts to the number of the generated events in a certain kinematic range. The acceptance calculated in this manner accounts for the detector and reconstruction efficiencies, the geometrical acceptance the detector resolution and the trigger efficiency. The data distributions are then corrected for this acceptance and further analyzed.

The determination of the REMC trigger efficiency (Sec. 5.3.1) and the PT acceptance (Sec. 5.3.2) are included in the determination of the acceptance in different kinematical variables, which is presented in Figure 5.14 for the ρ^0, ϕ and J/ψ mesons. The inefficiency at low $-t$

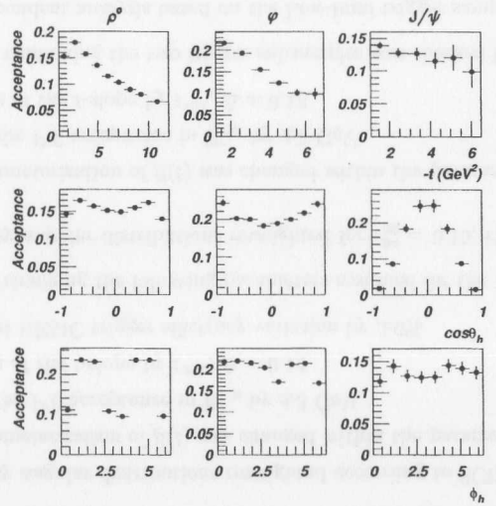

Figure 5.14: The overall acceptance as a function of $-t$, $cos\theta_h$ and φ_h for the ρ^0 (left), ϕ (center) and J/ψ (right) mesons.

as well as the strong variation of the acceptance in φ_h for the ρ^0 and ϕ mesons are due to the small opening angles of the decay particles. As a result many very backward tracks (see the η^+ distributions in Figure 5.10) are outside of the CTD geometrical acceptance.

Chapter 6

Results

The goal of this decay angle analysis is to determine some of the ρ^0, ϕ and J/ψ spin density matrix elements and their dependence on t for $-t$ values up to 12 GeV^2. The seemly large statistics of the present sample allows to perform the $M_{\pi\pi}$, M_{KK} and M_{ll} analyses, for ρ^0, ϕ and J/ψ respectively, not only in bins of t, but also in bins of the helicity angles. This procedure makes it possible to directly extract the vector meson resonant contribution as a function of the helicity angles and in this way to correct for the nonresonant background.

6.1 Estimate of systematic uncertainties

The systematic uncertainty was determined by either varying the selection cuts applied in the analysis (see Section 4.3) within the resolutions of the cut variables or by changing the reweighting factors applied to the Monte Carlo. Below the 29 performed systematic checks are described in detail.

- Changes in the selection cuts were as follows:

  1. Tighter track quality cuts: $|\eta| < 2.0$ and $p_T > 200$ MeV for ρ^0, $p_T > 500$ MeV for ϕ or $p_T > 600$ MeV for J/ψ.
  2. Looser track quality cuts: $|\eta| < 2.2$ and $p_T > 100$ MeV for ρ^0, $p_T > 300$ MeV for ϕ or $p_T > 400$ MeV for J/ψ.
  3. Tighter ($|V_Z| < 35$ cm and $\sqrt{V_X^2 + V_Y^2} < 0.5$ cm) vertex position cuts.
  4. Looser ($|V_Z| < 45$ cm and $\sqrt{V_X^2 + V_Y^2} < 1.0$ cm) vertex position cuts.
  5. Decrease in the cone opening angle around each track to 0.15 rad.
  6. Increase in the cone opening angle around each track to 0.25 rad.
  7. Decrease in the maximum energy E_{max} to 200 MeV both in BCAL and RCAL
  8. Increase in the maximum energy E_{max} to 300 MeV both in BCAL and RCAL
  9. Change of the selected signal region in the ρ^0 analysis to $0.65 < M_{\pi\pi} < 1.2$ GeV.
  10. Change of the selected signal region in the ρ^0 analysis to $0.45 < M_{\pi\pi} < 1.0$ GeV.

- The effect of introducing the proton-dissociative tag was checked:

  11. PRT was used for tagging proton-dissociative events.

- The effects of changing the following parameters assumed for the ρ^0 MC were checked:

  12. The decay angular distributions reweighted according to SCHC expectations.
  13. Constant background instead of linear in $M_{\pi\pi}$ was assumed.
  14. The parameterization of $\beta(t)$ was changed within the parameter uncertainties.
  15. Shift in the PT acceptance in $W_{\gamma p}$ by ± 3 GeV.
  16. variation of the t-slope by $t^{\pm\Delta}$, $\Delta = 0.04$
  17. Simulated REMC trigger efficiency variation by $\pm 6\%$

- The effects of changing the following parameters assumed for the ϕ MC were checked:

  18. The decay angular distributions reweighted according to SCHC expectations.
  20. The parameterization of $\beta(t)$ was changed within the parameter uncertainties.
  21. Shift in the PT acceptance in $W_{\gamma p}$ by ± 3 GeV.
  22. Variation of the t-slope by $t^{\pm\Delta}$, $\Delta = 0.14$
  23. Simulated REMC trigger efficiency variation by $\pm 6\%$

- The effects of changing the following parameters assumed for the $J\psi$ MC were checked:

  24. The decay angular distributions reweighted for $r^{04}_{00} = 0.15$, $r^{04}_{1-1} = 0.11$ and $r^{04}_{1-1} = -0.11$.
  25. The parameterization of $\beta(t)$ was changed within the parameter uncertainties.
  26. Shift in the PT acceptance in $W_{\gamma p}$ by ± 3 GeV.
  27. Variation of the t-slope by $t^{\pm\Delta}$, $\Delta = 0.18$

- The effects of combining the two trigger subsamples was checked by performing:

  28. An independent analysis based on the Low-lumi trigger sample only.
  29. An independent analysis based on the High-lumi trigger sample only.

The systematic uncertainty was determined by repeating the full analysis for each systematic check. The effect of the variation of the selection cuts within the resolution of the cut variables (checks 1-8) was less than ± 0.03 on the spin density matrix elements. The uncertainty in the ρ^0 signal extraction (checks 9,10,13) had an effect of less than ± 0.01 on the ρ^0 matrix elements. The effect from requiring a hit in the PRT (check 11) was always much smaller than 0.01.

The modeling of the proton dissociative system N (checks 14,20,25) through the variation of the $\beta(t)$ parameterization within parameter uncertainties had no effect on the spin density matrix elements for all mesons. The reweighting of different MC distributions (t,W,$cos\theta_h$,φ_h) within the range allowing to maintain satisfactory agreement between data and MC (checks 12,15,16,18,21,22,24,26,27) affected the spin density matrix elements by about 0.01. In particular the variation in the MC t slope by a factor $t^{\pm\Delta}$ (in checks 16, 22, and 27) is connected to the cross section measurements performed in [8]. There the prediction of [3, 4] that the cross section $d\sigma/dt$ behaves like a power-like function $A \cdot |t|^{-n}$ at large $-t$ is tested. Here Δ is equal to twice the error on the measured power n for each meson respectively. The variation of the RCAL EMC trigger efficiency within its uncertainty (checks 17,23) changed the spin density

matrix elements by about 0.01.

The systematic uncertainties due to the differences in the results for the Low-Lumi trigger and for the High-Lumi trigger (check 28,29) are not included in the systematic error. The Low-Lumi trigger corresponds to 30% of the luminosity and the statistical fluctuations are quite large. All deviations from the nominal results are smaller than the (large) statistical uncertainty of the check and should therefore not be taken as a systematic uncertainty. The results of the systematic error analysis are summarized in Tables A.1–A.12 in Appendix A.

6.2 ρ^0 decay angle analysis

6.2.1 One-dimensional analysis in the helicity frame

The helicity analysis for ρ^0 was performed in four $-t$ bins. The ρ^0 signal was extracted in each of the eight $cos\theta_h$ and eight φ_h bins within each $-t$ bin. This was achieved by fitting the $M_{\pi\pi}$ distribution with a parameterization inspired by the Söding model [56], where the Breit-Wigner (BW) amplitude is distorted by the interference with non-resonant two-pion production:

$$\frac{d\sigma}{dM_{\pi\pi}} = A^2 \left[\left| \frac{\sqrt{M_{\pi\pi} M_\rho \Gamma_\rho}}{M_{\pi\pi}^2 - M_\rho^2 + iM_\rho\Gamma_\rho} + B/A \right|^2 + f \right], \tag{6.1}$$

where M_ρ is the ρ^0 mass and Γ_ρ is the momentum dependent width :

$$\Gamma_\rho(M_{\pi\pi}) = \Gamma_0 \left(\frac{q}{q_0}\right)^3 \frac{M_\rho}{M_{\pi\pi}}, \tag{6.2}$$

where Γ_0 is the ρ^0 width, q is the π momentum in the $\pi\pi$ rest frame and q_0 is the value of q for $M_{\pi\pi} = M_\rho$. The normalization factor of the resonant amplitude is denoted by A, and B is the non-resonant $\pi\pi$ production amplitude (assumed $M_{\pi\pi}$-independent). Another term

$$f = A_f(1 + 1.5M_{\pi\pi}) \tag{6.3}$$

linear in $M_{\pi\pi}$ [57] was introduced to account for the background from photon diffractive dissociation ($\gamma p \to XN$). For the mass fits in all the $-t$ and angular bins the ρ^0 mass and width were fixed at 770 MeV and 150.7 MeV respectively, leaving A, B/A and A_f as fit parameters. The results of fits to the acceptance corrected $M_{\pi\pi}$ distributions in angular and $-t$ bins are presented in Figures 6.1 and 6.2.

The spin density matrix elements r_{00}^{04} and r_{1-1}^{04} were obtained through 1-dimensional fits of Eq. (2.52) and (2.53) to the normalized helicity distributions of the extracted ρ^0 signal in the 4 $-t$ bins under study. The fits to the helicity distributions are presented in Figure 6.3

6.2.2 Two-dimensional analysis in the helicity frame

The double dimensional helicity analysis for ρ^0 was performed in three $-t$ bins. The ρ^0 signal was extracted in each of the 3×5 ($cos\theta_h \times \phi_h$) angular bins within each $-t$ bin. This was achieved by fitting equation (6.1) to the acceptance corrected dipion invariant mass distributions. As an example the resulting mass fits obtained in the first $-t$ bin are presented in Figure 6.4.

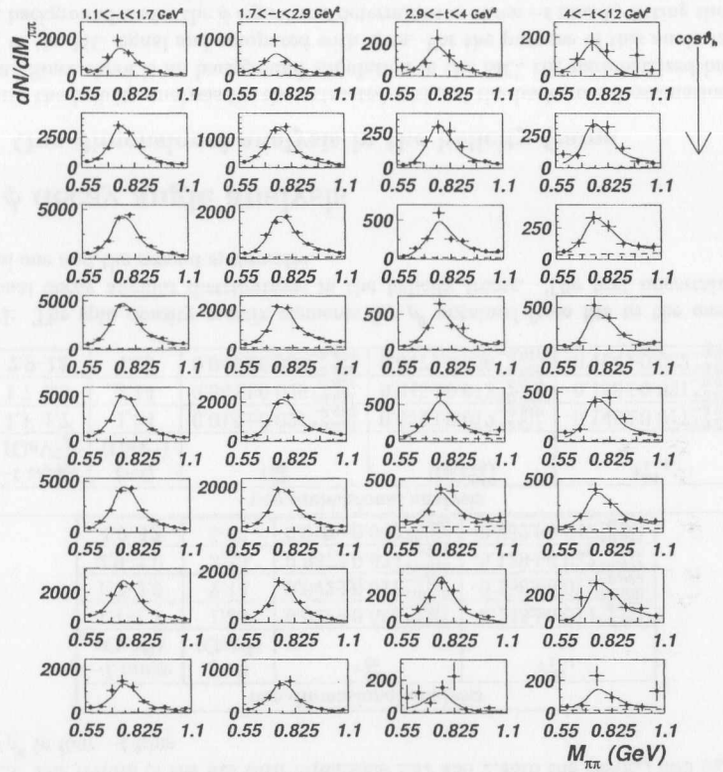

Figure 6.1: The results of the fits to $M_{\pi\pi}$ distributions in four bins of $-t$ and eight bins of $cos\theta_h$ for ρ^0. The nonresonant background contribution is presented as a dashed line.

The angular dependence of the extracted ρ^0 resonant contribution in each $-t$ bin is then fitted with the double-dimensional angular distribution function from equation (2.51). From these fits besides the r_{00}^{04} and r_{1-1}^{04} spin density matrix elements, also the $\mathrm{Re}(r_{10}^{04})$ element is determined.

6.2.3 ρ^0 spin density matrix elements

In this section the results of the angular fits to the decay angular distributions of the extracted ρ^0 signal are presented. The measured ρ^0 spin density matrix elements versus $-t$ are displayed in Figure 6.5 in comparison to the earlier ZEUS measurements and summarized in Table 6.1.

The results of this analysis are in good agreement with the previous ZEUS results. The measurements of r_{00}^{04} show that the helicity single-flip contribution is small over the entire $-t$ range under study. The small value of r_{00}^{04} indicates that the probability for the ρ^0 to be

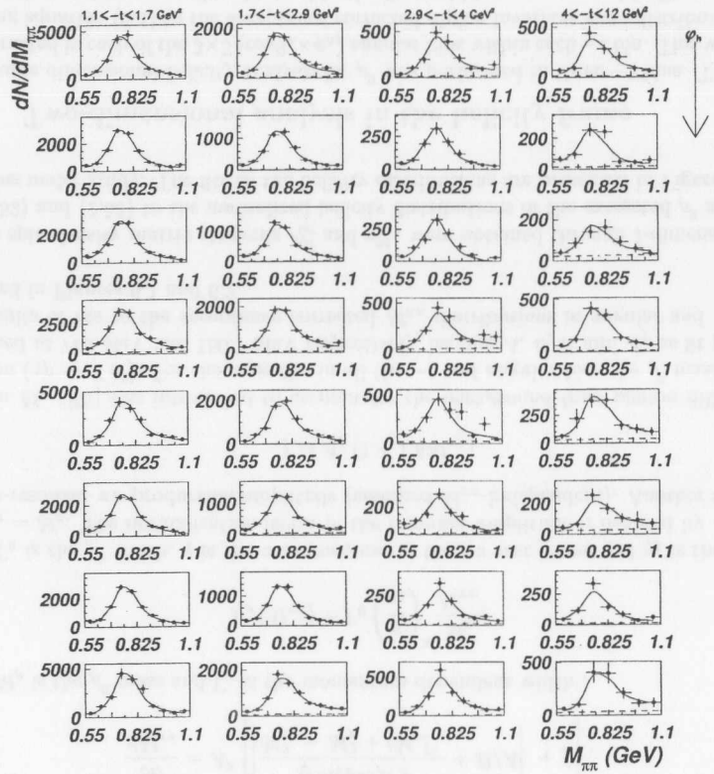

Figure 6.2: The results of the fits to $M_{\pi\pi}$ distributions in four bins of $-t$ and eight bins of φ_h for ρ^0. The nonresonant background contribution is presented as a dashed line.

produced with longitudinal polarization is less than 15% even at $t = 5.6$ GeV^2.

The measured non-zero values of $\mathrm{Re}(r^{04}_{10})$ clearly indicate a helicity single-flip contribution. The measurements of r^{04}_{1-1} show a clear helicity double-flip contribution. The obtained results lead to the conclusion that in the case of the ρ^0 meson SCHC is violated with a statistical significance of 3 standard deviations at such large values of $-t$.

The comparison between the measured angular distributions in data and MC presented in Figure 6.6 seems to prove the deviation from SCHC. The MC reweighted with the results of this analysis describes the data much better than the MC in which SCHC was assumed.

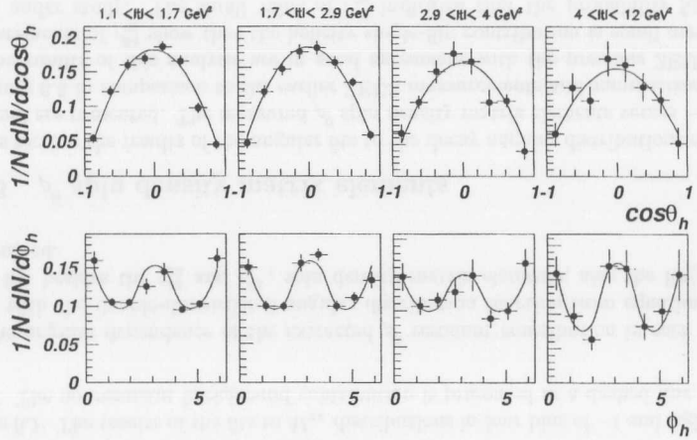

Figure 6.3: The results of the fits with Equations 2.52 and 2.53to the $cos(\theta_h)$ and φ_h distributions for ρ^0 in four $-t$ bins

one dimensional analysis			
$-t$ range (GeV^2)	$\langle -t \rangle$ (GeV^2)	r^{04}_{00}	r^{04}_{1-1}
1.1–1.7	1.34	$0.022 \pm 0.016^{+0.016}_{-0.018}$	$-0.143 \pm 0.014^{+0.023}_{-0.031}$
1.7–2.9	2.14	$0.042 \pm 0.017^{+0.018}_{-0.021}$	$-0.158 \pm 0.017^{+0.020}_{-0.022}$
2.9–4.0	3.35	$0.037 \pm 0.034^{+0.032}_{-0.036}$	$-0.129 \pm 0.032^{+0.023}_{-0.050}$
4.0–12	5.67	$0.090 \pm 0.049^{+0.035}_{-0.040}$	$-0.252 \pm 0.047^{+0.044}_{-0.023}$

two dimensional analysis				
$-t$ range (GeV^2)	$\langle -t \rangle$ (GeV^2)	r^{04}_{00}	$\mathrm{Re}(r^{04}_{10})$	r^{04}_{1-1}
1.1–1.7	1.34	$0.018 \pm 0.021^{+0.013}_{-0.016}$	$0.054 \pm 0.012^{+0.017}_{-0.010}$	$-0.145 \pm 0.017^{+0.031}_{-0.025}$
1.7–2.9	2.14	$0.044 \pm 0.026^{+0.021}_{-0.024}$	$0.045 \pm 0.013^{+0.016}_{-0.010}$	$-0.138 \pm 0.021^{+0.013}_{-0.019}$
2.9–12	4.38	$0.049 \pm 0.039^{+0.026}_{-0.024}$	$0.047 \pm 0.020^{+0.009}_{-0.017}$	$-0.194 \pm 0.032^{+0.024}_{-0.042}$

Table 6.1: The spin density matrix elements for ρ^0 obtained from fits to the one and two dimensional decay angular distributions in the helicity frame. The first uncertainty is the statistical one and the second systematic.

6.3 ϕ decay angle analysis

6.3.1 One-dimensional analysis in the helicity frame

To perform the helicity analysis for the extracted ϕ signal the background estimation must be done first. Since there is no background simulation in the MC, the parametrized background is added to the MC signal and compared with data. For the purpose of this analysis the non-resonant background under the ϕ signal was determined in three $-t$ bins by fitting the observed mass spectra in the range $0.99 < M_{KK} < 1.15 GeV$. A relativistic Breit-Wigner (BW) function

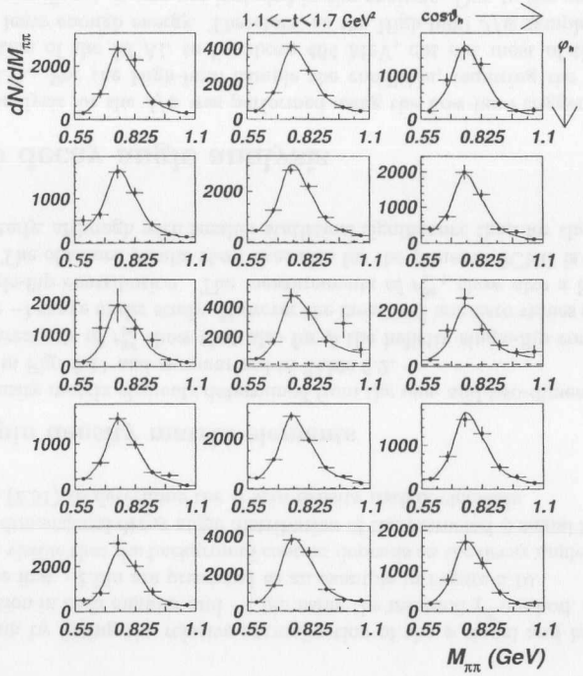

Figure 6.4: The results of the fits with equation (6.1) to $M_{\pi\pi}$ distributions in the first $-t$ bin and in 3×5 ($cos\theta_h \times \phi_h$) angular bins for ρ^0.

convoluted with a Gaussian function to account for finite tracking resolution was fitted to the data over a function describing the background.

The non-resonant background under the ϕ peak is mainly due to diffractive ρ^0 production, which means that ρ^0 events are incorrectly reconstructed with the kaon mass. The study of the invariant mass distributions of the ρ^0 MC events, for which the two pions are given the kaon mass, results with the parameterization of the background contribution as a function of M_{KK}. The deduced shape of this background is given by the following power-like function:

$$BG = A_{BG} \cdot (M_{KK} - 2M_K)^{\delta_\phi}, \tag{6.4}$$

where A_{BG}, being the background normalization, and δ_ϕ are parameters determined by the fit. In the fits the ϕ mass was fixed at 1019.417 MeV and the width of the Breit-Wigner function at 4.458 MeV leaving only three free parameters: the resonance normalization, A_{BG} and δ_ϕ.

The helicity analysis for ϕ was performed in three $-t$ bins. The ϕ signal was extracted in

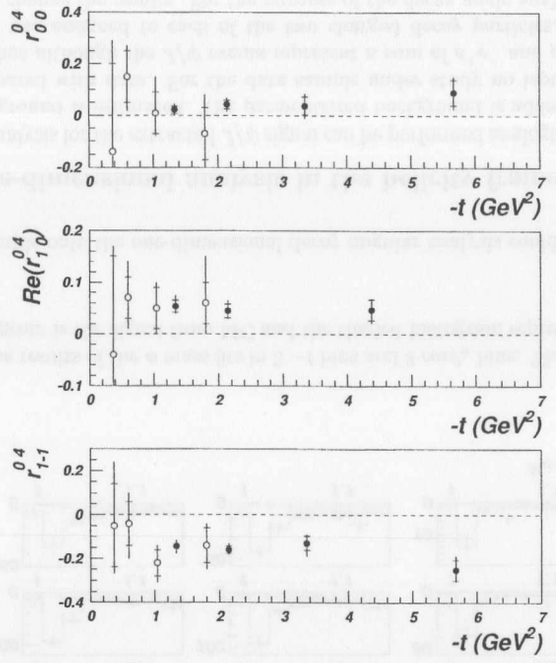

Figure 6.5: The measured values of spin density matrix elements for proton-dissociative ρ^0 photoproduction as a function of $-t$. The full circles correspond to the results of this analysis, while th open ones are the published ZEUS results [7]. The inner error bars represent the statistical uncertainty, and the outer ones the statistical and systematical uncertainties added in quadrature.

each of the eight $cos\theta_h$ and eight φ_h bins within every $-t$ bin. This was achieved by fitting the relative normalization of the ϕ signal and background for the M_{KK} distribution in each angular and $-t$ bin using the minimal χ^2 method (see Eq 5.6). The results of these fits are presented in Figures 6.7 and 6.8, where the points are the data, the solid histograms the signal from the Monte Carlo, and the shaded histograms represent the background contribution.

The normalized and acceptance corrected decay angle distributions of the extracted ϕ signal and the corresponding one-dimensional angular fits of Eq. (2.52) and (2.53) are presented in Fig. 6.9.

6.3.2 Two-dimensional analysis in the helicity frame

The double dimensional helicity analysis for ϕ was performed in two $-t$ bins. The ϕ signal was extracted in each of the 3×5 ($cos\theta_h \times \phi_h$) angular bins within each $-t$ bin. This was

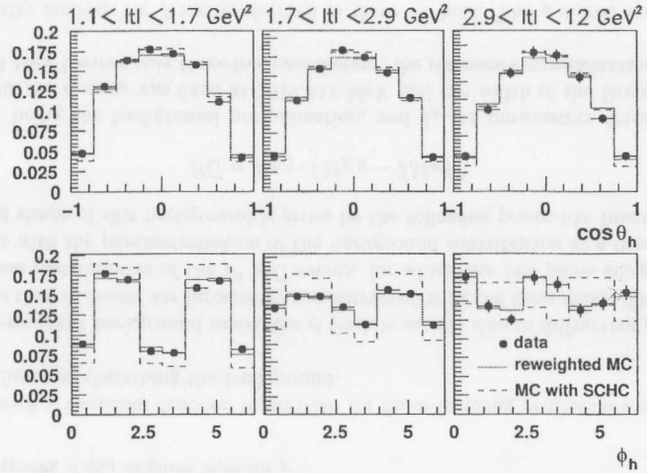

Figure 6.6: The comparison of the measured angular distributions in data and MC in three ranges of $-t$ for the ρ^0 meson. The points are the data, the solid line is the MC reweighted with the results of this analysis and the dashed line represents the MC with SCHC assumed.

performed again by fitting the relative normalization of the ϕ signal and background for the M_{KK} distribution in each angular and $-t$ bin using the minimal χ^2 method. The results of the mass fits in the first $-t$ bin are presented as an example in Figure 6.10.

It is clearly visible that the background content depends on the decay angles. The acceptance corrected two-dimensional decay angle distribution of the extracted ϕ signal in each $-t$ bin was fitted with Eq.(2.51) to determine the ϕ spin density matrix elements.

6.3.3 ϕ spin density matrix elements

The ϕ spin density matrix elements determined from the one- and two-dimensional angular fits are presented in Fig. 6.11 and summarized in Table 6.2.

The measurements of r^{04}_{00} show that also for ϕ the helicity single-flip contribution is small over the entire $-t$ range under study. However the measured non-zero values of $\mathrm{Re}(r^{04}_{10})$ indicate a helicity single-flip contribution. The measurements of r^{04}_{1-1} show also a helicity double-flip contribution. The obtained results show that also for the ϕ meson SCHC is violated in the $-t$ range under study, although with smaller statistical significance than for the ρ^0.

6.4 J/ψ decay angle analysis

The helicity analysis for the J/ψ was performed using the Low-lumi trigger data sample only (see Sec. 5.3.1). For the High-lumi sample the condition, requiring the energy deposit in the EMC section of the RCAL to be above 464 MeV, cut out most of the J/ψ events, as muons didn't leave enough energy. Therefore, as the High-lumi J/ψ sample turned out to be statistically insignificant, it was not included in the analysis. Due to the overall low statistics

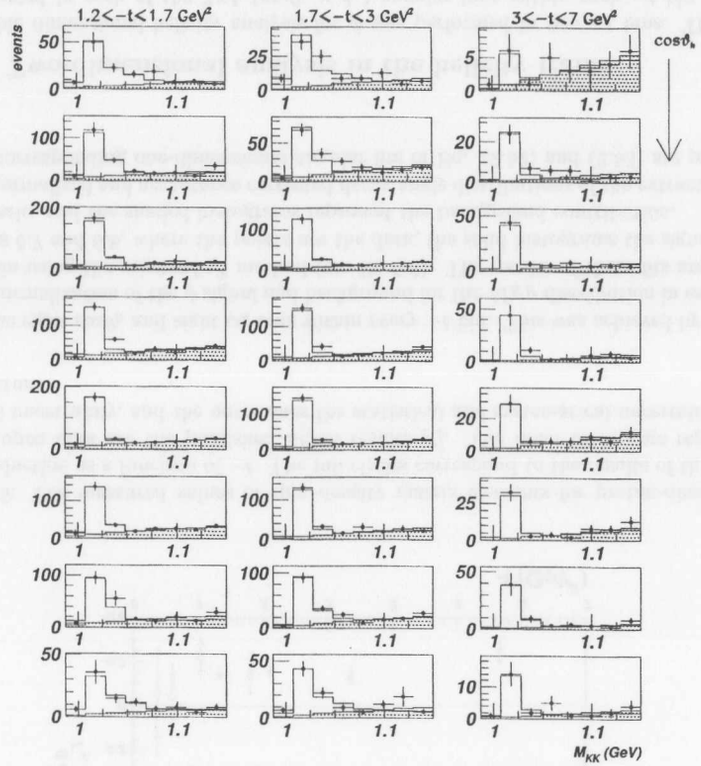

Figure 6.7: The results of the ϕ mass fits in 3 $-t$ bins and 8 $cos\theta_h$ bins. The points are the data, the solid histogram is the signal from MC and the shaded histogram represents the background contribution.

of the J/ψ sample only the one-dimensional decay angular analysis could be performed.

6.4.1 One-dimensional analysis in the helicity frame

The helicity analysis for the extracted J/ψ signal can be performed analogically to the ϕ analysis once the background is estimated. The parametrized background is added to the signal in the MC and compared with data. For the data sample under study no lepton identification was performed. Thus although the J/ψ events represent a sum of e^+e^- and $\mu^+\mu^-$ final states, the electron mass was assigned to each of the two charged decay particles, assuming the muon mass does not change the results. For the purpose of the decay angle analysis the non-resonant

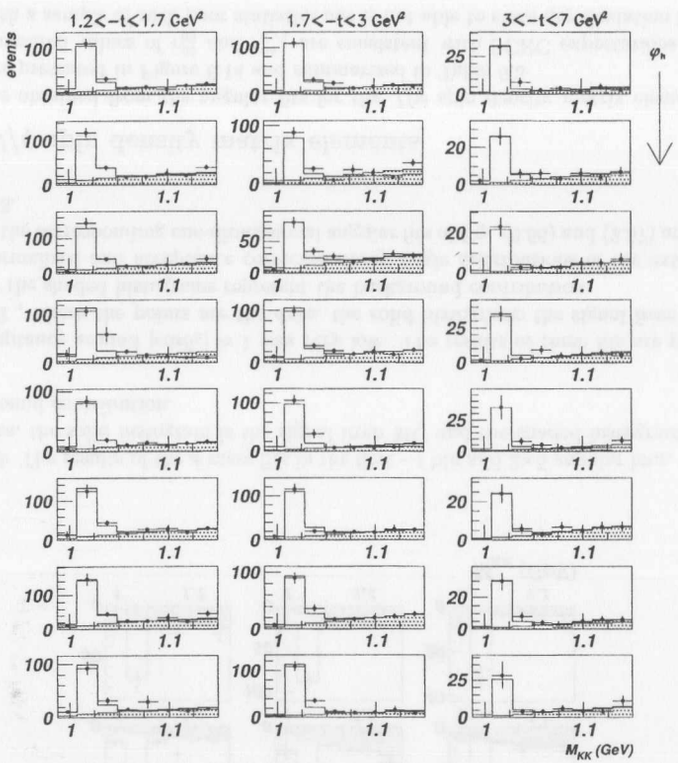

Figure 6.8: The results of the ϕ mass fits in 3 $-t$ bins and 8 φ_h bins. The points are the data, the solid histogram is the signal from MC and the shaded histogram represents the background contribution.

background under the J/ψ peak was determined in two $-t$ bins by fitting the observed mass spectra in the range $2.3 < M_{ee} < 3.4GeV$. A sum of a Gaussian function (muon decay channel) and a bremsstrahlung function convoluted with a Gaussian function (electron decay channel) with equal weights was fitted to the data over an exponential background of the form:

$$BG = A_{BG} \cdot e^{\delta_{J/\psi} \cdot M_{ee}} \tag{6.5}$$

This form of the background turned out to be the best possible parameterization in the wide range of the fit considered. The free parameters of the fit were the normalization, A_{BG} and $\delta_{J/\psi}$ as the J/ψ mass and width were fixed at PDG values.

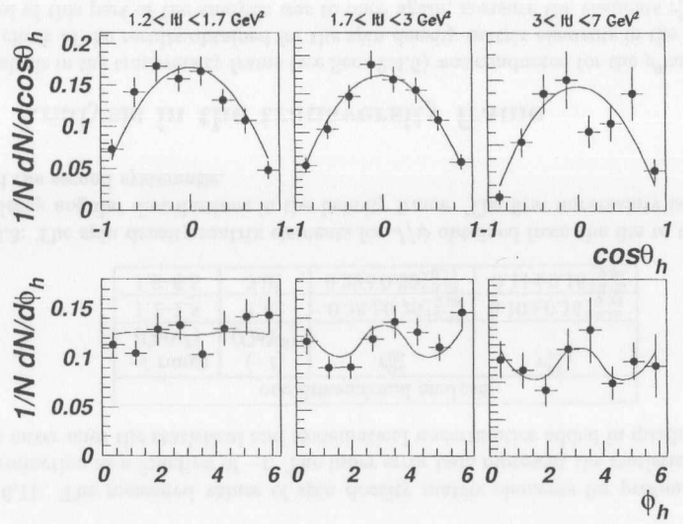

Figure 6.9: The results of the fits to the acceptance and background corrected ϕ angular distributions in 3 $-t$ bins.

one dimensional analysis			
$-t$ range (GeV²)	$\langle -t \rangle$ (GeV²)	r^{04}_{00}	r^{04}_{1-1}
1.2–1.7	1.42	$0.080 \pm 0.028^{+0.020}_{-0.026}$	$0.008 \pm 0.033^{+0.011}_{-0.039}$
1.7–3.0	2.20	$0.066 \pm 0.025^{+0.034}_{-0.021}$	$-0.085 \pm 0.032^{+0.023}_{-0.028}$
3.0–7.0	4.03	$-0.020 \pm 0.035^{+0.034}_{-0.018}$	$-0.108 \pm 0.058^{+0.053}_{-0.030}$

two dimensional analysis				
$-t$ range (GeV²)	$\langle -t \rangle$ (GeV²)	r^{04}_{00}	$\mathrm{Re}(r^{04}_{10})$	r^{04}_{1-1}
1.2–1.7	1.42	$0.070 \pm 0.047^{+0.040}_{-0.017}$	$0.053 \pm 0.021^{+0.019}_{-0.024}$	$-0.078 \pm 0.041^{+0.037}_{-0.027}$
1.7–7.0	2.72	$0.083 \pm 0.041^{+0.022}_{-0.044}$	$0.057 \pm 0.018^{+0.013}_{-0.007}$	$-0.079 \pm 0.035^{+0.008}_{-0.017}$

Table 6.2: The spin density matrix elements for ϕ obtained from fits to the one and two dimensional decay angular distributions in the helicity frame. The first uncertainty is the statistical and the second the systematic.

The helicity analysis for J/ψ was performed in only two $-t$ bins due to the limited statistics of the sample. The J/ψ signal was extracted in each of the four $cos\theta_h$ and five φ_h bins within every $-t$ bin. This was achieved by fitting the relative normalization of the J/ψ signal and background for the M_{ee} distribution in each angular and $-t$ bin using the minimal χ^2 method (see Eq. 5.6). The $cos\theta_h$ range under study was for J/ψ limited to the range $|cos\theta_h| < 0.9$

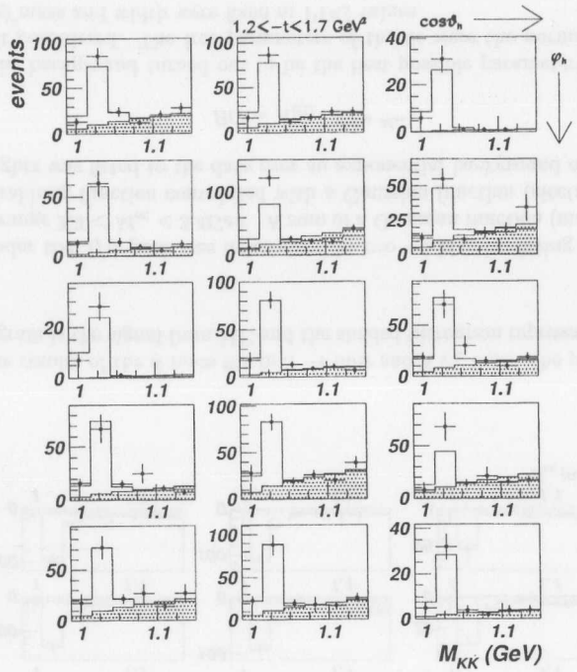

Figure 6.10: The results of the ϕ mass fits in the first $-t$ bin and 3×5 angular bins. The points are the data, the solid histogram is the signal from MC and the shaded histogram represents the background contribution.

as the acceptance around $|cos\theta_h| \approx 1$ was very low. The results of these fits are presented in Figure 6.12 , where the points are the data, the solid histograms the signal from the Monte Carlo, and the shaded histograms represent the background contribution.

The normalized and acceptance corrected decay angle distributions of the extracted J/ψ signal and the corresponding one-dimensional angular fits of Eq. (2.56) and (2.57) are presented in Fig. 6.13.

6.4.2 J/ψ spin density matrix elements

The results obtained from the angular fits for the J/ψ spin density matrix elements in this analysis are presented in Figure 6.14 and summarized in Table 6.3

The measured values of r^{04}_{00} and r^{04}_{1-1} are consistent with SCHC expectations within the errors. With a sample of such poor statistics one is not able to state any deviation from SCHC for J/ψ.

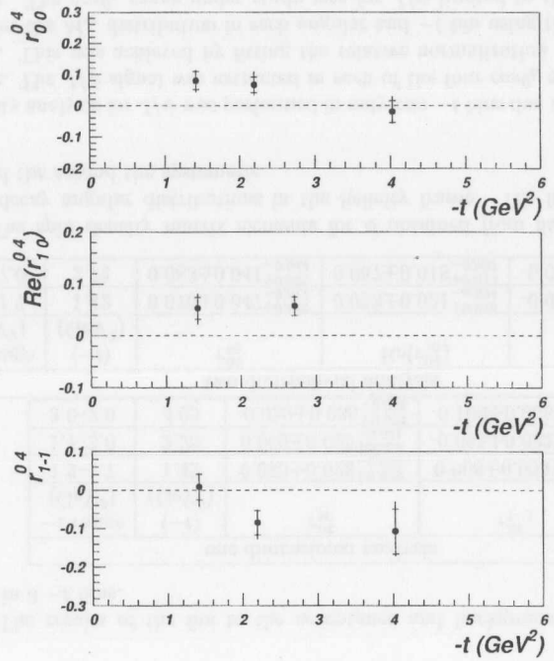

Figure 6.11: The measured values of spin density matrix elements for proton-dissociative ϕ photoproduction as a function of $-t$. The inner error bars represent the statistical uncertainty, and the outer ones the statistical and systematical uncertainties added in quadrature.

one dimensional analysis			
$-t$ range (GeV²)	$\langle -t \rangle$ (GeV²)	r^{04}_{00}	r^{04}_{1-1}
1.1–1.8	1.42	$-0.28 \pm 0.26^{+0.28}_{-0.08}$	$0.10 \pm 0.15^{+0.16}_{-0.03}$
1.8–6.5	3.01	$0.22 \pm 0.30^{+0.38}_{-0.11}$	$-0.11 \pm 0.16^{+0.06}_{-0.04}$

Table 6.3: The spin density matrix elements for J/ψ obtained from the fits to the one dimensional decay angular distributions in the helicity frame. The first uncertainty is the statistical one and the second systematic.

6.5 Analysis in the transversity frame

The analysis in the transversity frame (see Sec. 2.4.5) was conducted for the ρ^0 and ϕ mesons as a cross check of the results obtained for the spin density matrix elements in the helicity frame. The goal of this part of the analysis was to once again, measure the elements r^{04}_{00}, $\mathrm{Re}(r^{04}_{10})$ and r^{04}_{1-1} of the spin density matrix in the helicity frame starting however from the statistical tensors

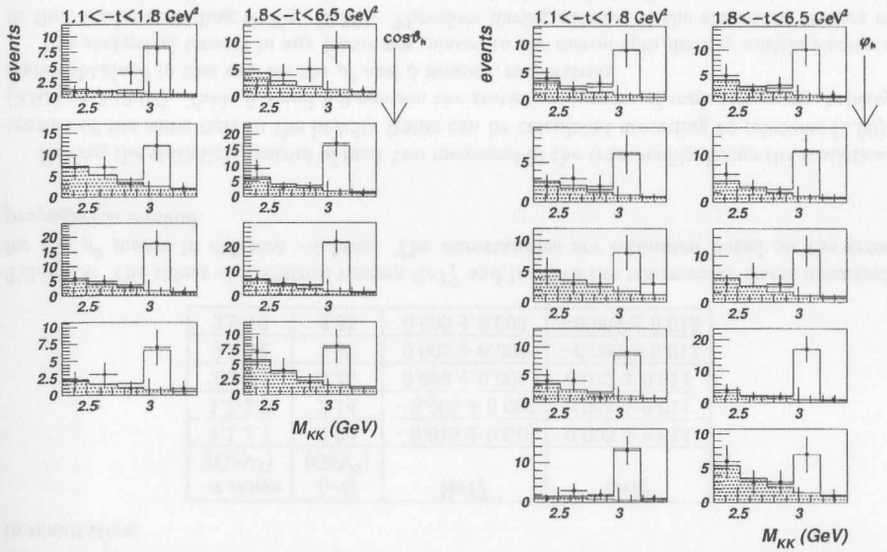

Figure 6.12: The results of the J/ψ mass fits conducted in two $-t$ bins and 4 $\cos\theta_h$ bins (left plot) or in 5 φ_h bins (right plot). The points are the data, the solid histogram is the signal from MC and the shaded histogram represents the background contribution.

in the transversity frame. The analysis was performed for the two mesons in the same bins in $-t$ as in the helicity frame, therefore the results obtained in both analyses can be directly compared.

To determine the statistical tensors T^J_M in the transversity frame the mean values of the corresponding spherical harmonics $Y^J_M(\theta_t, \varphi_t)$ were calculated (see Eq.(2.76)). The errors on the spherical harmonics were calculated using the error propagation method, where the initial errors on θ_t and ϕ_t were estimated in 40 angular bins respectively in the whole $-t$ range. The errors therefore were calculated from equations (2.87)–(2.89) in the following way:

$$\Delta Y^J_M(\theta_t, \varphi_t) = \sqrt{\left(\frac{\partial Y^J_M}{\partial \theta_t} \cdot \Delta\theta_t\right)^2 + \left(\frac{\partial Y^J_M}{\partial \varphi_t} \cdot \Delta\varphi_t\right)^2}, \tag{6.6}$$

where $\Delta\theta_t$ and $\Delta\varphi_t$ were evaluated by measuring the difference between the mean values of the generated and reconstructed angular distributions in the MC in each of the 40 bins in θ_t and ϕ_t respectively. Distributions of the uncertainties resulting from equation (6.6) for each spherical harmonic were studied. The mean values of these distributions were regarded as estimates of uncertainties for the mean values of the respective spherical harmonics. The errors $\Delta Y^J_M(\theta_t, \varphi_t)$ calculated in this manner depend on the angle detection resolution and should thus be treated as systematic uncertainties. The statistical errors on the mean values of spherical harmonics

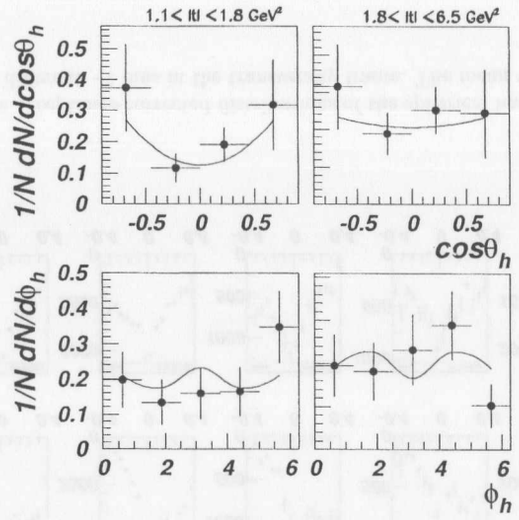

Figure 6.13: The results of the fits to the $cos\theta_h$ and φ_h distributions for J/ψ with Eq. (2.56) and (2.57 respectively in two ranges of $-t$.

under study correspond to at the most 25% of the calculated systematic uncertainties, therefore added in quadrature lead to an increase of the total errors by no more than 3%. Taking this fact into account it was concluded that the statistical uncertainties on the mean spherical harmonics can be neglected in further analysis, compared to the systematic ones. The errors on the statistical tensors in the transversity frame, in the helicity frame, and finally the spin density matrix elements were obtained also on the basis of the error propagation method.

The results of all the steps of this part of the analysis will be presented for the ρ^0 and ϕ mesons. The acceptance-corrected distributions of the relevant spherical harmonics Y^2_M in different $-t$ bins are presented in Figures 6.15 and 6.16 for the ρ^0 and ϕ mesons, respectively.

From these measured mean values of spherical harmonics of rank two the statistical tensors of that rank in the transversity frame were calculated, by dividing the mean by the coefficient $F(2)$ given by Eq. (2.86). The statistical tensors of rank two obtained for the ρ^0 meson in the transversity frame are given in Tables 6.4 and 6.5. Analogically Tables 6.6 and 6.7 list the statistical tensors of rank two measured for the ϕ meson in the transversity frame.

As mentioned above, it is expected that for parity conserving decays those statistical tensors with $M = 1$ in the transversity frame should be equal zero and they are. The only exception is the slight deviation from zero of $\mathrm{Im}T^2_1$ in the fourth $-t$ bin for ρ^0meson. On the contrary the tensors of even rank are significantly different from zero, for bothρ^0 and ϕ mesons, in case M is also even. This again is in agreement with the expectations for parity conserving decays.

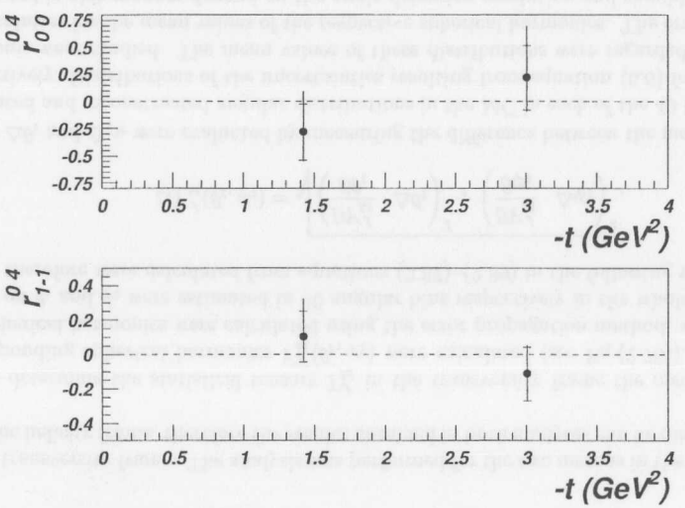

Figure 6.14: The fitted values of the spin density matrix elements for the proton-dissociative J/ψ photoproduction as a function of $-t$. The inner error bars correspond to the statistical uncertainty, while the outer ones represent the statistical and systematical uncertainties added in quadrature.

$-t$ range (GeV^2)	$\langle -t \rangle$ (GeV^2)	ReT_1^2	ImT_1^2
1.1-1.7	1.34	-0.010 ± 0.010	0.003 ± 0.014
1.7-2.9	2.14	-0.005 ± 0.009	0.008 ± 0.014
2.9-4.0	3.35	0.006 ± 0.009	0.012 ± 0.014
4.0-12	5.67	0.005 ± 0.009	-0.035 ± 0.013
2.9-12	4.38	0.005 ± 0.009	-0.004 ± 0.013

Table 6.4: The values of statistical tensors ReT_1^2 and ImT_1^2 in the transversity frame measured for the ρ^0 meson in different $-t$ bins. The uncertainties are estimated based on the error propagation method.

Having the statistical tensors of rank two measured in the transversity frame the statistical tensors of the same rank in the helicity frame can be calculated according to relations (2.90), (2.91) and (2.92). Table 6.8 and 6.9 contain the statistical tensors of rank two in the helicity frame obtained in this way for the ρ^0 and ϕ mesons, respectively.

The statistical tensors in any frame are related to the meson spin density matrix elements in that frame according to Eq. (2.59). Therefore having calculated the statistical tensors of rank two in the helicity frame only one more step in the analysis allows to obtain the sought

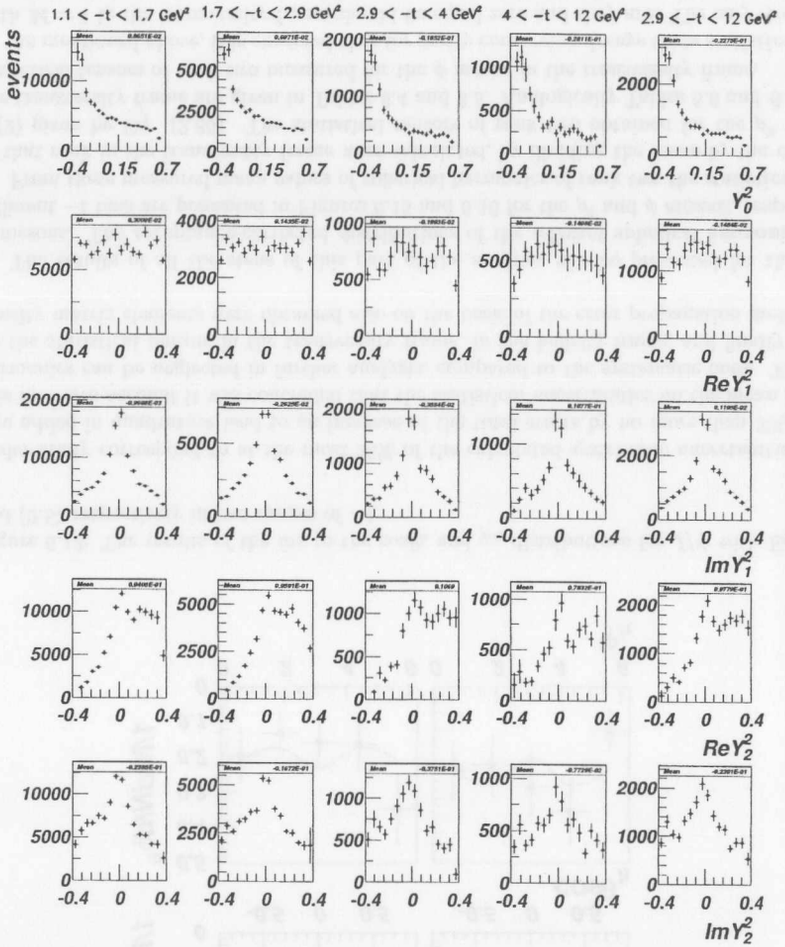

Figure 6.15: The acceptance-corrected distributions of the spherical harmonics of rank two for the ρ^0 meson in different $-t$ bins in the transversity frame. The mean values are given in each plot.

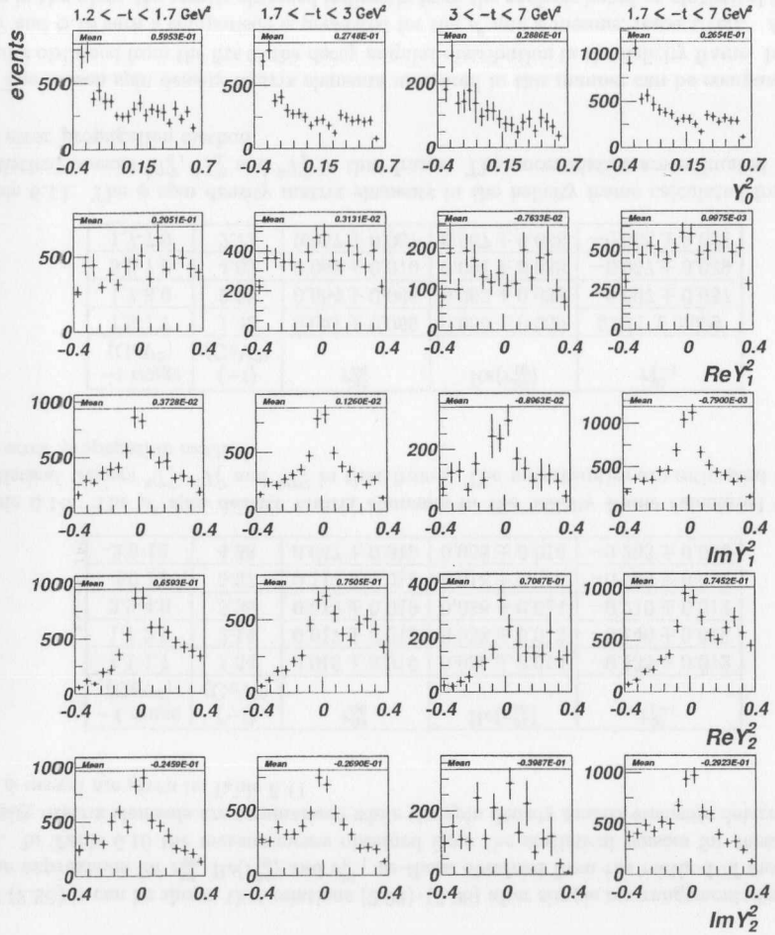

Figure 6.16: The acceptance-corrected distributions of the spherical harmonics of rank two for the ϕ meson in different $-t$ bins in the transversity frame. The mean values are given in each plot.

$-t$ range (GeV^2)	$\langle -t \rangle$ (GeV^2)	T_0^2	ReT_2^2	ImT_2^2
1.1-1.7	1.34	-0.028 ± 0.013	-0.304 ± 0.018	0.077 ± 0.019
1.7-2.9	2.14	-0.023 ± 0.013	-0.307 ± 0.018	0.054 ± 0.019
2.9-4.0	3.35	0.060 ± 0.012	-0.346 ± 0.019	0.121 ± 0.020
4.0-12	5.67	0.091 ± 0.012	-0.253 ± 0.018	0.025 ± 0.020
2.9-12	4.38	0.074 ± 0.012	-0.316 ± 0.018	0.074 ± 0.020

Table 6.5: The values of statistical tensors T_0^2, ReT_2^2 and ImT_2^2 in the transversity frame measured for the ρ^0 meson in different $-t$ bins.The uncertainties are estimated based on the error propagation method.

$-t$ (GeV^2)	$\langle t \rangle$ (GeV^2)	ReT_1^2	ImT_1^2
1.2-1.7	1.42	-0.066 ± 0.053	-0.012 ± 0.045
1.7-3.0	2.20	-0.010 ± 0.049	-0.004 ± 0.041
3.0-7.0	4.03	0.026 ± 0.051	0.029 ± 0.045
1.7-7.0	2.72	-0.003 ± 0.050	0.003 ± 0.042

Table 6.6: The values of statistical tensors ReT_1^2 and ImT_1^2 in the transversity frame measured for the ϕ meson in different $-t$ bins. The uncertainties are estimated based on the error propagation method.

$-t$ (GeV^2)	$\langle t \rangle$ (GeV^2)	T_0^2	ReT_2^2	ImT_2^2
1.2-1.7	1.42	-0.193 ± 0.033	-0.213 ± 0.067	0.080 ± 0.055
1.7-3.0	2.20	-0.089 ± 0.030	-0.243 ± 0.065	0.087 ± 0.054
3.0-7.0	4.03	-0.093 ± 0.030	-0.229 ± 0.070	0.129 ± 0.054
1.7-7.0	2.72	-0.086 ± 0.030	-0.241 ± 0.066	0.095 ± 0.054

Table 6.7: The values of statistical tensors T_0^2, ReT_2^2 and ImT_2^2 in the transversity frame measured for the ϕ meson in different $-t$ bins. The uncertainties are estimated based on the error propagation method.

$-t$ range (GeV^2)	$\langle -t \rangle$ (GeV^2)	${}^hT_0^2$	${}^hT_1^2$	${}^hT_2^2$
1.1-1.7	1.34	0.387 ± 0.023	-0.077 ± 0.019	-0.135 ± 0.012
1.7-2.9	2.14	0.388 ± 0.023	-0.054 ± 0.019	-0.140 ± 0.012
2.9-4.0	3.35	0.394 ± 0.023	-0.121 ± 0.020	-0.210 ± 0.012
4.0-12	5.67	0.265 ± 0.022	-0.025 ± 0.020	-0.182 ± 0.012
2.9-12	4.38	0.351 ± 0.023	-0.074 ± 0.020	-0.203 ± 0.012

Table 6.8: The values of the ρ^0 statistical tensors ${}^hT_0^2$, ${}^hT_1^2$ and ${}^hT_2^2$ in the helicity frame calculated from the measured statistical tensors of rank two in the transversity frame in different $-t$ bins. The uncertainties are estimated based on the error propagation method.

spin density matrix elements. By introducing the calculated statistical tensors of rank two in the helicity frame into equations (2.96), (2.97) and (2.98) we obtain r_{00}^{04}, Re(r_{10}^{04}) and r_{1-1}^{04} respectively. It should be mentioned here that these elements are the same as the spin density matrix elements denoted by $\rho_{mm'}$ in equations (2.96)-(2.98). Starting from equations (2.76)

$-t$ (GeV^2)	$\langle t \rangle$ (GeV^2)	${}^hT_0^2$	${}^hT_1^2$	${}^hT_1^2$
1.2-1.7	1.42	0.358 ± 0.084	-0.080 ± 0.055	0.011 ± 0.039
1.7-3.0	2.20	0.342 ± 0.081	-0.087 ± 0.054	-0.067 ± 0.037
3.0-7.0	4.03	0.328 ± 0.086	-0.129 ± 0.054	-0.057 ± 0.039
1.7-7.0	2.72	0.338 ± 0.082	-0.095 ± 0.054	-0.068 ± 0.038

Table 6.9: The values of the ϕ statistical tensors ${}^hT_0^2$, ${}^hT_1^2$ and ${}^hT_2^2$ in the helicity frame calculated from the measured statistical tensors of rank two in the transversity frame in different $-t$ bins. The uncertainties are estimated based on the error propagation method.

and (2.86) it can be shown that relations (2.96)–(2.98) after simple rearrangements lead to the same expressions for r_{00}^{04}, $\mathrm{Re}(r_{10}^{04})$ and r_{1-1}^{04} as those obtained from the method of moments in [28]. In Table 6.10 the measurements obtained from the statistical tensors for these ρ^0 spin density matrix elements are summarized while the spin density matrix elements determined for the ϕ meson are given in Table 6.11.

$-t$ range (GeV^2)	$\langle -t \rangle$ (GeV^2)	r_{00}^{04}	$\mathrm{Re}(r_{10}^{04})$	r_{1-1}^{04}
1.1-1.7	1.34	0.018 ± 0.019	0.055 ± 0.014	-0.135 ± 0.012
1.7-2.9	2.14	0.017 ± 0.019	0.038 ± 0.013	-0.140 ± 0.012
2.9-4.0	3.35	0.012 ± 0.019	0.086 ± 0.014	-0.210 ± 0.012
4.0-12	5.67	0.117 ± 0.018	0.018 ± 0.014	-0.182 ± 0.012
2.9-12	4.38	0.047 ± 0.019	0.053 ± 0.014	-0.203 ± 0.012

Table 6.10: The ρ^0 spin density matrix elements in the helicity frame calculated from the statistical tensors ${}^hT_0^2$, ${}^hT_1^2$ and ${}^hT_2^2$ in that frame. The uncertainties are estimated based on the error propagation method.

$-t$ range (GeV^2)	$\langle -t \rangle$ (GeV^2)	r_{00}^{04}	$\mathrm{Re}(r_{10}^{04})$	r_{1-1}^{04}
1.2-1.7	1.42	0.041 ± 0.069	0.056 ± 0.039	0.011 ± 0.039
1.7-3.0	2.20	0.054 ± 0.066	0.062 ± 0.038	-0.067 ± 0.037
3.0-7.0	4.03	0.066 ± 0.070	0.091 ± 0.038	-0.057 ± 0.039
1.7-7.0	2.72	0.057 ± 0.067	0.067 ± 0.038	-0.068 ± 0.038

Table 6.11: The ϕ spin density matrix elements in the helicity frame calculated from the ϕ statistical tensors ${}^hT_0^2$, ${}^hT_1^2$ and ${}^hT_2^2$ in that frame. The uncertainties are estimated based on the error propagation method.

The meson spin density matrix elements measured in this manner can be compared to the results obtained from the fits to the decay angular distribution in the helicity frame. In Figures 6.17 and 6.18 such a comparison is presented for the ρ^0 and ϕ mesons, respectively. As can be seen in the plots, the results obtained indirectly from the analysis based on statistical tensors in the transversity frame give good agreement with the measurements of the spin density matrix elements resulting from the fits to the decay angular distribution in the helicity frame. The violation of the SCHC hypothesis in the case of light mesons is clearly confirmed by the results obtained from the statistical tensors method.

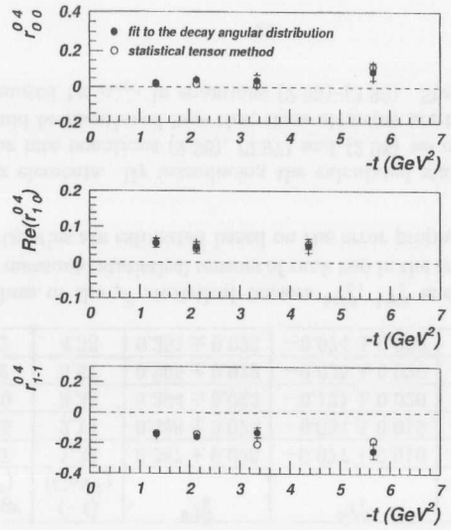

Figure 6.17: The comparison of the ρ^0 spin density matrix elements obtained from fits to the decay angular distribution in the helicity frame (full circles) and indirectly by the determination of the statistical tensors in the transversity frame (open circles).

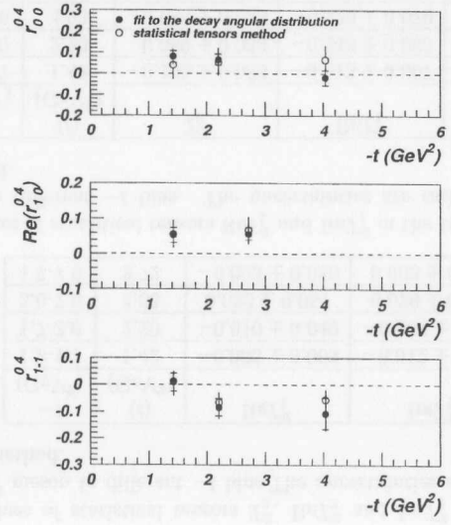

Figure 6.18: The comparison of the ϕ spin density matrix elements obtained from fits to the decay angular distribution in the helicity frame (full circles) and indirectly by the determination of the statistical tensors in the transversity frame (open circles).

Chapter 7

Discussion

7.1 Comparison of the three measurement methods

In this thesis the spin density matrix elements r^{04}_{00}, $\mathrm{Re}(r^{04}_{10})$ and r^{04}_{1-1} for the ρ^0 and ϕ mesons have been measured as a function of $-t$ with the use of three of the available methods. Among these methods are the fits to the one dimensional angular distributions $W(\cos\theta_h)$ and $W(\varphi_h)$ in the helicity frame, fits to the two dimensional angular distribution $W(\cos\theta_h, \varphi_h)$ in the helicity frame, and the statistical tensors method. The measurements within each method were performed in corresponding ranges in $-t$ so that the obtained results for the spin density matrix elements could be directly compared. In Tables 7.1 and 7.3 the measurements resulting for ρ^0 from the three methods are summarized for the r^{04}_{00} and r^{04}_{1-1} elements respectively. Since the element $\mathrm{Re}(r^{04}_{10})$ cannot be determined from any of the one dimensional fits, Table 7.2 contains the comparison of the results from a two dimensional fit and the statistical tensors method. Analogical information on the spin density matrix elements measured for the ϕ meson is summarized in Tables 7.4 to 7.6.

r^{04}_{00} measurements for ρ^0				
$-t$ range (GeV^2)	$\langle -t \rangle$ (GeV^2)	1-dim $W(\cos\theta_h)$ fit	2-dim $W(\cos\theta_h, \varphi_h)$ fit	statistical tensors method
1.1-1.7	1.34	$0.022\pm0.015^{+0.016}_{-0.018}$	$0.018\pm0.021^{+0.013}_{-0.016}$	0.016±0.018
1.7-2.9	2.14	$0.042\pm0.017^{+0.018}_{-0.021}$	$0.044\pm0.026^{+0.021}_{-0.024}$	0.017±0.019
2.9-4.0	3.35	$0.037\pm0.034^{+0.032}_{-0.036}$		0.012±0.019
4.0-12	5.67	$0.090\pm0.049^{+0.035}_{-0.040}$		0.117±0.018
2.9-12	4.38		$0.049\pm0.039^{+0.026}_{-0.024}$	0.047±0.019

Table 7.1: The results obtained for the r^{04}_{00} element of the ρ^0 spin density matrix by fitting one and two dimensional decay angular distributions in the helicity frame and a comparison to the results obtained from statistical tensors in the transversity frame. The first uncertainties are statistical and the second the systematic.

The results for the ρ^0 spin density matrix elements obtained with the use of the three methods are all in satisfactory agreement. As can be seen in Table 7.1, the measurements obtained from the one and two dimensional fits for r^{04}_{00} in the first two $-t$ ranges are in excellent agreement. Within the errors also the values measured with the statistical tensors method agree with the fit results in all the $-t$ ranges considered. As for the $\mathrm{Re}(r^{04}_{10})$ element the results of the two dimensional fits to the angular distribution in the helicity frame are in perfect agreement with the corresponding measurements obtained with the statistical tensors method (see Table

$\mathrm{Re}(r^{04}_{10})$ measurements for ρ^0			
$-t$ range (GeV^2)	$\langle -t \rangle$ (GeV^2)	2-dim $W(\cos\theta_h, \varphi_h)$ fit	statistical tensors method
1.1-1.7	1.34	$0.054\pm0.012^{+0.017}_{-0.010}$	0.055±0.014
1.7-2.9	2.14	$0.045\pm0.013^{+0.016}_{-0.010}$	0.038±0.013
2.9-12	4.38	$0.047\pm0.020^{+0.009}_{-0.017}$	0.053±0.014

Table 7.2: The results obtained for the $\mathrm{Re}(r^{04}_{10})$ element of the ρ^0 spin density matrix by fitting one and two dimensional decay angular distributions in the helicity frame and a comparison to the results obtained from statistical tensors in the transversity frame.The first uncertainties are statistical and the second the systematic.

r^{04}_{1-1} measurements for ρ^0				
$-t$ range (GeV^2)	$\langle -t \rangle$ (GeV^2)	1-dim $W(\varphi_h)$ fit	2-dim $W(\cos\theta_h, \varphi_h)$ fit	statistical tensors method
1.1-1.7	1.34	$-0.143\pm0.014^{+0.023}_{-0.031}$	$-0.145\pm0.017^{+0.031}_{-0.025}$	-0.135±0.012
1.7-2.9	2.14	$-0.158\pm0.017^{+0.020}_{-0.022}$	$-0.138\pm0.021^{+0.013}_{-0.019}$	-0.140±0.012
2.9-4.0	3.35	$-0.129\pm0.032^{+0.023}_{-0.050}$		-0.210±0.012
4.0-12	5.67	$-0.252\pm0.047^{+0.044}_{-0.023}$		-0.182±0.012
2.9-12	4.38		$-0.194\pm0.032^{+0.024}_{-0.042}$	-0.203±0.012

Table 7.3: The results obtained for the r^{04}_{1-1} element of the ρ^0 spin density matrix by fitting one- and two-dimensional decay angular distributions in the helicity frame and a comparison to the results obtained from statistical tensors in the transversity frame. The first uncertainties are statistical and the second the systematic.

7.2). The r^{04}_{1-1} measurements for ρ^0 show a slight discrepancy between the one dimensional fit results and the statistical tensors method in the 3rd and 4th $-t$ bins, but otherwise all three methods are in good agreement, as shown in Table 7.3.

r^{04}_{00} measurements for ϕ				
$-t$ range (GeV^2)	$\langle -t \rangle$ (GeV^2)	1-dim $W(\cos\theta_h)$ fit	2-dim $W(\cos\theta_h, \varphi_h)$ fit	statistical tensors method
1.2-1.7	1.42	$0.080\pm0.028^{+0.020}_{-0.026}$	$0.070\pm0.047^{+0.040}_{-0.017}$	0.041±0.069
1.7-3.0	2.20	$0.066\pm0.025^{+0.034}_{-0.021}$		0.054±0.066
3.0-7.0	4.03	$-0.020\pm0.035^{+0.034}_{-0.018}$		0.066±0.070
1.7-7.0	2.72		$0.083\pm0.041^{+0.022}_{-0.044}$	0.057±0.067

Table 7.4: The results obtained for the r^{04}_{00} element of the ϕ spin density matrix by fitting one- and two-dimensional decay angular distributions in the helicity frame and a comparison to the results obtained from statistical tensors in the transversity frame.The first uncertainties are statistical and the second the systematic.

Also the measurements conducted with the three different methods for the ϕ spin density matrix elements show satisfactory agreement. In Table 7.4 The measurements of the r^{04}_{00} element are summarized. The results obtained with the three different methods in the corresponding $-t$ ranges are equal within errors. Only in the 3rd $-t$ bin a slight discrepancy between the results from the one dimensional fit and the statistical tensors method is observed, but nevertheless both measurements are equal zero within the errors. The $\mathrm{Re}(r^{04}_{10})$ measurements obtained from the two dimensional decay angular fit and the statistical tensors method are in excellent

$\mathrm{Re}(r^{04}_{10})$ measurements for ϕ			
$-t$ range (GeV^2)	$\langle -t \rangle$ (GeV^2)	2-dim $W(\cos\theta_h, \varphi_h)$ fit	statistical tensors method
1.2-1.7	1.42	$0.053 \pm 0.021^{+0.019}_{-0.024}$	0.056 ± 0.039
1.7-7.0	2.72	$0.057 \pm 0.018^{+0.013}_{-0.007}$	0.067 ± 0.038

Table 7.5: The results obtained for the $\mathrm{Re}(r^{04}_{10})$ element of the ϕ spin density matrix by fitting one- and two-dimensional decay angular distributions in the helicity frame and a comparison to the results obtained from statistical tensors in the transversity frame.The first uncertainties are statistical and the second the systematic.

r^{04}_{1-1} measurements for ϕ				
$-t$ range (GeV^2)	$\langle -t \rangle$ (GeV^2)	1-dim $W(\varphi_h)$ fit	2-dim $W(\cos\theta_h, \varphi_h)$ fit	statistical tensors method
1.2-1.7	1.42	$0.008 \pm 0.033^{+0.011}_{-0.039}$	$-0.078 \pm 0.041^{+0.037}_{-0.027}$	0.011 ± 0.039
1.7-3.0	2.20	$-0.085 \pm 0.032^{+0.023}_{-0.028}$		-0.067 ± 0.037
3.0-7.0	4.03	$-0.108 \pm 0.058^{+0.053}_{-0.030}$		-0.057 ± 0.039
1.7-7.0	2.72		$-0.079 \pm 0.035^{+0.008}_{-0.017}$	-0.068 ± 0.038

Table 7.6: The results obtained for the r^{04}_{1-1} element of the ϕ spin density matrix by fitting one- and two-dimensional decay angular distributions in the helicity frame and a comparison to the results obtained from statistical tensors in the transversity frame.The first uncertainties are statistical and the second the systematic.

agreement for the ϕ in both $-t$ ranges considered. This is summarized in Table 7.5. The comparison of the results obtained for the r^{04}_{1-1} element with the three methods is presented in Table 7.6. The results of the three methods are in good agreement in all the $-t$ bins, except for the first one, where the result of the two dimensional fit is clearly below those obtained from the one dimensional fit and the statistical tensors method. This may be due to the statistical fluctuations in the two dimensional decay angular distribution, where the same sample of events was distributed between twice as many bins as in the one dimensional angular distributions. Although on first sight this measurement seems to show big disagreement between the results of the one and two dimensional fits, the total errors on these measurements overlap.

7.2 Summary of the results

The ρ^0, ϕ and J/ψ spin density matrix elements r^{04}_{00} and r^{04}_{1-1} were obtained by fitting the background-subtracted and acceptance-corrected decay angular distributions in several $-t$ ranges. For the ρ^0 and ϕ mesons the $\mathrm{Re}(r^{04}_{10})$ element was determined from a two dimensional fit to the decay angular distribution in three and two $-t$ intervals, respectively. Unfortunately, due to the limited statistics of the sample, a two dimensional fit could not be performed for the J/ψ meson. Additionally as a cross check to these results an analysis in the transversity frame, based on the statistical tensors method, was performed.

The small values obtained for the r^{04}_{00} measured for the ρ^0 meson indicate that the probability to produce ρ^0 mesons in the helicity 0 state from a photon of helicity ± 1 is small over the entire $-t$ range. This probability from the performed measurements is $4 \pm 5\%$ at $-t = 3.35$ GeV^2 and $9 \pm 6\%$ at $-t = 5.57$ GeV^2. The non-zero values of $\mathrm{Re}(r^{04}_{10})$ and r^{04}_{1-1} reflect the contributions from the helicity single-flip and double-flip amplitudes, respectively. The non-zero

and significantly negative results obtained for r^{04}_{1-1} stand in clear disagreement with the SCHC expectations. The clearly non-zero values of $\mathrm{Re}(r^{04}_{10})$ show, that there is a fraction of events in which longitudinally polarized ρ^0 mesons are produced from transverse photons. Therefore, although the helicity non-flip amplitude dominates in these measurements, the observation of SCHC violation is a fact for the ρ^0 meson.

The measurements of the ϕ spin density matrix elements are similar to those obtained for the ρ^0, although have smaller statistical significance. Nevertheless, the results obtained for the $\mathrm{Re}(r^{04}_{10})$ and r^{04}_{1-1} elements, show that the single and double helicity-flip contributions cannot be overlooked also in the case of the ϕ meson.

Figure 7.1 shows the spin density matrix elements measured in this analysis for the ρ^0 and ϕ mesons in comparison with previous results [7] obtained for ρ^0 in the lower $-t$ region. For

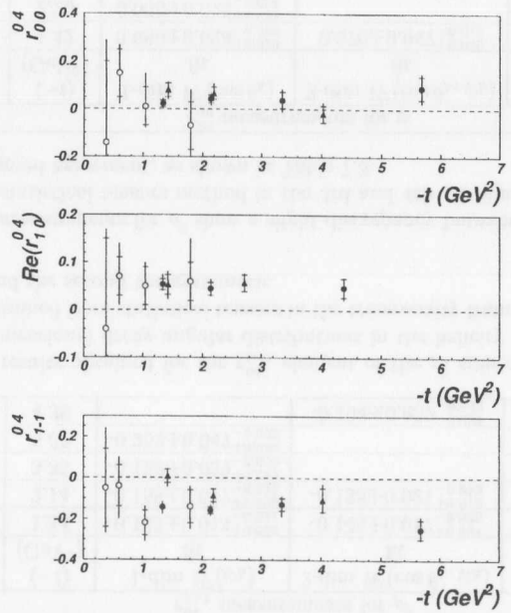

Figure 7.1: The spin density matrix elements as a function of $-t$ measured in this analysis compared to previous results at lower $-t$. The full symbols correspond to the measurements for proton-dissociative ρ^0 (circles) and ϕ (triangles) photoproduction. The open circles are the published ZEUS ρ^0 results. [7]

both these vector mesons the obtained results show a clear deviation from SCHC expectations. Both the helicity single-flip and the helicity double-flip contributions are observed for the two light vector mesons studied in this analysis. From the comparison presented in Figure 7.1 it

seems that the spin density matrix elements of both ρ^0 and ϕ are the same and independent of the meson mass. The results obtained in this analysis for ρ^0 are in agreement in the region of overlap with the earlier ZEUS measurements [7] at lower $-t$.

The spin density matrix elements measured for J/ψ on the other hand show no deviation from SCHC for large $-t$, as within the large errors the obtained values are compatible with zero. For J/ψ these measurements of the spin density matrix elements are the first at such high values of $-t$.

In Figure 7.2 the $\cos\theta_h$ and φ_h distributions with the results of the fits in the highest $-t$ range for each vector meson are presented. Overlayed on these distributions with a dashed line are the expectations of the SCHC hypothesis. It is clear that the flat φ_h distribution, predicted

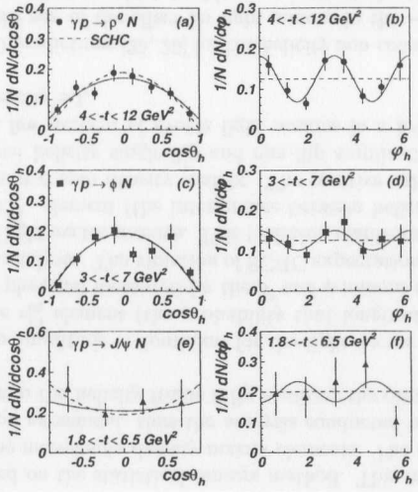

Figure 7.2: The normalized background-subtracted and acceptance-corrected $\cos\theta_h$ and φ_h distributions for proton-dissociative ρ^0(a,b), ϕ(c,d) and J/ψ(e,f) photoproduction. The symbols are the data, the solid curves are the results of the one dimensional fits and the dashed curves represent the SCHC expectations

by SCHC and represented by the dashed line, disagrees with the ρ^0 data, indicating a violation of the SCHC.

The analysis conducted in the transversity frame, based on the statistical tensors method, enabled an indirect determination of the same spin density matrix elements as in the helicity frame. These results proved to be in good agreement with the measurements obtained from the fits to the angular distributions of ρ^0 and ϕ decay products in the helicity frame.

7.3 Comparison with pQCD predictions

The pQCD predictions of [25, 26] presented in Sec. 2.3.3 are here confronted with the results of the conducted analysis.

The results obtained for the J/ψ are consistent with the SCHC expectations as predicted by the pQCD calculations conducted in [25]. However, the model for the light vector meson production proposed in [25] is not applicable to the measurements obtained in this thesis. No bounds at $-t \approx 1$ GeV^2 and $-t \approx 5$ GeV^2 for the ϕ and rho^0 mesons respectively, at which the production of mesons in helicity 0 states should exceed the production of those with helicity ± 1, have been observed. The probability to produce a light vector meson in a helicity 0 state grows slowly with $-t$, but even at the high end of the range under study does not exceed 15% for the ρ^0 meson.

In the case of light vector meson production the non-flip helicity amplitude dominates in the $-t$ region under study as predicted in [26]. However, the ratios of the helicity amplitudes T_{01}/T_{11} and T_{-11}/T_{11} obtained from the measured values of the r^{04}_{00}, Re(r^{04}_{10}) and r^{04}_{1-1} elements for the ρ^0 meson (see Eq. (2.54)) are different than those predicted by this model. From the measured ρ^0 spin density matrix elements, the following values of the ratios of the helicity amplitudes are obtained: $T_{01}/T_{11} = 0.09 \pm 0.05$ over the entire $1.1 < -t < 12$ GeV^2 range and $T_{-11}/T_{11} = -0.16 \pm 0.03$ at $-t = 2.14$ GeV^2 while at $-t = 5.67$ GeV^2 the ratio $T_{-11}/T_{11} = -0.25 \pm 0.06$. All this compared to the model predicted ratios $0.25 < T_{01}/T_{11} < 0.35$ and $-0.02 < T_{-11}/T_{11} < 0.04$, shows that the observed contribution from longitudinally polarized light vector mesons is therefore smaller than that predicted by pQCD calculations, even at the highest values of $-t$ reached in the analysis. The measured contribution from the double-flip helicity amplitude is on the other hand bigger than expected. Therefore this recent Ivanov et al. [26] model is not able to quantitatively describe the present data.

Chapter 8

Conclusions

The spin density matrix elements r^{04}_{00}, $\mathrm{Re}(r^{04}_{10})$ and r^{04}_{1-1} have been measured for the diffractive photoproduction of ρ^0, ϕ, and J/ψ mesons with proton dissociation at $W \approx 100$ GeV and $-t$ values up to 12 GeV^2. The main methods of measurement include the one and two dimensional fits to the decay angular distributions in the helicity frame and an independent analysis in the transversity frame, based on the statistical tensors method. This method allowed for an indirect determination of the meson spin density matrix elements. The results obtained with these methods were all in good agreement, thus the analysis conducted in the transversity frame as a cross-check to the one in the helicity frame fully confirms the obtained results.

The helicity non-flip amplitude is dominant for the light vector meson production at large $-t$, as the values of the r^{04}_{00} element (the probability that longitudinal vector mesons will be produced by transverse photons) measured for the ρ^0 and ϕ mesons are small over the entire $-t$ range considered in the analysis. The violation of SCHC expectations was however observed for the photoproduction of light vector mesons. This violation manifests itself mainly in the clearly negative values of the r^{04}_{1-1} element (the interference between helicity double-flip and non-flip amplitudes) of the ρ^0 and ϕ spin density matrix. The positive values of the $\mathrm{Re}(r^{04}_{10})$ element (the interference between helicity single-flip and non-flip amplitudes) measured for ρ^0 and ϕ mesons show that in a few percent of events light mesons in a helicity 0 state are produced from real photons of helicity ± 1.

The available pQCD predictions [25, 26] for the helicity non-conservation at high $-t$ seem to strongly overestimate the size of the effect for light mesons in the $-t$ range under study. Until now there is no pQCD prediction, which is able to quantitatively describe the results obtained for the ρ^0 and ϕ mesons in this thesis. The pQCD predictions for the helicity conservation in the photoproduction of heavy mesons [25] is confirmed by the results obtained in this thesis for the J/ψ meson. Both measured J/ψ spin density matrix elements r^{04}_{00} and r^{04}_{1-1} within large errors are consistent with zero and thus with SCHC expectations. Due to the inconsistency of the presented measurements with the available pQCD predictions for the light mesons, no final conclusion about whether large values of $-t$ can serve as a hard scale for pQCD calculations can be made.

Acknowledgements

I am most grateful to my supervisor, Prof. Danuta Kisielewska, for her continuous scientific advice and guidance, great attention devoted to my work and patient, friendly encouragement. I appreciate very much the tremendous effort she invested in helping me consolidate my thesis into a reasonable shape.

The study presented here has been realized within the framework of the ZEUS Collaboration. I would like to thank all its members for the pleasure I had in working with them and for the help I have so many times received. I am especially indebted to Leszek Adamczyk, from whom I gained valuable knowledge through many inspiring discussions. His experienced advice and constructive criticism of my work were very helpful in the realization of this thesis. With Kasia Klimek I often shared my ups and downs during these long months of completion of this study. She best understands the difficulties of this analysis and the joy of overcoming them. I am grateful to her for her inestimable support and good humor.

I would like to thank my parents for their understanding and patient encouragement and most of all my husband Marek for his love and heroic support in this difficult period of simultaneous realisation of two doctoral theses - his and mine.

I could not forget to thank my friends for their friendly company and lasting encouragement. I would like to thank Agnieszka Oblakowska–Mucha and Mariusz Przybycień for their deep interest in my work and so many inspiring questions. I am grateful to Janusz Szuba and Andrzej Rybicki for answering the innumerable questions I've been asking during the last year and for countless suggestions, which made my work easier. Last, but not least, I would like to thank Dorota Szuba, for being an excellent companion and for her incredible sense of humor.

Appendix A

r_{00}^{04} 1-dim fit systematic error analysis for ρ^0				
Check	$-t$ range (GeV^2)			
	1.1-1.7	1.7-2.9	2.9-4.0	4.0-12
$\|\eta\| < 2.0$	0.028	0.041	0.038	0.089
$\|\eta\| < 2.2$	0.023	0.042	0.036	0.088
$p_T > 0.1$ GeV	0.016	0.031	0.035	0.075
$p_T > 0.2$ GeV	0.032	0.041	0.043	0.077
$\|V_Z\| < 35$ cm	0.021	0.042	0.031	0.079
$\|V_Z\| < 45$ cm	0.023	0.042	0.041	0.083
$V_r < 0.5$ cm	0.028	0.055	0.030	0.090
$V_r < 1.0$ cm	0.024	0.043	0.040	0.090
$E_{max}(0.2rad) < 0.2$ GeV	0.016	0.044	0.038	0.076
$E_{max}(0.2rad) < 0.3$ GeV	0.022	0.043	0.035	0.103
$E_{max}(0.15rad) < 0.25$ GeV	0.008	0.053	0.024	0.113
$E_{max}(0.25rad) < 0.25$ GeV	0.024	0.043	0.040	0.100
$0.45 < M_{\pi\pi} < 1.0$ GeV	0.028	0.046	0.009	0.098
$0.65 < M_{\pi\pi} < 1.2$ GeV	0.031	0.036	0.066	0.084
$M_{\pi\pi}$ fit with bkg=const	0.024	0.043	0.038	0.095
PRT-tag	0.020	0.048	0.049	0.107
Low-lumi	0.033	0.039	0.088	0.125
High-lumi	0.003	0.034	0.122	0.084
SCHC assumed	0.024	0.026	0.024	0.060
$\mathrm{ACC}_{PT}(W_{\gamma p} - 3$ GeV)	0.021	0.039	0.037	0.086
$\mathrm{ACC}_{PT}(W_{\gamma p} + 3$ GeV)	0.022	0.044	0.037	0.093
t slope varied by $+0.04$ GeV^2	0.023	0.043	0.038	0.090
t slope varied by -0.04 GeV^2	0.021	0.042	0.037	0.089
$\mathrm{REMC}_{eff}+6\%$	0.021	0.042	0.037	0.089
$\mathrm{REMC}_{eff}-6\%$	0.023	0.025	0.038	0.090
$\beta(t) = exp(0.226 - 0.297 \cdot t)$	0.023	0.042	0.038	0.090
$\beta(t) = exp(0.146 - 0.297 \cdot t)$	0.021	0.043	0.037	0.090
$\beta(t) = exp(0.186 - 0.320 \cdot t)$	0.021	0.042	0.037	0.090
$\beta(t) = exp(0.186 - 0.274 \cdot t)$	0.023	0.042	0.037	0.089

Table A.1: Values obtained for the r_{00}^{04} element of the ρ^0 spin density matrix, from one dimensional fits to the $\cos\theta_h$ distribution, for each of the listed systematic checks (see Section 6.1).

r_{1-1}^{04} 1-dim fit systematic uncertainty for ρ^0				
Check	$-t$ range (GeV^2)			
	1.1-1.7	1.7-2.9	2.9-4.0	4.0-12
$\|\eta\| < 2.0$	-0.151	-0.157	-0.131	-0.252
$\|\eta\| < 2.2$	-0.141	-0.160	-0.131	-0.251
$p_T > 0.1$ GeV	-0.136	-0.158	-0.131	-0.245
$p_T > 0.2$ GeV	-0.140	-0.159	-0.124	-0.240
$\|V_Z\| < 35$ cm	-0.140	-0.160	-0.128	-0.239
$\|V_Z\| < 45$ cm	-0.140	-0.157	-0.130	-0.246
$V_r < 0.5$ cm	-0.143	-0.164	-0.139	-0.269
$V_r < 1.0$ cm	-0.142	-0.153	-0.123	-0.249
$E_{max}(0.2rad) < 0.2$ GeV	-0.141	-0.159	-0.126	-0.250
$E_{max}(0.2rad) < 0.3$ GeV	-0.145	-0.154	-0.136	-0.244
$E_{max}(0.15rad) < 0.25$ GeV	-0.144	-0.159	-0.111	-0.237
$E_{max}(0.25rad) < 0.25$ GeV	-0.141	-0.153	-0.137	-0.242
$0.45 < M_{\pi\pi} < 1.0$ GeV	-0.155	-0.147	-0.166	-0.219
$0.65 < M_{\pi\pi} < 1.2$ GeV	-0.159	-0.171	-0.161	-0.266
$M_{\pi\pi}$ fit with bkg=const	-0.145	-0.157	-0.131	-0.250
PRT-tag	-0.150	-0.170	-0.120	-0.247
Low-lumi	-0.137	-0.159	-0.143	-0.304
High-lumi	-0.163	-0.163	-0.155	-0.174
SCHC assumed	-0.130	-0.145	-0.133	-0.242
$\mathrm{ACC}_{PT}(W_{\gamma p} - 3$ GeV)	-0.165	-0.166	-0.133	-0.256
$\mathrm{ACC}_{PT}(W_{\gamma p} + 3$ GeV)	-0.128	-0.1501	-0.127	-0.249
t slope varied by $+0.04$ GeV^2	-0.142	-0.157	-0.129	-0.252
t slope varied by -0.04 GeV^2	-0.144	-0.159	-0.130	-0.252
$\mathrm{REMC}_{eff}+6\%$	-0.142	-0.158	-0.129	-0.251
$\mathrm{REMC}_{eff}-6\%$	-0.144	-0.158	-0.130	-0.252
$\beta(t) = exp(0.226 - 0.297 \cdot t)$	-0.143	-0.158	-0.130	-0.252
$\beta(t) = exp(0.146 - 0.297 \cdot t)$	-0.143	-0.158	-0.130	-0.251
$\beta(t) = exp(0.186 - 0.320 \cdot t)$	-0.143	-0.158	-0.130	-0.251
$\beta(t) = exp(0.186 - 0.274 \cdot t)$	-0.143	-0.159	-0.130	-0.252

Table A.2: Values obtained for the r_{1-1}^{04} element of the ρ^0 spin density matrix, from one dimensional fits to the φ_h distribution, for each of the listed systematic checks (see Section 6.1).

r_{00}^{04} 2-dim fit systematic error analysis for ρ^0			
Check	$-t$ range (GeV^2)		
	1.1-1.7	1.7-2.9	2.9-12
$\|\eta\| < 2.0$	0.021	0.034	0.047
$\|\eta\| < 2.2$	0.024	0.038	0.051
$p_T > 0.1$ GeV	0.018	0.040	0.057
$p_T > 0.2$ GeV	0.017	0.043	0.051
$\|V_Z\| < 35$ cm	0.020	0.039	0.053
$\|V_Z\| < 45$ cm	0.018	0.044	0.048
$V_r < 0.5$ cm	0.023	0.040	0.031
$V_r < 1.0$ cm	0.019	0.044	0.046
$E_{max}(0.2rad) < 0.2$ GeV	0.020	0.055	0.047
$E_{max}(0.2rad) < 0.3$ GeV	0.015	0.053	0.069
$E_{max}(0.15rad) < 0.25$ GeV	0.008	0.059	0.037
$E_{max}(0.25rad) < 0.25$ GeV	0.016	0.047	0.050
$0.45 < M_{\pi\pi} < 1.0$ GeV	0.010	0.043	0.052
$0.65 < M_{\pi\pi} < 1.2$ GeV	0.009	0.026	0.063
$M_{\pi\pi}$ fit with bkg=const	0.019	0.042	0.049
PRT-tag	0.025	0.046	0.045
Low-lumi	0.021	0.079	-0.005
High-lumi	0.007	0.010	0.062
SCHC assumed	0.020	0.047	0.053
$\text{ACC}_{PT}(W_{\gamma p} - 3$ GeV)	0.019	0.040	0.050
$\text{ACC}_{PT}(W_{\gamma p} + 3$ GeV)	0.017	0.046	0.048
t slope varied by +0.04 GeV^2	0.019	0.044	0.049
t slope varied by -0.04 GeV^2	0.017	0.042	0.049
REMC_{eff}+6%	0.017	0.043	0.049
REMC_{eff}−6%	0.019	0.044	0.049
$\beta(t) = exp(0.226 - 0.297 \cdot t)$	0.018	0.043	0.049
$\beta(t) = exp(0.146 - 0.297 \cdot t)$	0.018	0.044	0.050
$\beta(t) = exp(0.186 - 0.320 \cdot t)$	0.018	0.044	0.050
$\beta(t) = exp(0.186 - 0.274 \cdot t)$	0.018	0.043	0.049

Table A.3: Values obtained for the r_{00}^{04} element of the ρ^0 spin density matrix, from two dimensional fits to the decay angular distribution in the helicity frame, for each of the listed systematic checks (see Section 6.1).

Re(r_{10}^{04}) 2-dim fit systematic error analysis for ρ^0			
Check	$-t$ range (GeV^2)		
	1.1-1.7	1.7-2.9	2.9-12
$\|\eta\| < 2.0$	0.058	0.041	0.046
$\|\eta\| < 2.2$	0.054	0.045	0.047
$p_T > 0.1$ GeV	0.055	0.046	0.038
$p_T > 0.2$ GeV	0.058	0.045	0.045
$\|V_Z\| < 35$ cm	0.053	0.044	0.044
$\|V_Z\| < 45$ cm	0.054	0.045	0.042
$V_r < 0.5$ cm	0.056	0.052	0.046
$V_r < 1.0$ cm	0.054	0.041	0.047
$E_{max}(0.2rad) < 0.2$ GeV	0.053	0.047	0.054
$E_{max}(0.2rad) < 0.3$ GeV	0.054	0.043	0.051
$E_{max}(0.15rad) < 0.25$ GeV	0.061	0.047	0.043
$E_{max}(0.25rad) < 0.25$ GeV	0.053	0.044	0.040
$0.45 < M_{\pi\pi} < 1.0$ GeV	0.046	0.049	0.043
$0.65 < M_{\pi\pi} < 1.2$ GeV	0.051	0.038	0.045
$M_{\pi\pi}$ fit with bkg=const	0.053	0.046	0.047
PRT-tag	0.064	0.056	0.053
Low-lumi	0.043	0.059	0.049
High-lumi	0.058	0.030	0.040
SCHC assumed	0.048	0.038	0.042
$\text{ACC}_{PT}(W_{\gamma p} - 3$ GeV)	0.059	0.041	0.048
$\text{ACC}_{PT}(W_{\gamma p} + 3$ GeV)	0.050	0.047	0.047
t slope varied by +0.04 GeV^2	0.054	0.045	0.047
t slope varied by -0.04 GeV^2	0.054	0.044	0.047
REMC_{eff}+6%	0.054	0.044	0.046
REMC_{eff}−6%	0.054	0.045	0.048
$\beta(t) = exp(0.226 - 0.297 \cdot t)$	0.054	0.045	0.047
$\beta(t) = exp(0.146 - 0.297 \cdot t)$	0.054	0.044	0.047
$\beta(t) = exp(0.186 - 0.320 \cdot t)$	0.054	0.044	0.047
$\beta(t) = exp(0.186 - 0.274 \cdot t)$	0.054	0.045	0.047

Table A.4: Values obtained for the Re(r_{10}^{04}) element of the ρ^0 spin density matrix, from two dimensional fits to the decay angular distribution in the helicity frame, for each of the listed systematic checks (see Section 6.1).

r^{04}_{1-1} 2-dim fit systematic error analysis for ρ^0			
Check	$-t$ range (GeV^2)		
	1.1-1.7	1.7-2.9	2.9-12
$\|\eta\| < 2.0$	-0.152	-0.139	-0.196
$\|\eta\| < 2.2$	-0.145	-0.138	-0.194
$p_T > 0.1$ GeV	-0.146	-0.140	-0.203
$p_T > 0.2$ GeV	-0.128	-0.137	-0.191
$\|V_Z\| < 35$ cm	-0.145	-0.140	-0.192
$\|V_Z\| < 45$ cm	-0.141	-0.137	-0.188
$V_r < 0.5$ cm	-0.142	-0.139	-0.213
$V_r < 1.0$ cm	-0.142	-0.135	-0.191
$E_{max}(0.2rad) < 0.2$ GeV	-0.145	-0.137	-0.174
$E_{max}(0.2rad) < 0.3$ GeV	-0.139	-0.140	-0.202
$E_{max}(0.15rad) < 0.25$ GeV	-0.148	-0.137	-0.188
$E_{max}(0.25rad) < 0.25$ GeV	-0.147	-0.141	-0.190
$0.45 < M_{\pi\pi} < 1.0$ GeV	-0.157	-0.137	-0.225
$0.65 < M_{\pi\pi} < 1.2$ GeV	-0.155	-0.150	-0.195
$M_{\pi\pi}$ fit with bkg=const	-0.149	-0.138	-0.195
PRT-tag	-0.143	-0.150	-0.209
Low-lumi	-0.109	-0.085	-0.170
High-lumi	-0.159	-0.176	-0.196
SCHC assumed	-0.150	-0.143	-0.197
ACC$_{PT}(W_{\gamma p} - 3$ GeV)	-0.161	-0.147	-0.196
ACC$_{PT}(W_{\gamma p} + 3$ GeV)	-0.132	-0.131	-0.192
t slope varied by $+0.04$ GeV^2	-0.144	-0.138	-0.193
t slope varied by -0.04 GeV^2	-0.145	-0.139	-0.195
REMC$_{eff}$+6%	-0.144	-0.138	-0.194
REMC$_{eff}$−6%	-0.145	-0.139	-0.194
$\beta(t) = exp(0.226 - 0.297 \cdot t)$	-0.145	-0.138	-0.194
$\beta(t) = exp(0.146 - 0.297 \cdot t)$	-0.144	-0.138	-0.194
$\beta(t) = exp(0.186 - 0.320 \cdot t)$	-0.144	-0.138	-0.194
$\beta(t) = exp(0.186 - 0.274 \cdot t)$	-0.145	-0.138	-0.194

Table A.5: Values obtained for the r^{04}_{1-1} element of the ρ^0 spin density matrix, from two dimensional fits to the decay angular distribution in the helicity frame, for each of the listed systematic checks (see Section 6.1).

r^{04}_{00} 1-dim fit systematic error analysis for ϕ			
Check	$-t$ range (GeV^2)		
	1.1-1.7	1.7-3.0	3.0-7.0
$\|\eta\| < 2.0$	0.082	0.0612	-0.020
$\|\eta\| < 2.2$	0.080	0.067	-0.020
$p_T > 0.3$ GeV	0.072	0.052	-0.020
$p_T > 0.5$ GeV	0.097	0.092	-0.016
$\|V_Z\| < 35$ cm	0.077	0.069	-0.018
$\|V_Z\| < 45$ cm	0.083	0.064	-0.021
$V_r < 0.5$ cm	0.064	0.067	-0.0373
$V_r < 1.0$ cm	0.085	0.069	-0.004
$E_{max}(0.2rad) < 0.2$ GeV	0.084	0.086	0.003
$E_{max}(0.2rad) < 0.3$ GeV	0.087	0.072	-0.013
$E_{max}(0.15rad) < 0.25$ GeV	0.072	0.074	-0.017
$E_{max}(0.25rad) < 0.25$ GeV	0.084	0.071	-0.005
PRT-tag	0.080	0.056	-0.010
Low-lumi	0.023	0.024	0.015
High-lumi	0.120	0.055	-0.102
SCHC assumed	0.065	0.057	-0.015
ACC$_{PT}(W_{\gamma p} - 3$ GeV)	0.074	0.066	-0.019
ACC$_{PT}(W_{\gamma p} + 3$ GeV)	0.078	0.062	-0.025
t slope varied by $+0.14$ GeV^2	0.081	0.067	-0.020
t slope varied by -0.14 GeV^2	0.079	0.066	-0.020
REMC$_{eff}$+6%	0.080	0.067	-0.020
REMC$_{eff}$−6%	0.080	0.066	-0.020
$\beta(t) = exp(0.561 - 0.505 \cdot t)$	0.081	0.067	-0.019
$\beta(t) = exp(0.361 - 0.505 \cdot t)$	0.080	0.066	-0.020
$\beta(t) = exp(0.461 - 0.562 \cdot t)$	0.079	0.066	-0.020
$\beta(t) = exp(0.461 - 0.448 \cdot t)$	0.081	0.067	-0.019

Table A.6: Values obtained for the r^{04}_{00} element of the ϕ spin density matrix, from one dimensional fits to the $\cos\theta_h$ distribution, for each of the listed systematic checks (see Section 6.1).

r^{04}_{1-1} 1-dim fit systematic error analysis for ϕ			
Check	$-t$ range (GeV^2)		
	1.1-1.7	1.7-3.0	3.0-7.0
$\|\eta\| < 2.0$	0.006	-0.085	-0.107
$\|\eta\| < 2.2$	0.004	-0.085	-0.108
$p_T > 0.3$ GeV	-0.003	-0.082	-0.108
$p_T > 0.5$ GeV	-0.015	-0.095	-0.112
$\|V_Z\| < 35$ cm	0.010	-0.082	-0.103
$\|V_Z\| < 45$ cm	0.007	-0.087	-0.106
$V_r < 0.5$ cm	0.015	-0.093	-0.136
$V_r < 1.0$ cm	0.009	-0.084	-0.087
$E_{max}(0.2rad) < 0.2$ GeV	0.014	-0.080	-0.092
$E_{max}(0.2rad) < 0.3$ GeV	0.013	-0.075	-0.117
$E_{max}(0.15rad) < 0.25$ GeV	0.005	-0.085	-0.081
$E_{max}(0.25rad) < 0.25$ GeV	-0.002	-0.083	-0.091
PRT-tag	-0.017	-0.110	-0.076
Low-lumi	-0.047	-0.063	-0.072
High-lumi	0.012	-0.125	-0.170
SCHC assumed	0.006	-0.089	-0.096
$\mathrm{ACC}_{PT}(W_{\gamma p} - 3$ GeV)	0.000	-0.088	-0.104
$\mathrm{ACC}_{PT}(W_{\gamma p} + 3$ GeV)	0.004	-0.086	-0.107
t slope varied by $+0.14$ GeV^2	0.010	-0.085	-0.108
t slope varied by -0.14 GeV^2	0.007	-0.086	-0.107
REMC_{eff}+6%	0.009	-0.085	-0.107
REMC_{eff}−6%	0.008	-0.086	-0.107
$\beta(t) = exp(0.561 - 0.505 \cdot t)$	0.005	-0.088	-0.108
$\beta(t) = exp(0.361 - 0.505 \cdot t)$	0.012	-0.083	-0.107
$\beta(t) = exp(0.461 - 0.562 \cdot t)$	0.011	-0.083	-0.107
$\beta(t) = exp(0.461 - 0.448 \cdot t)$	0.005	-0.088	-0.108

Table A.7: Values obtained for the r^{04}_{1-1} element of the ϕ spin density matrix, from one dimensional fits to the φ_h distribution, for each of the listed systematic checks (see Section 6.1).

r^{04}_{00} 2-dim fit systematic error analysis for ϕ		
Check	$-t$ range (GeV^2)	
	1.1-1.7	1.7-7.0
$\|\eta\| < 2.0$	0,082	0,084
$\|\eta\| < 2.2$	0,073	0,083
$p_T > 0.3$ GeV	0,081	0,067
$\|V_Z\| < 35$ cm	0,063	0,087
$\|V_Z\| < 45$ cm	0,071	0,079
$V_r < 0.5$ cm	0,066	0,069
$V_r < 1.0$ cm	0,077	0,073
$E_{max}(0.2rad) < 0.2$ GeV	0,064	0,104
$E_{max}(0.2rad) < 0.3$ GeV	0,080	0,060
$E_{max}(0.15rad) < 0.25$ GeV	0,062	0,059
$E_{max}(0.25rad) < 0.25$ GeV	0,072	0,071
PRT-tag	0,103	0,079
Low-lumi	0,044	0,051
High-lumi	0,059	0,090
SCHC assumed	0,069	0,078
$\mathrm{ACC}_{PT}(W_{\gamma p} - 3$ GeV)	0,065	0,082
$\mathrm{ACC}_{PT}(W_{\gamma p} + 3$ GeV)	0,071	0,084
t slope varied by $+0.14$ GeV^2	0,070	0,083
t slope varied by -0.14 GeV^2	0,069	0,083
REMC_{eff}+6%	0,069	0,082
REMC_{eff}−6%	0,070	0,083
$\beta(t) = exp(0.561 - 0.505 \cdot t)$	0,071	0,084
$\beta(t) = exp(0.361 - 0.505 \cdot t)$	0,068	0,082
$\beta(t) = exp(0.461 - 0.562 \cdot t)$	0,069	0,082
$\beta(t) = exp(0.461 - 0.448 \cdot t)$	0,071	0,084

Table A.8: Values obtained for the r^{04}_{00} element of the ϕ spin density matrix, from two dimensional fits to the decay angular distribution in the helicity frame, for each of the listed systematic checks (see Section 6.1).

$\mathrm{Re}(r^{04}_{10})$ 2-dim fit systematic error analysis for ϕ		
Check	$-t$ range (GeV^2)	
	1.1-1.7	1.7-7.0
$\|\eta\| < 2.0$	0,057	0,056
$\|\eta\| < 2.2$	0,047	0,056
$p_T > 0.3$ GeV	0,048	0,065
$\|V_Z\| < 35$ cm	0,052	0,058
$\|V_Z\| < 45$ cm	0,050	0,056
$V_r < 0.5$ cm	0,056	0,056
$V_r < 1.0$ cm	0,050	0,052
$E_{max}(0.2rad) < 0.2$ GeV	0,047	0,062
$E_{max}(0.2rad) < 0.3$ GeV	0,037	0,062
$E_{max}(0.15rad) < 0.25$ GeV	0,041	0,056
$E_{max}(0.25rad) < 0.25$ GeV	0,058	0,057
PRT-tag	0,070	0,063
Low-lumi	0,022	0,040
High-lumi	0,034	0,058
SCHC assumed	0,043	0,053
$\mathrm{ACC}_{PT}(W_{\gamma p} - 3$ GeV)	0,055	0,058
$\mathrm{ACC}_{PT}(W_{\gamma p} + 3$ GeV)	0,052	0,056
t slope varied by $+0.14$ GeV^2	0,054	0,057
t slope varied by -0.14 GeV^2	0,052	0,057
REMC_{eff}+6%	0,053	0,057
REMC_{eff}−6%	0,053	0,057
$\beta(t) = exp(0.561 - 0.505 \cdot t)$	0,051	0,057
$\beta(t) = exp(0.361 - 0.505 \cdot t)$	0,054	0,057
$\beta(t) = exp(0.461 - 0.562 \cdot t)$	0,054	0,057
$\beta(t) = exp(0.461 - 0.448 \cdot t)$	0,052	0,057

Table A.9: Values obtained for the $\mathrm{Re}(r^{04}_{00})$ element of the ϕ spin density matrix, from two dimensional fits to the decay angular distribution in the helicity frame, for each of the listed systematic checks (see Section 6.1).

r^{04}_{1-1} 2-dim fit systematic error analysis for ϕ		
Check	$-t$ range (GeV^2)	
	1.1-1.7	1.7-7.0
$\|\eta\| < 2.0$	-0,081	-0,080
$\|\eta\| < 2.2$	-0,101	-0,080
$p_T > 0.3$ GeV	-0,077	-0,082
$\|V_Z\| < 35$ cm	-0,078	-0,080
$\|V_Z\| < 45$ cm	-0,083	-0,079
$V_r < 0.5$ cm	-0,082	-0,087
$V_r < 1.0$ cm	-0,084	-0,072
$E_{max}(0.2rad) < 0.2$ GeV	-0,082	-0,077
$E_{max}(0.2rad) < 0.3$ GeV	-0,083	-0,088
$E_{max}(0.15rad) < 0.25$ GeV	-0,062	-0,077
$E_{max}(0.25rad) < 0.25$ GeV	-0,087	-0,083
PRT-tag	-0,046	-0,089
Low-lumi	-0,052	-0,058
High-lumi	-0,016	-0,100
SCHC assumed	-0,080	-0,081
$\mathrm{ACC}_{PT}(W_{\gamma p} - 3$ GeV)	-0,083	-0,079
$\mathrm{ACC}_{PT}(W_{\gamma p} + 3$ GeV)	-0,073	-0,079
t slope varied by $+0.14$ GeV^2	-0,077	-0,079
t slope varied by -0.14 GeV^2	-0,079	-0,079
REMC_{eff}+6%	-0,079	-0,078
REMC_{eff}−6%	-0,078	-0,079
$\beta(t) = exp(0.561 - 0.505 \cdot t)$	-0,083	-0,080
$\beta(t) = exp(0.361 - 0.505 \cdot t)$	-0,073	-0,078
$\beta(t) = exp(0.461 - 0.562 \cdot t)$	-0,074	-0,078
$\beta(t) = exp(0.461 - 0.448 \cdot t)$	-0,082	-0,080

Table A.10: Values obtained for the r^{04}_{1-1} element of the ϕ spin density matrix, from two dimensional fits to the decay angular distribution in the helicity frame, for each of the listed systematic checks (see Section 6.1).

r_{00}^{04} 1-dim fit systematic error analysis for J/ψ		
Check	$-t$ range (GeV^2)	
	1.1-1.8	1.8-6.5
$\|\eta\| < 2.0$	-0.292	0.221
$\|\eta\| < 2.2$	-0.276	0.221
$p_T > 0.4$ GeV	-0.258	0.248
$p_T > 0.6$ GeV	-0.263	0.157
$\|V_Z\| < 35$ cm	-0.225	0.232
$\|V_Z\| < 45$ cm	-0.235	0.224
$V_r < 0.5$ cm	-0.312	0.210
$V_r < 1.0$ cm	-0.285	0.207
$E_{max}(0.2rad) < 0.2$ GeV	-0.172	0.302
$E_{max}(0.2rad) < 0.3$ GeV	-0.350	0.147
$E_{max}(0.15rad) < 0.25$ GeV	-0.286	0.189
$E_{max}(0.25rad) < 0.25$ GeV	-0.291	0.233
PRT-tag	-0.312	0.473
ACC$_{PT}(W_{\gamma p} - 3$ GeV)	-0.265	0.237
ACC$_{PT}(W_{\gamma p} + 3$ GeV)	-0.301	0.204
t slope varied by $+0.18$ GeV^2	-0.283	0.220
t slope varied by -0.18 GeV^2	-0.285	0.214
$r_{00}^{04} = 0.15$ and $r_{1-1}^{04} = 0$	-0.156	0.370
$r_{00}^{04} = 0$ and $r_{1-1}^{04} = 0.11$	-0.078	0.432
$r_{00}^{04} = 0$ and $r_{1-1}^{04} = -0.11$	-0.085	0.477
$\beta(t) = 0.90$	-0.296	0.258
$\beta(t) = 0.36$	-0.264	0.185

Table A.11: Values obtained for the r_{00}^{04} element of the J/ψ spin density matrix, from one dimensional fits to $\cos\theta_h$ distribution, for each of the listed systematic checks (see Section 6.1).

r_{1-1}^{04} 1-dim fit systematic error analysis for J/ψ		
Check	$-t$ range (GeV^2)	
	1.1-1.8	1.8-6.5
$\|\eta\| < 2.0$	0.100	-0.110
$\|\eta\| < 2.2$	0.096	-0.112
$p_T > 0.4$ GeV	0.100	-0.100
$p_T > 0.6$ GeV	0.133	-0.139
$\|V_Z\| < 35$ cm	0.102	-0.108
$\|V_Z\| < 45$ cm	0.119	-0.111
$V_r < 0.5$ cm	0.110	-0.115
$V_r < 1.0$ cm	0.104	-0.120
$E_{max}(0.2rad) < 0.2$ GeV	0.159	-0.130
$E_{max}(0.2rad) < 0.3$ GeV	0.101	-0.062
$E_{max}(0.15rad) < 0.25$ GeV	0.109	-0.094
$E_{max}(0.25rad) < 0.25$ GeV	0.096	-0.125
PRT-tag	0.253	-0.130
ACC$_{PT}(W_{\gamma p} - 3$ GeV)	0.105	-0.104
ACC$_{PT}(W_{\gamma p} + 3$ GeV)	0.104	-0.121
t slope varied by $+0.18$ GeV^2	0.104	-0.112
t slope varied by -0.18 GeV^2	0.106	-0.113
$r_{00}^{04} = 0.15$ and $r_{1-1}^{04} = 0$	0.098	-0.102
$r_{00}^{04} = 0$ and $r_{1-1}^{04} = 0.11$	0.091	-0.112
$r_{00}^{04} = 0$ and $r_{1-1}^{04} = -0.11$	0.097	-0.094
$\beta(t) = 0.90$	0.122	-0.103
$\beta(t) = 0.36$	0.081	-0.120

Table A.12: Values obtained for the r_{1-1}^{04} element of the J/ψ spin density matrix, from one dimensional fits to the φ_h distribution, for each of the listed systematic checks (see Section 6.1).

Bibliography

[1] H. Abramowicz, A. Caldwell, "Hera Collider Physics", DESY 98-192 (1998), and references therein

[2] J.A. Crittenden, "Exclusive Production of Neutral Vector Mesons at the Electron-Proton Collider HERA", Springer Tracts in Modern Physics, Volume 140 (Springer, Berlin Heidelberg, 1997)

[3] L. Frankfurt, M. Strikmann, Phys. Rev. Lett. 63 (1989) 1914.

[4] A.H. Mueller, W-K. Tang, Phys. Lett. B284 (1992) 123.

[5] ZEUS Collaboration, J. Breitweg et al., Eur. Phys. J. C2 (1998), 247.

[6] ZEUS Collaboration, J. Breitweg et al., Paper Contributed to the International Conference on High Energy Physics, Osaka 2000 (Abstract 884)

[7] ZEUS Collaboration, J. Breitweg et al., Eur. Phys. J. C14 (2000) 213.

[8] K. Klimek, PhD Thesis, DESY-THESIS-2001-053

[9] ZEUS Collaboration, J. Breitweg et al., Eur. Phys. J. C12 (2000) 393.

[10] H1 Collaboration, C. Adloff et al., Eur. Phys. J. C13 (2000) 371.

[11] C. Collard, H1 Collaboration, Proc. of the DIS2001 workshop, Bologna, Italy, 2001

[12] H1 Collaboration, C. Adloff et al., Phys. Lett. B483 (2000) 360.

[13] G. Levman, ZEUS Note 95-088

[14] J.J. Sakurai, Phys. Rev. Lett. 22 (1969) 981.

[15] T.H. Bauer et al., Rev. Mod. Phys. 50 (1978) 261.

[16] J.J. Sakurai, D. Schildknecht, Phys. Lett. B40 (1972) 121.

[17] P.D.B. Collins, "An Introduction to Regge Theory and High Energy Physics", Cambridge University Press, 1997

[18] A. Donnachie, P.V. Landshoff, Phys. Lett. B296 (1992) 227.

[19] S.J. Brodsky et al., Phys. Rev. D50 (1994) 3134.

[20] M.G. Ryskin, Zeit. Phys. C57 (1993) 89.
M.G. Ryskin et al., Zeit. Phys. C76 (1997) 231.

[21] J. Bartels et al., Phys. Lett B375 (1996) 301.

[22] F.J. Gilman et al., Phys. Lett.B31 (1910) 387.

[23] D.Yu. Ivanov, Phys. Rev. D53 (1996) 3564.

[24] V.L. Chernyak and A.R. Zhitnitsky, Phys. Rep. 112 (1984) 173.

[25] I. Ginzburg and D.Yu. Ivanov, Phys. Rev. D54 (1996) 5523.

[26] D.Yu. Ivanov et al., Phys. Lett. B478 (2000) 101.

[27] H. Abramowicz, L. Frankfurt and M. Strikmann, Surveys in High Energy Physics 11 (1999) 51.

[28] K. Schilling, G.Wolf, Nucl. Phys. B61 (1973) 381.

[29] A.A. Sokolov and I.M. Ternov, Sov. Phys. Dokl. 8 (1964) 1203.

[30] M. Jacob, G.C. Wick, Ann of Phys. 7 (1959) 404.

[31] K. Schilling, R. Seyboth, G.Wolf, Nucl. Phys. B15 (1970) 397.

[32] A. Kotański, "Resonance Decay distributions and Transversity Amplitudes", Ecole Internationale de la Physique des Particules Elementaires, Herceg-Novi,Strasbourg-Belgrade, 1970

[33] A. Kotański, K. Zalewski, Nucl. Phys. B4 (1968) 559.

[34] G. Wolf, "HERA: physics, machine and experiments", Lectures given at *Inst. of Techniques and Concepts of High Energy Physics*, St. Croix, Virgin Islands, June 19-30, 1986, DESY 86-089 (1986)

[35] HERA, "A Proposal for a Large Electron-Proton Colliding Beam Facility at DESY", DESY HERA 81-10 (1981)

[36] ZEUS collaboration, M. Derrick et al., The ZEUS Detector Status Report 1993, DESY (1993)

[37] N. Harnew et al., Nucl. Instr. and Meth. A 279 (1989) 290.
B. Foster et al., Nucl. Phys. B 32 (Proc. Suppl.) (1993) 181.
B. Foster et al., Nucl. Instr. and Meth. A 338 (1994) 254.

[38] D. Bailey et al., "The Design and Performance of the ZEUS Central Tracking Detector z-by-Timing System", ZEUS Note 97-055 (1997)

[39] M. Derrick et al., Nucl Instr. and Meth. A309 (1991) 77.
A. Andersen et al., Nucl Instr. and Meth. A309 (1991) 101.
A. Bernstein et al., Nucl Instr. and Meth. A336 (1993) 23.
A Caldwell et al., Nucl Instr. and Meth. A321 (1992) 356.

[40] K. Dessler, ZEUS Note 95-061

[41] H. Bethe, W. Heitler, Proc. Roy. Soc. A146 (1934) 83.
H.A. Bethe, Phys. Rev. 89 (1953) 1256.

[42] J. Andruszków et al., "Luminosity Measurement in the ZEUS Experiment", Acta Phys. Polon. B, 32 (2001) 2025.

[43] G.F. Hartner et al., "VCTRAK (3.07/04): Off-line Output Information", ZEUS Note 97-064

[44] TRKCLU1, ZEUS user library

[45] M. Kasprzak, ZEUS Note 95-069 (1995)

[46] M. Kasprzak, PhD Thesis, Warsaw University, DESY Internal Report: DESY F35D-96-16, November 1996

[47] B.R. Webber, Ann. Rev. Nucl. Part. Sci. 36 (1986) 253.
G. Marchesini et al., Comput. Phys. Comm. 67 (1992) 465.

[48] R. Brun et al., "GEANT3", CERN DD/EE/11-1 (1989).

[49] MOZART, ZEUS internal package.

[50] Els de Wolf (editor) et al., "ZGANA, ZEUS trigger simulation library".

[51] Albrow et al., Nucl. Phys. B108 (1975) 1.

[52] UA8 Collaboration, A. Brandt et al., Nucl. Phys. B514 (1998) 3.

[53] L. Adamczyk, PhD Thesis, DESY-THESIS-1999-045, December 1999

[54] G. Zech, DESY 95-113, June 1995.

[55] F. James, M. Roos, MINUIT Function Minimization, CERN-Note D506, Nucl. Instr. and Meth. A340 (1994) 396.

[56] P. Söding, Phys. Lett. 19 (1966) 702.

[57] D. Westphal, PhD Thesis, DESY Internal Report: F35D-97-11, November 1997